UNIMORE
UNIVERSITÀ DEGLI STUDI DI
MODENA E REGGIO EMILIA

DEPARTMENT OF
SCIENCES AND METHOD FOR ENGINEERING

DOCTORATE SCHOOL
INDUSTRIAL INNOVATION ENGINEERING
XXXVIII CYCLE

WEAKLY TURBULENT CONVECTION REGIMES OF HEAVY LIQUID METALS IN ROD BUNDLES

Scientific Tutor:
Prof. Ing. Diego Angeli

Candidate:
Danila Trane

School Dean:
Prof. Ing. Franco Zambonelli

UNIVERSITY OF MODENA AND REGGIO EMILIA
ACADEMIC YEAR 2024/2025

Abstract

Abstract - English version

The study of thermal hydraulics in rod bundles is of great importance to tackle the new challenges presented by the design of IV generation nuclear reactors, in particular those using liquid metals as coolant, aimed at increasing their safety and improving the efficient use of resources.

The state-of-the-art reveals certain limitations concerning the implementation of the most commonly used turbulence models, as well as the presence of inaccuracies in the correlations employed for the prediction of friction factors or Nusselt numbers. This outcome is attributable to models founded on the well-known Reynolds analogy, whose validity extends to fluids characterised by a Prandtl number (Pr) of approximately 1, a value far from that of liquid metals (Pr«1). Furthermore, widely employed correlations are typically valid within restricted ranges spectrum of free governing parameters and are derived from very early experiments. The development and validation of new advanced models can be achieved through the use of high-fidelity data from experimental programmes or computational investigations. The present study will focus on the latter.

The first aim of this work is to investigate the effects of buoyancy on flow around rod bundles, a subject that has received limited attention in the existing literature.

Direct Numerical Simulation (DNS) is adopted to analyse the flow dynamics and thermal characteristics of liquid metals around four vertical cylindrical rods arranged in a square lattice, for both forced and mixed convection conditions. First order statistics are provided, in addition to the detailed budgets of turbulent kinetic energy and turbulent heat fluxes, whose contributions are relevant for the calibration of new turbulence models.

In the second part of this work, the focus will be directed towards the results obtained in the context of a benchmark exercise proposed by the EGTHM (Expert Group on Reactor Core Thermal-Hydraulics and Mechanics), group belonging to NEA (Nuclear Energy Agency). The computational data concerning a fully developed flow around a triangular lattice of bare rod bundles are attained by means of DNS. The reference system for the thermo-hydraulic exercise is the Advanced LFR European Demonstrator, bundle geometry for which high-resolution Particle Image Velocimetry (PIV) data were produced by the Texas A&M University in collaboration with Westinghouse Electric Company. The analysis will not be confined to a comparison with experimental data; but it will rather constitute an integration to the experiment.

Another contribution that high-fidelity simulations can give to the aforementioned research field is in the development of machine learning models. In the final section of this study, carried out during my research stay at the *von Karman Institute for Fluid Dynamics* (Sint-Genesius-Rode, Belgium) as part of my period abroad, the data obtained from previous DNSs are pre-processed to obtain suitable parameters for an artificial neural network, which aim is to implement a correction to the subgrid-viscosity of frequently employed turbulence models.

In conclusion, the results offer an insight into the effects of buoyancy in liquid metal flows and supply high-fidelity data for the future development of more accurate turbulence models, enriching the connection between fundamental research and practical reactor design.

Abstract - Italian version

Lo studio della termo-idraulica dei fluidi attorno a fasci di barre è di grande importanza per affrontare le nuove sfide nella progettazione dei reattori nucleari di quarta generazione, in particolare quelli che utilizzano metalli liquidi come refrig-

erante, con l'obiettivo di aumentarne la sicurezza e migliorare l'uso efficiente delle risorse.

Lo stato dell'arte rivela alcune limitazioni relative all'implementazione dei modelli di turbolenza più comunemente utilizzati, nonché la presenza di imprecisioni nelle correlazioni impiegate per la previsione dei fattori di attrito o dei numeri di Nusselt. Questo risultato è attribuibile a modelli basati sulla ben nota analogia di Reynolds, la cui validità si estende ai fluidi caratterizzati da un numero di Prandtl (Pr) di circa 1, un valore lontano da quello dei metalli liquidi (Pr«1). Inoltre, le correlazioni ampiamente utilizzate sono tipicamente delineate all'interno di uno spettro ristretto di parametri e derivano da primissimi esperimenti condotti sulla trasmissione di calore attorno a barre cilindriche. Lo sviluppo e la validazione di nuovi modelli avanzati possono essere ottenuti attraverso l'uso di dati ad alta fedeltà provenienti da campagne sperimentali o indagini computazionali. Il presente studio si concentrerà su questi ultimi.

Il primo obiettivo di questo lavoro è quello di studiare gli effetti del galleggiamento sul flusso attorno a fasci di barre, un argomento che ha ricevuto scarsa attenzione nella letteratura esistente. La dinamica del flusso e le caratteristiche termiche dei metalli liquidi attorno a quattro barre cilindriche verticali disposte in un reticolo quadrato, sia in condizioni di convezione forzata che mista, sono stati analizzati utilizzando Direct Numerical Simulations (DNS). Si presentano le statistiche del primo ordine e i bilanci dettagliati dell'energia cinetica turbolenta e dei flussi di calore turbolenti, i cui contributi sono rilevanti per la calibrazione di nuovi modelli di turbolenza.

Nella seconda parte di questo lavoro, l'attenzione sarà rivolta ai risultati ottenuti nell'ambito di un esercizio di benchmark proposto dall'EGTHM (Expert Group on Reactor Core Thermal-Hydraulics and Mechanics), gruppo appartenente a NEA (Nuclear Energy Agency). I dati computazionali relativi ad un flusso completamente sviluppato attorno a un reticolo triangolare di fasci di barre sono ottenuti mediante DNS. Il sistema di riferimento per l'esercizio termoidraulico è l'Advanced LFR European Demonstrator, per il quale sono stati prodotti dati ad alta risoluzione di Particle Image Velocimetry (PIV) dalla Texas A&M University in collaboratione con Westinghouse Electric Company. L'analisi non si limiterà a un confronto con i dati sperimentali, ma costituirà un'integrazione laddove l'esperimento presenta dei lim-

iti.

Un altro contributo che le simulazioni ad alta fedeltà possono dare al suddetto campo di ricerca è lo sviluppo di modelli machine learning. Nella parte finale di questo studio, svolto durante il mio periodo di ricerca all'estero presso il *von Karman Institute for Fluid Dynamics* (Sint-Genesius-Rode, Belgium), i dati ottenuti da precedenti DNS vengono elaborati per ottenere parametri adeguati ad una rete neurale artificiale, il cui scopo è quello di implementare una correzione della viscosità subgrid dei modelli di turbolenza più frequentemente utilizzati.

In conclusione, i risultati offrono una visione approfondita degli effetti di galleggiamento nei flussi di metallo liquido e forniscono dati ad alta fedeltà per lo sviluppo futuro di modelli di turbolenza più accurati, rafforzando il legame tra attività di ricerca fondamentale e fase progettuale dei reattori.

Contents

CHAPTER 1

Introduction

The investigation of the turbulent flow and heat transfer around rod bundles is of huge interest to a wide range of engineering applications. The behaviour of the flow may be influenced by a multitude of specifications, including the arrangement of the bundle, the spacing between rods, the nature of the working fluid and the influence of gravity. The present study focuses on rod bundle configurations that imply the use of refrigerant fluids with low Prandtl number. This analysis is of particular interest in the multidisciplinary context of the design of new IV generation nuclear reactors. Gen-IV innovative nuclear reactors differ from previous generations for the adoption of novel fluids for the purposes of heat removal: among these fluids, liquid metals are distinguished by a Prandtl number that is much lower than unity. In fluids with a Prandtl number of approximately one, the statistical properties of the turbulent velocity and temperature fields are analogous, and the diffusive and conductive wall layers exhibit a comparable thickness (*Reynolds analogy*). As the Prandtl number decreases, the conductive heat flux becomes increasingly significant in the proximity of the walls, and there is no similarity between the time-averaged velocity and temperature profiles. This specific feature has implications for the turbulence and heat transfer models most commonly used in computational fluid dynamics, which show significant limitations.

Quite some effort has been put in the development of liquid metal cooled nuclear

reactors as the developments are mostly related to design work of reactors. The most noteworthy initiatives are outlined hereafter [1]:

- Advanced Sodium Technology Reactor for Industrial Demonstration (ASTRID): the goals will be to demonstrate the multirecycling and transmutation capabilities of the uranium-plutonium cycle on an industrial scale and to demonstrate the feasibility and operability of sodium-cooled fast reactors for commercial power production.
- Advanced Lead Fast Reactor European Demonstrator (ALFRED): prototypical design options are integrated to be used in the industrial-size plants, using proved and available technical solutions to the maximum extent possible, in order to ease qualification and licensing.
- Multipurpose hYbrid Research Reactor for High-tech Applications (MYRRHA): an innovative multipurpose fast-spectrum research reactor employing lead-bismuth eutectic as primary coolant. It is also able to operate in critical mode.
- Swedish Advanced Lead-cooled Reactor (SEALER): is designed to meet the demands for commercial power production in Arctic regions of Canada.

In the existing literature, there are numerous case studies that adopt more common models, such as $k-\varepsilon$ or $k-\omega$ SST, or even more innovative ones, as algebraic heat flux models, in an attempt to describe the behaviour of the fluid as accurately as possible without having to perform high-fidelity calculations. However, as demonstrated by various studies and briefly mentioned in the literature review in Chapter 2, there are certain scenarios where the models employed necessitate precise calibration: for example, in the presence of flows exhibiting anisotropic and non-equilibrium turbulence, the reliability of simple eddy diffusivity models is compromised [2].

The verification of the compatibility of the aforementioned models, as well as the development and validation of new ones, constitutes a central aspect within the thermal hydraulic research framework of Gen IV reactors. This implies not only a low-Prandtl number fluid, as well as the occurrence of exceptional operational

conditions, such as fluids at reduced velocity or instances of plant malfunction. These conditions may lead to the presence of transitional regimes and mixed or natural convection, areas which remain under-documented in the field. The present study aims to make a contribution to this relatively unexplored area of research.

1.1. Structure and organisation

A comprehensive overview of the current state of the art with respect to flows around rod bundles adopting frequently fluids is provided in Chapter 2. This is accompanied by a concise presentation of the most widely employed models and their respective limitations when adopted for specific geometries, including wire-wrapped rods or assemblies with spacer grids. The focus then shifts towards analysing fluids with low Prandtl numbers, with the aim of reporting their characteristics for both basic reaserch geometries and rod bundles.

Chapter 3 introduces the numerical methodology employed to perform Direct Numerical Simulations in this work. The proposed immersed boundary approach [3] preserves second-order accuracy throughout the computational domain while ensuring a good calculation performance.

In Chapter 4 the results of Direct Numerical Simulations of fully developed flow in a bundle of vertical heated rods in a square arrangement are presented. The fluid is assumed to be Liquid Lead-Bismuth Eutectic (LBE) by imposing a Prandtl number of 0.031. A total of four cases are examined, one characterised by forced convection ($Ra = 0$) and three by mixed convection ($Ra = 2.5\times10^3, 2.5\times10^4, 5.0\times10^4$). Statistics relating to velocity and temperature fields are presented to highlight the effects that buoyancy has on the flow. Furthermore, the contributions to turbulent budgets are shown, which are of considerable interest for the development and validation of new turbulence models.

Chapter 5 shows the results for the NEA Lead-Cooled Fast Reactor benchmark exercise proposed by EGTHM [4]. Based on the provided specifications, a DNS of fully developed flow in a bare rod bundle domain is performed to generate high-fidelity results. The benchmark aims to characterise the flow around rod bundles in the presence of grid spacers, reproducing as faithfully as possible through CFD models an experiment carried out at Texas A&M University in collaboration with Westinghouse Electric Company [5]. The dataset presented then acts as an excellent tool for the

understanding of the actual effects that the grid spacers have on the flow.
In Chapter 6 preliminary results of an attempt to develop an hybrid turbulence model are presented. The work was conducted during a research stay at *von Karman Institute for Fluid Dynamics* (Sint-Genesius-Rode, Belgium) under the supervision of Dr. L. Koloszar and Dr. M. Fiore. This study offers a valuable practical example of how high-fidelity datasets can be employed to validate new turbulence models, thereby contributing meaningfully to areas that remain relatively unexplored in the literature.

CHAPTER 2

Literature review

2.1. Liquid metal cooled IV generation nuclear reactors

This chapter will provide a general overview of the field of research in which flow around rod bundles is of greatest interest, i.e. the design of new liquid metal cooled IV generation reactors. The aim is to explore the most commonly used approaches, whether experiments or computational simulations, and their possible limitations.

2.1.1. Benefits and drawbacks of liquid metals as coolants

Nuclear reactors in general use uranium as natural resource to produce energy. The identified resources and additional exploitable resources of uranium are sufficient to support continued use and significant growth of nuclear energy production for well over 300 years. However, the use of uranium in the widely spread water-cooled nuclear reactors can be significantly improved: in these thermal reactors, only a very small amount of the uranium is actually split into fission products and producing energy. By switching to fast reactors, uranium can be used much more efficiently. As fast reactors operate with fast neutrons inducing fission reactions, they cannot be cooled by water that would slow down (or moderate) the neutrons. Alternatively, another coolant has to be used. Mostly, liquid sodium has been applied, for its great

heat transport and neutronic characteristics. However, sodium also has its drawbacks, especially stemming from its chemical reactivity with air and water. Other liquid metals, such as lead or lead-bismuth eutectic, do not react equally violently with air and water and are also considered for that reason. For a comprehensive overview on the liquid-metal fast reactor designs constructed and operated all over the world, reference may be made to textbooks such as: IAEA [6,7] or Pioro *et al.* [8].

From a thermal hydraulic perspective, the use of liquid metals as coolants poses new challenges and necessitates of advanced tools in comparison to the employment of water and gas.
The thermo-hydraulic benefits and drawbacks of using liquid metals are hereafter listed and shortly described. As for the advantages:

- The metals remain liquid at the operating temperatures of the nuclear reactor, with a sufficient margin below their boiling point. As a result, the reactor can be operated without pressurization and at low pressure, in contrast to water-cooled reactors.
- Liquid metals typically possess good heat transport characteristics and high heat capacity, allowing for efficient transport of heat generated in the core with relatively small systems and providing grace time in case of accident situations.
- The high density of liquid metals relaxes the conditions for establishing natural circulation cooling loops in accident situations.
- The high boiling point of liquid metals mitigates issues with core voiding.
- A high efficiency for electricity production can be achieved by the application of liquid metals because of the relatively high operating temperatures that can be achieved.
- The heat transport characteristics of lead and lead-alloys allow large fuel rod pitches that result in low pressure drops and enable application of natural circulation.

The following drawbacks can be identified related to the application of liquid metal as a coolant in nuclear reactors:

- The typical high mass of liquid-metal-cooled systems (especially lead- and lead-bismuth-cooled systems) requires special measures for seismic events.
- Corrosion issues may always be present, but they increase especially at temperatures above 600°C. When operating temperatures above 600°C are envisaged, which should in principle be beneficial especially for lead and lead-alloys because they can safely operate at much higher temperatures without needing high pressure, new materials need to be developed to withstand the corrosion issues.
- In-service inspection with an opaque coolant is significantly more difficult than in transparent coolants like water and gases as optical inspection methods cannot be applied. Furthermore, the high density and elevated operation temperature of liquid metals create higher forces on inspection tools that therefore need to be specially developed and tested.
- The high melting point of liquid metals requires preheaters and measures against solidification of the coolant in case of shutdown, both during normal operation and during accident situations.
- The high density of lead and lead-alloys also leads to erosion issues in the components of the primary cooling system. This limits the coolant speed in such systems below 2 m/s, as a rule of thumb.

For a more detailed analysis on the advantages and disadvantages of adopting liquid metals, the reader is referred to [6, 9, 10]. As outlined above, a significant drawback of utilising liquid metals as refrigerants lies in the complexity of conducting experimental investigations. The measurement techniques employed in such cases are not the focus of this study; however, the reader is referred to the the LBE handbook of the OECD [11] for further information.

2.2. CFD application for turbulent heat fluxes

In the context of the objectives of the present study, among the thermal hydraulic challenges, the issue of turbulent heat fluxes will be addressed subsequently. Simulation of turbulent heat transfer in highly conductive liquid metals is of great interest

for the field and the ultimate goal is to have a RANS turbulent heat transfer model that is valid in all flow regimes, comprehensive of natural, mixed and forced convection [13].

The model proposed by Shams *et al.* [14, 15] is one of the most frequently encountered in the existing literature. It is founded upon a widely utilised approximation, namely that of constant turbulent Prandtl. Moreover, Manservisi and Menghini [16, 17] presented the $k-\varepsilon-k_\theta-\varepsilon_\theta$ model, validated by means of DNS and experimental correlations.

2.2.1. Numerical approaches

From a numerical point of view, to define the main aspects of the design of reactor cores and/or fuel assemblies, three different kinds of numerical approaches are usually adopted: the system thermal hydraulics (STH), the subchannel thermal-hydraulic (SCTH), and three-dimensional computational fluid dynamics (CFD). The system thermal hydraulic (STH) programs are one-dimensional numerical codes and treat the entire reactor core as one or a few flow channels. This approach focuses on the dynamic behavior of the entire complex cooling system and provides only average values of thermal-hydraulic parameters in reactor core or fuel assembly,

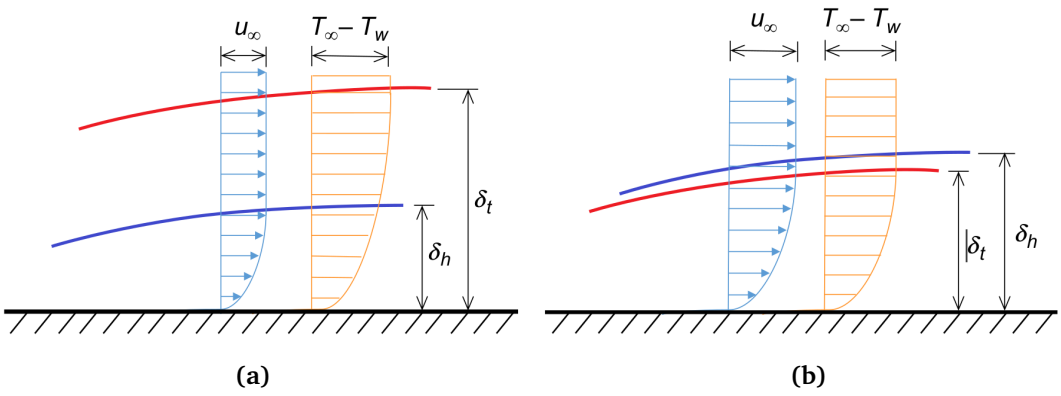

Figure 2.1: Comparison of hydrodynamic (blue) and thermal (red) boundary layers (δ_H hydrodynamic boundary layer thickness and δ_t thermal boundary layer thickness). (a) Liquid metals, (b) nonmetallic fluids (e.g., water). [12]

which usually are not sufficient for the design purpose. The SCTH analysis method is the most widely applied approach in the thermal-hydraulic design of fuel assembly and/or reactor core. Each fuel assembly is divided into a large number of individual flow channels, the so-called subchannels. With this approach, the thermal hydraulic parameters averaged over each subchannel can be obtained, and the hot test subchannels or the hot test fuel pins can be identified. CFD focuses on finer-scale phenomena where turbulent flow and heat transfer around geometric features like pins, wire wraps, and assembly cans are modeled explicitly. Due to the high requirement on the storage need and computing time, application of this approach is mostly limited to a section of one fuel assembly or even a section of one subchannel. [18]
As reported by Roelofs *et al.* [19] within CFD, a hierarchy of methods can be distinguished. A concise overview of (U)RANS (unsteady Reynolds-averaged Navier-Stokes), hybrid methods (combination of RANS and LES), large eddy simulation (LES), and direct numerical simulation (DNS) adopted for fuel assembly and pool thermal hydraulics for fast reactors can be found in Roelofs *et al.* [20]. Over the years, generic best practice guidelines have been developed and documented for the application of CFD to nuclear reactor safety: it is worth mentioning works from Menter *et al.* [21], Bestion *et al.* [22], Johnson *et al.* [23], OECD [24] and Roelofs [25].

2.2.2. High fidelity simulations

Among the CFD methods listed above, DNS provides a real picture of turbulence containing all scales of motion, from the largest scales to the smallest dissipative scales. However, the resolution of all sizes of motion comes with an enormously increased computational cost. This limits the application of the DNS to low Reynolds number flow configurations and for relatively simple geometries. Consequently, its use in the design of nuclear plants is regarded as fundamental research instrument for designing nuclear plants, providing a means of obtaining high-fidelity data that can overcome some of the limitations of experiments. Most of the state-of-the-art DNS studies assume constant material properties and only some of them are considering the buoyancy effects, resulting in scarcity of data for natural and mixed convection phenomena. [26]

With regard to the existent studies in the literature that are worth mentioning in this context there are DNSs of heat transfer in flat channels at low Reynolds numbers and different Prandtl numbers: around Pr = 1 (Kim and Moin [27], Kasagi *et al.* [28]), up to Pr = 10 (Kawamura *et al.* [29], Na and Hanratty [30])- and later on also for low Prandtl number relevant for liquid metal applications - Piller *et al.* [31], Abe *et al.* [32], Tiselj and Cizelj [33], Kawamura [34], Guo and Prasser [35].
When geometries become more complex, also the flow and temperature fields gain specific, relevant features that are not observed over planar walls. Hereafter, a selection of works on unusual geometries is reported. Errico and Stalio [36,37] performed DNS of the fully developed low Prandtl number forced convective heat transfer in a channel of high aspect ratio, having one wavy wall and one flat wall. The flow is forced and no buoyancy effects are accounted for. Oder *et al.* [38,39] and Niemann and Fröhlich [40] describe results obtained by means of DNS for a backward-facing step (BFS) at respectively Pr = 0.01, Pr = 0.005 and Pr = 0.0088.

Rod bundles play a significant role among the complex geometries of considerable interest. If nuclear reactor design is considered, fuel rod bundles are utilised for heat generation, and a parallel fluid flow through the bundles is responsable for heat removal. Rod bundle flows have been the focus of extensive research, both through experimental methods and numerical simulations, for several decades. However, in the current literature, there is a paucity of works addressing the subject of fuel bundle flow simulations relevant to low Prandtl number fluids, such as liquid metals.

In the following, an analysis of some cases from the existing literature concerning flows around rod bundles will be reported. In Section 2.3 the focus will be on rod bundles immersed in the most common refrigerant fluids, which are consequently the most extensively documented in the literature. In Section 2.4, the focus will be on studies that have taken into account the behaviour of the flow for liquid metals.

2.3. Rod bundles

Rod bundle arrangements most commonly used and documented can be classified as follows (Figure 2.2):

- regular triangular array of rods within an hexagonal channel
- regular square array of rods within a square channel
- circular array of rods within a circular channel

The main geometrical characteristics adopted to describe rod bundles are: the rod outside diameter D, the pitch P defined as the distance between the rod centers, the distance W from the wall defined as rod diameter plus the shortest distance between a rod and the channel wall and number n_R of rods in a rod bundle.

2.3.1. Bare rod bundles: laminar flow

Laminar flow has been widely investigated in bare rod bundles. In specific ranges of P/D, usually below 2.5, and subchannel rows far from the wall, the treatment of flow around rod bundles by individual subchannels is quite accurate: this approximation entails the absence of momentum transport across the boundary between adjacent subchannels, and it is applicable to laminar flow. In regular and infinite arrays of rods with axisymmetric and uniform heat generation, this assumption is also valid for laminar flow heat transfer. However, in actual practice, the presence of fixed duct walls, variations in heat generation across the rod bundles, large rod spacing and entrance effects may render subchannel analysis an approximation and

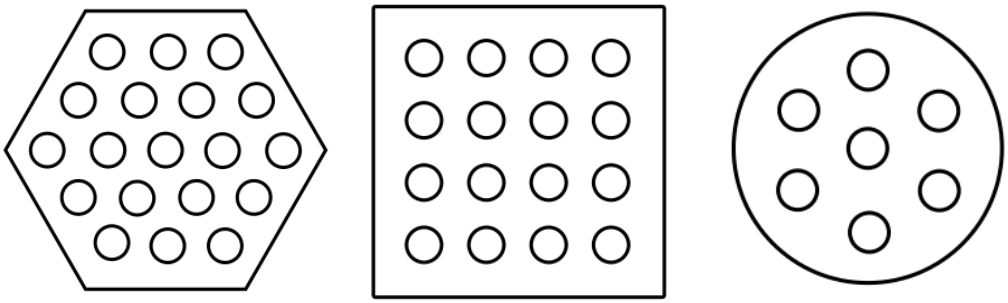

Figure 2.2: Rod bundle arrangements: (a) triangular arry within an hexagonal channel, (b) square array within a square channel, (c) circular array within a circular channel.

the necessity for a multiregion or multicell analysis arises. Rehme [41] highlights that the majority of the knowledge regarding friction factors and Nusselt numbers is derived from theoretical analyses. The lack of experimental data is primarily ascribed to the difficulty in measuring minor pressure fluctuations in laminar flow. Rehme [41] reports several solutions for fRe for central, wall and corner subchannels, for both triangular and square arrays, under fully developed or developing flow conditions.

2.3.2. Bare rod bundles: turbulent flow

Contrary to laminar flow, research on turbulent flow through rod bundles has been predominantly experimental, with more focus on pressure drop and less on heat transfer, as the latter is more expensive. Measuring heat transfer requires many precise temperature sensors (often embedded in rods, walls, and coolant), calibrated heaters, and high-accuracy data systems. A theoretical approach has also been considered, but it is worth noting that this involves the validation of turbulence models, which can only be carried out through experimental data. In the context of nuclear applications, subchannel analysis is widely employed to compute temperature distribution, averaged on subchannels. However, measuring subchannel friction factors and heat transfer coefficient is challenging due to:

- the presence of the walls, which affect the pressure drop and the overall flow distribution among subchannels
- inaccurate knowledge of the cross flow section and wetted perimeter (mostly for very early experiments)
- the presence of spacer grids, which affect the pressure drop

Consequently, in order to estimate subchannel friction factors, it is necessary to measure wall shear stresses and velocities in detail and the evaluation of these parameters is prohibitively expensive. Once more, Rehme [41] presents comprehensive findings on friction factors derived from experimental analysis and, additionally, offers insights into velocity distributions and pressure drop from a range of theoretical works that exhibit significant inconsistencies. If square arrays are considered, the

available experimental data are extremely limited. Therefore, the findings of $f\,\mathrm{Re}$ from laminar flow have been adapted to study friction factors in turbulent flows.

In order to recalibrate existing correlations, which are often based on very early experiments, or turbulence models (especially for more complex geometries - Section 2.3.3 - or unconventional coolants - Section 2.4), availability of high-fidelity data is essential.
A comprehensive review of early simulation of bundle flows for nuclear application is reported by Grötzbach and Wörner [42]. Among the most recent studies , Kraus *et al.* [43] performed DNS for a 5 by 5 square rod bundle representative of light water reactor fuel. The high-fidelity calculations were performed using Nek5000 [44]. The DNS was run at a Reynolds number of 19,000. For boundary conditions, a no-slip condition was applied at the cylindrical and square walls and periodic conditions were used in the streamwise direction.
Figure 2.3 reports findings for the average streamwise velocity: in the inner subchannels, the flow behaves similarly to canonical turbulent channel flow and the streamwise velocity matches standard log-law behavior, while the edge and corner subchannels have clear differences. The parallel and wall-normal components of the velocity show significant differences (refer to [43] for the details of instantaneous wall-parallel velocity in channel centerlines). For the edge channel, the wall-parallel components form large, organized structures that coincide with the gap centers and behave in a way that resembles vortex shedding. This behavior might indicate that the gaps themselves are causing an instability in the flow, which as been previously observed in [45].
The streamwise Reynolds stresses show the usual two peaks near the channel walls, and the lateral stresses exhibit similar but weaker patterns. However, the edge-gap region behaves differently: the streamwise stress is much smaller due to lower shear, and the lateral stresses lose their typical dual-peak shape (Figure 2.4a), forming instead a single strong peak at the gap center—especially in the wall-parallel component (Figure 2.4b). This indicates that turbulence there is driven not by mean shear but by geometric and intrinsic flow effects, supporting the presence of a gap vortex street.
Furthermore, DNS provides the ability to analyse secondary flows characteristics

which are important for interchannel mixing and heat transfer,. The lateral velocities are of the order of 1% with respect to the bulk velocity. The cross flows show that in wide gaps the flow moves toward the subchannel center while in narrow gaps the flow moves toward rod surfaces.
The paper also reports findings for the turbulent kinetic energy (TKE) budget. DNS resolves all relevant scales and it is possible to balance and quantify each term in this budget for steady flows. This detailed information is valuable for understanding turbulence mechanisms and for validating lower-fidelity turbulence models. Central subchannels behave similarly to canonical channel flow: outside of the boundary layer, production and dissipation are typically the dominant terms while redistribution effects matter only near the wall. In contrast, the edge subchannel exhibits clear signs of a gap vortex: at its center, production nearly vanishes and turbulent transport becomes the main TKE source, indicating that turbulence there is imported from other regions rather than generated locally.

2.3.3. Spacer grids and wire wrapped

Bubelis and Schikorr [46] addressed a recurrent problem in thermal-hydraulics by examining the existing correlations for friction factors of wire-wrapped rod bundles (Figure 2.5). It was noted that, while numerous correlations had been derived, these had been developed for a restricted range of experiments, frequently involv-

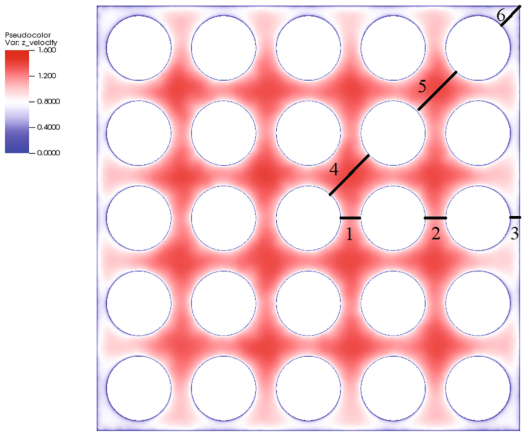

Figure 2.3: Average streamwise velocity in a 5x5 rod bundle obtained by DNS. [43]

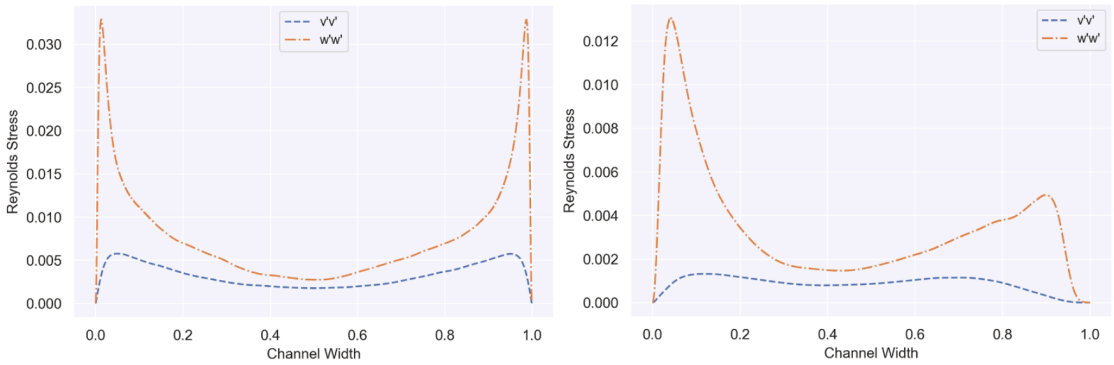

Figure 2.4: Reynolds normal stresses for (a) line 4 and (b) line 6. For these lines $u'u' = v'v'$. [43]

ing a single coolant and a specific geometry. A a result, the application of these correlations in domains other than their original one frequently yields unreliable predictions. Bubelis and Schikorr [46] review the major correlations available, including models from Novendstern [47], Rehme [48], Engel *et al.* [49], Cheng and Todreas [50], Baxi and Dalle-Donne [51] and Sobolev [52]. Some correlation stand even in modified forms, where adjustments have been made to ensure compatibility with particular datasets. The review reveals that while many correlations can fit specific cases, the Rehme correlation stands out as the most universally applicable across fluids, geometries, and Reynolds number ranges. Moreover, Sobolev, Novendstern, Engel (modified), Baxi and Dalle-Donne (modified) demonstrate a satisfactory degree of agreement. Nevertheless, Bubelis and Schikorr propose that more rigorous quantitative comparisons are required, and agree that new datasets should be generated in order to strengthen validation.

More recently, Fan *et al.* [53] examine how pressure varies not only along the length of the bundle but also across it, and how these variations relate to the helical geometry of the wire wrap spacers. This is one of the lesser-explored aspects of thermal hydraulics in wire-wrapped rod bundles and to address this reasearch gap they designed experiment on a transparent polymethyl methacrylate 19-pin assembly. The results indicate that axial pressure in the edge subchannels displays a non-linear relationship with distance, exhibiting a repeating helical periodicity that aligns with the pitch of the wire wraps. In the transverse direction, the pressure field is found to

rotate in phase with the wire wraps. The direction of rotation and the relative heights of the wire spacers at given cross-sections are significantly affecting local pressure distribution. This experimental result provides strong evidence that computational studies were correct in their predictions. Specifically, the data demonstrate that wire wraps not only increase mixing and drag, but also shape the cross-flow in a periodic, geometry-dependent way. The obtained data are then compared with several classic friction-factor correlations as the ones listed above. This analysis confirmed that the Rehme [48] correlation best fits the cases under consideration.

Zhao *et al.* [55] focus on cross-flow in a wire-wrapped hexagonal seven-pin fuel bundle. The simulation of transverse flow is conducted utilising OpenFOAM software [56], with a comprehensive investigation undertaken into the impact of significant parameters. Specifically, the effects of the Reynolds number (in the range 6000-100,000), the helical pitch-to-pin diameter ratio (in the range 12-24), and the pitch-to-pin diameter ratio (in the range 1.11-1.22) are examined. The analysis highlights that the Reynolds number has a minor effect on the transverse flow, while the bundle geometry parameters, such as H/D and P/D, influence the transverse flow prominently. In particular, the transverse velocities increase with the decrease of H/D or the increase of P/D. Moreover, Zhao *et al.* make a comparison between the results and some existing correlations (Wantland [57], Naveen Raj and Velusamy [58]), highlighting discrepancies due to the P/D influence being ignored. In their study, Yoon and Heidet [59] evaluate the existing friction factor correlations for 217 pin wire-wrapped fuel rod bundles of SFR and the range of applica-

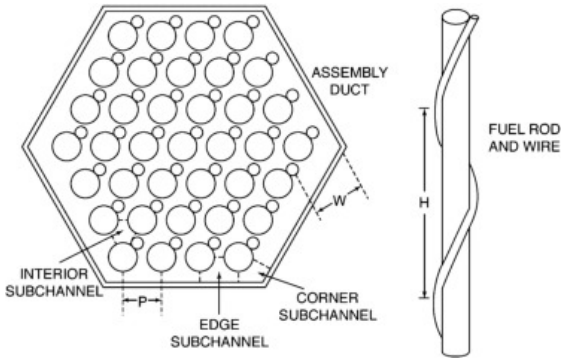

Figure 2.5: Assembly duct and with wire-wrapped fuel rod. [54]

Table 2.1: Applicable ranges of the existing friction factor correlations for wire-wrapped rod bundles [59]

Correlation	Year	n_R	P/D	H/D	Reynolds number
Novendstern [47]	1972	19 - 217	1.060 - 1.420	8.0 - 96.0	Transition & turbulent 2600 - 10^5
Rehme [48]	1973	7 - 217	1.100 - 1.420	8.0 - 50.0	Transition & turbulent 1000 - 3×10^5
Engel *et al.* [49]	1979	19 - 61	1.067 - 1.082	7.7 - 8.3	All regimes 50 - 10^5
Baxi and Dalle Donne [51]	1981	19 - 217	1.060 - 1.420	8.0 - 96.0	All regimes 50 - 10^5
Cheng-Todreas (Detailed) [50]	1986	19 - 217	1.000 - 1.420	4.0 - 52.0	All regimes 50 - 10^6
Cheng-Todreas (Simplified) [50]	1986	19 - 217	1.025 - 1.420	8.0 - 50.0	All regimes 50 - 10^6
Upgraded Cheng-Todreas (Detailed) [54]	2018	7 - 271	1.000 - 1.420	8.0 - 52.0	All regimes 50 - 10^6
Upgraded Cheng-Todreas (Simplified) [54]	2018	19 - 271	1.025 - 1.420	8.0 - 50.0	All regimes 50 - 10^6

bility of these correlations for the purpose of identifying the preferred one for SFR analysis. Table 2.1 presents an interesting summary of the existing friction factor correlations considered, including the relevant ranges for each of them. The Engel, Markley and Bishop [49] correlation, Novendstern [47] correlation and Baxi and Dalle Donne [51] correlation show the relatively inaccurate prediction of friction factor in some or all of the flow regimes. The relative differences among the Rehme [48] correlation, Cheng and Todreas detailed correlations (original [50] and upgraded [54]) are approximately ±10%, which is less than the typical experimental measurement uncertainties.

Ahmad and Kim [60] conducted a three-dimensional investigation of flow and heat transfer in a wire-spacer fuel assembly for a liquid-metal reactor using RANS analysis. The SST turbulence model was employed as the closure model for a compu-

tational domain for a 7-pin wire-spacer fuel assembly. The SST model was selected because it accurately captures flow separation under adverse pressure gradients and provides reliable near-wall turbulence predictions, which are essential for modelling turbulent heat transfer. The results indicate that the largest region of low axial velocity occurs downstream of the wire-wrap as it moves through the inter-pin gap. A significant recirculating zone forms behind the wire-wrap within the interior subchannel. These flow features strongly influence the accurate prediction of coolant temperature within the fuel assembly.
Gajapathy et al. [61] provided detailed flow and temperature distributions needed for realistic evaluation of thermal-hydraulic parameters. Their work considered fuel pins of 6.6 mm diameter arranged in a triangular pitch and employed the standard high-Reynolds-number $k-\varepsilon$ turbulence model [62]. The helical wire produces a secondary flow that significantly enhances coolant mixing, promoting temperature uniformity and increasing turbulence levels. However, it also contributes to higher pressure drop. Friction-factor predictions from Rehme's correlations were compared with CFD results: the CFD model under-predicted friction factors at low Reynolds numbers but over-predicted them at high Reynolds numbers. The study further confirms that the helical wire induces a secondary swirl in the bundle, enhancing cross-stream mixing and improving coolant-temperature uniformity.

Bieder *et al.* [63] in their work investigate how RANS and LES approaches using wall functions perform in predicting pressure losses and velocity distributions in wire-wrapped fuel rod bundles. They also outline how the majority of recent publications on wire-wrapped fuel assemblies employ wall-resolved modelling, as described by Dovizio *et al.* [64]. Furthermore, they highlight the sensitivity of the wire-wrapped rod bundle configuration to the refinement of near-wall discretisation and the turbulence model, as evidenced by Song *et al.* [65]. Bieder *et al.* [63] conducted sensitivity tests on geometry effects to better understand the effects of the wires. In particular, they studied a spatially fully developed, straight wire spacer (not helical) with periodic boundary conditions, a spatially developing configuration with an helical wire spacer with an inflow boundary condition from the first configuration and finally a spatially fully developed helical wire spacer with periodic boundary conditions. The helical spacer wires induce three-dimensional secondary flows that

increase resistance with respect to straight wires; these 3D effects are not fully captured by wall functions, leading to pressure overprediction.
Moreover, Bieder *et al.* [63] conducted a sensitivity analysis on the influence of the number of rods (7 - 19 - 37 - 61). While the experimental correlations (Blasius, Rehme, Cheng & Todreas) show a slightly increment of the pressure loss with the increasing number of rods, RANS with wall functions predict a near-constant pressure loss across all configurations and consistently overestimate experimental and empirical correlation values by 10 - 20 %.
Also a quantitative comparison of velocity profiles and flow distribution is made for a 61-pins rod bundle configuration: the findings agreed reasonably well with wall-resolved RANS and LES, capturing major flow patterns and swirl induced by spacer wires. However, pressure losses are once again overestimated (around 20%) compared to both experiments and correlations. This discrepancy is attributed to inadequate wall treatment in low-velocity regions and near-wall cells.
In the last part of their work, the authors present some LES results. Overall, a good agreement is observed between the LES with wall functions, the PIV measurements, and the wall-resolved LES, although some local discrepancies remain. Compared with the wall-resolved simulations, the wall-function approach predicts slightly higher axial velocities in the peripheral sub-channels, especially in the wake of the wire spacers. The finer near-wall mesh resolution of the wall-resolved model allows a more detailed capture of small-scale flow structures, such as the swirling motion near the lower shroud wall.

Roelofs *et al.* [66] provide a comprehensive overview of recent international activities with a focus on the validation of CFD techniques for 'as designed' assemblies with wire-wrapped bundle configurations (Table 2.2). The available reference data include 3-pin bundles, with the domain size increasing until reaching full-scale fuel assemblies of 217-pin bundles, and and ultimately extending to an infinite-pin bundles. The larger bundles are more indicative of the actual situation, with the infinite bundle being purely hypothetical and primarily serving the purpose of code validation. The inherent uncertainties associated with both experiments and simulations result in variations in the accuracy of CFD implementation. In the context of the wire-wrapped pins, the contact between the pin and wire is considered as a distinc-

tive source of uncertainty: two approaches are currently employed for the modelling of this charateristic, the open and closed gap contact. In the case of open gap contact, a small space is modelled between the wire, which is fixed to one pin, and the next pin. In the case of closed gap contact, a small surface contact is modelled to fill this gap. Delchini *et al.* [67] demonstrate that the friction factor remains unaffected by the contact-point model and the incorporation of boundary layers on wall boundaries. Another uncertainty to consider when investigating wire-wrapped rod bundles is their deviation from the original design specifications [68, 69]. Deformation occurs even under normal operating conditions: this is due to a number of factors, including tension in the pre-stressed wires, contact pressure between the clad and adjacent rods' wires, thermal and irradiation clad creep, irradiation-caused swelling and fuel burn-up. Therefore, an evaluation of the consequences of deformation on both the flow and heat transport is necessary. Mays *et al.* [70] illustrate that these wire-wrapped fuel assembly components undergo deformation over time during standard operation, resulting in substantial alterations to the core thermal-hydraulic systems.

As previously stated, a prevalent configuration in nuclear reactor assemblies that enhances turbulent mixing and heat exchange is the presence of grid spacers. Furthermore, the presence of spacer grids ensures that the distances between rods are always kept constant within the assembly: this is crucially important when, for instance, cooling fluids such as liquid metals are employed, as these are very dense and can cause stresses that could alter the position of the rods. Common practice is to experimentally develop correlations, where a wide variety of data is reported in the literature where various shapes of spacers have been analyzed. However, researchers widely have investigated spacer grid design influences in a rod bundle also by means of CFD. Among these some examples can be mentioned.

As for wire-wrapped rod bundles, RANS simulations were used to predict the mixing and the pressure losses induced by spacer grids, showing strong sensitivity to turbulence-model choice [90]. Batta and Class [91] conducted RANS simulations on a 19-pin LMFR fuel assembly with grid spacers, for regular and reversed flows through their rod bundle. In this study they account CFD as a valuable tool: the

Table 2.2: Overview of experimental data and corresponding RANS references [66]

Reference data	Reference literature	Fluid	Reynolds number /1000	Reference RANS
3-pin JAEA	Nishimura *et al.* [71]	Water	3 ÷ 15	Nishimura *et al.* [71]
7-pin LES	Merzari *et al.* [72]	Sodium	22 ÷ 50	Merzari *et al.* [72]
7-pin SEEDS-2	Bertocchi *et al.* [73]	Water	4 ÷ 15	Dovizio *et al.* [74]
19-pin KAIST	Chun *et al.* [75]	Water	0.1 ÷ 60	Chen *et al.* [76]
19-pin ESTHAIR	Berthoux *et al.* [77]	Air	0.4 ÷ 27	Berthoux *et al.* [77]
19-pin NACIE	Di Piazza *et al.* [78]	LBE	1 ÷ 15	Doolaard *et al.* [79]
19-pin KALLA	Pacio *et al.* [80]	LBE	14 ÷ 48	Pacio *et al.* [81]
61-pin TAMU	Nguyen *et al.* [82]	p-cymene	4 ÷ 19	Goth *et al.* [83]
61-pin AREVA	Mays *et al.* [70]	Water	19	Mays *et al.* [84]
61-pin LES	Goth *et al.* [83]	p-cymene	19	Dovizio *et al.* [74]
127-pin JAEA	Narita *et al.* [85]	Water	19 ÷ 70	Jeong *et al.* [86]
127-pin COMPLOT	Kennedy *et al.* [87]	LBE	4 ÷ 35	Kennedy *et al.* [87]
217-pin IGICAR	Naveen Raj *et al.* [58]	Water	87	Naveen Raj *et al.* [58]
∞-pin LES	Saxena [88]	Sodium	55	Saxena [88]
∞-pin q-DNS	Shams *et al.* [89]	LBE	7	Dovizio *et al.* [74]

results show that all the studied cases are equivalent according to the correlations and but there is a substantial difference in their pressure losses. CFD studies can be performed employing the actual geometry of the spacer including all its geometrical features allowing to study these effects in detail providing very good accuracy. Mathur *et al.* [92] investigated flow effects for nominal flow and accident conditions

due to partial blockages in 19-pin and 127-pin rod bundles with a hexagonal spacer using a wall-resolved reduced-resolution RANS approach. The study demonstrates how the method is consistent with experimental results for nominal flow conditions. However, in presence of partial blockages a larger flow recirculation zone than that observed in the experiments is predictied, leading to an over-prediction of temperature in the wake of the blockage. This finding highlights the necessity of a comprehensive understanding of the physics of the flow, thereby prompting Mathur *et al.* to conclude that further studies are required to analyse modelling aspects such as turbulence modelling, turbulent heat flux modelling or conjugate heat transfer modelling.

To analyse these modelling features, reference should be made once again to high fidelity data, where available. Early benchmark experiments have always been used as fundamental datasets for rod bundle flows with spacer grids using Laser Doppler Velocimetry and tailored test rigs, forming the basis for CFD validation [93, 94]. More recently Neumeister *et al.* [95] published a comprehensive overview of studies on Pressure Water Reactors (PWR) and Boiling Water Reactors (BWR) employing rod bundles with spacer grids. For LMFR assemblies with spacer grids, very scarce experimental research is available in recent literature related to flow dynamics and thermal hydraulics [5].

2.4. Rod bundles: low Prandtl number fluids

In 2013, Grötzbach [2] drew attention to certain significant aspects concerning the thermal hydraulic peculiarities of turbulent liquid metal flows.

Liquid metals are characterised by a high thermal conductivity. In fluids with Prandtl number around one, the statistical properties of the turbulent velocity and temperature fields are analogous, and the diffusive and conductive wall layers exhibit a comparable thickness. With decreasing Prandtl number the conductive heat flux is near walls increasing in importance and there is no similarity between time-averaged velocity and temperature profiles. Furthermore, with respect to the nuclear applications, they are within the transition range, where turbulent heat flux is predominantly influenced by both conduction and convection, thereby making its effects particularly significant. This is in contrast to high Reynolds regimes, where the tur-

bulent thermal diffusivity significantly exceeds the molecular thermal diffusivity. Grötzbach's analysis of the energy spectra for temperature and velocity fluctuations revealed that as the Prandtl number decreases, the increasing thermal diffusivity reduces the amplitude of temperature fluctuations and strongly damps them at small scales. For low-Pr flows, evidence suggests that the temperature spectra shift toward lower wavenumbers. Moreover, since the magnitudes of both velocity and temperature fluctuations vary with the wall distance, all these spectra also depend on the wall-normal coordinate. This offers a particular advantage for LES of low-Pr fluids, as it becomes easier to capture most, or even all, temperature fluctuations directly and presents the opportunity to eliminate the need for subgrid-scale (SGS) heat flux models.

RANS are a widely employed tool for detailed analyses of experiments and reactor components, including those involving liquid metals. However, a considerable amount of uncertainty is associated with the turbulence modelling of the velocity fields. In forced flows these can be reduced to a minimum by selecting the best suited momentum transfer model. In the case of bundle flows, it is well-established that the turbulent momentum transfer is highly anisotropic; as a result, anisotropic turbulence models are required in order to reproduce the local variations of mean flow data and secondary currents [96]. In strongly buoyancy influenced flows, when the temperature is no longer a passive scalar, it is crucial to calculate the temperature with precision. This is due to the fact that the temperature becomes an important component of the source term for the velocity field. It is also important to note that buoyant flows are, in principle, highly anisotropic. While commercial CFD codes account for buoyant flows to some extent, their adaptations remain limited.
The common modelling of the turbulent heat flux term $\overline{u_i' T'}$ in currently available RANS heat flux modelling methods is based on the following assumption:

$$\overline{u_i' T'} = -\varepsilon_h^{il} \frac{\partial \overline{T}}{\partial x_l} \tag{2.1}$$

Where the tensor ϵ_h^{il} stand for the eddy conductivity. In most models the anisotropic ε_h^{il} tensor is replaced by an isotropic scalar ε_h. Then the Reynolds analogy is applied and similarity is assumed in the turbulent transport features of momentum and heat,

and thus the isotropic eddy conductivity ε_h is assumed to be proportional to the eddy diffusivity for momentum ε_m. The proportionality factor is the inverse of the turbulent Prandtl number Pr_t:

$$\overline{u_i' T'} = -\varepsilon_h^{il} \frac{\partial \overline{T}}{\partial x_l} \approx -\varepsilon_h \frac{\partial \overline{T}}{\partial x_i} = -\frac{\varepsilon_m}{Pr_t} \frac{\partial \overline{T}}{\partial x_i} \tag{2.2}$$

with $Pr_t = \varepsilon_m / \varepsilon_h$. Consequently, the issue of closing the model is transferred to the factor Pr_t. The turbulent Prandtl number is defined by the turbulent shear stresses, the gradient of the velocity field, the turbulent heat flux and the gradient of the temperature field. These variables are not similar in liquid metal flows: thus Pr_t is not constant and depends on many parameters (Re_τ, Pr, wall distance).
The majority of CFD users still apply a constant turbulent Prandtl number ($Pr_t = 0.9$) for all flow types, Prandtl numbers, and shear stress models, despite its inaccuracy for low Prandlt number fluids. A significant challenge that remains to be addressed is the procurement of reliable experimental data for turbulent heat flux modelling in non-adiabatic liquid metal channel flows, since Pr_t is subject to variation due to the gradients of the mean fields and the characteristics of turbulence. While some DNS data for low Reynolds flows exist, most current datasets are characterised by inadequate large-scale resolution to support improved model development.
Grötzbach reports an interesting discussion on more advanced, transport-equation-based approaches for modelling turbulent heat fluxes. Unlike gradient-based models, algebraic heat flux models (AHM) formulations can handle counter-gradient fluxes and include buoyancy effects explicitly. In the model developed by [97], for example, the turbulent heat flux depends not only on the mean temperature gradient but also on velocity gradients, gravitational terms, and dissipation effects. The buoyancy term, in particular, becomes dominant in natural or mixed convection and allows the model to represent anisotropic heat transport realistically.
Grötzbach also considers full second-order heat flux models, which explicitly solve the transport equations for all components of the turbulent heat flux vector and the temperature variance. These models [98, 99], extended for liquid metal applications by Carteciano and Grötzbach [100], provide the most detailed description of turbulent heat transfer in buoyant flows. Further refinements were introduced by Chandra and Grötzbach [101]: they demonstrated that accurate modelling of tur-

bulent heat fluxes in buoyant, low Prandtl number flows requires accounting for anisotropy, non-equilibrium effects, and variable time scales, which are absent in the simpler approaches. Despite their advantages, these advanced models are not yet widely implemented in commercial CFD codes. Grötzbach emphasises the necessity of further development, calibration, and validation of models prior to their reliable application to actual engineering problems. Progress in this direction is predominantly impeded by the scarcity of high-quality experimental and DNS data at Reynolds and Rayleigh numbers that are pertinent to nuclear systems. In the development of their four-parameter heat transfer turbulence model, Manservisi and Menghini [16, 17] highlight how the validation has been accomplished by means of DNS data of plane geometry, which is one of the most commonly encountered in the literature. Nevertheless, the correlations derived for heat exchange in square and triangular lattice geometries are not satisfactory solutions. In this regard, the authors attribute the elusiveness of the problem to the absence of reliable data on rod bundles.

In 2019, Shams *et al.* [102] also discussed the topic of turbulence models for low Prandtl number in the framework of the EU SESAME project. The paper covers the same models illustrated by Grötzbach implemented through three different CFD solvers - STAR-CCM+, OpenFOAM and TransAT (ASCOMP). Different combinations of momentum and heat flux closures are tested selecting three canonical cases representative of natural, mixed and forced convection regimes at low Prandlt numbers. For natural convection a Rayleigh–Bénard cell is analysed: the reference case is a DNS conducted by Otic *et al.* [103]. For mixed convection a planar channel with differentially heated walls, reference case from Guo *et al.* [104]. For forced convection a planar impinging jet, reference case from Duponcheel and Bartosiewicz [105]. The AHFM-NRG+ (Algebraic Heat Flux Model - NRG version) model , a further calibration of the model AHFM-NRG [106] proposed by Shams [89], is indeed a model that introduces coefficients that depend on Prandtl and Rayleigh and stands out as the most suitable for natural and mixed convcetion cases in the prediction of temperature and velocity field; additionally it gives a good outcome for forced convection configurations. The results from this work highlight the need for a well-calibrated and sophisticated turbulent heat flux model for applications with low Prandtl fluids, especially when buoyancy effects play a significant role. On the other hand, they as-

sessed that the TMBF-eq-ATHFM [100] model shows instability and large local errors near stagnation points.

2.4.1. High fidelity simulations

In the context of high-fidelity data aimed at broadening the spectrum of available data on low Prandtl number fluids, here are briefly reported some noteworthy findings.

Lai *et al.* [107] performed a DNS of turbulent flow and heat transfer in bare rod bundles with a low P/D ratio of 1.107, representative of nuclear reactor fuel assemblies. The study explores how different Prandtl numbers affect turbulence and heat transfer characteristics and it is of high importance in the context of models validation. The high-order technique of spectral element method is chosen for DNS, using the software Nek5000. The accuracy of the DNS is confirmed by the analysis of velocity and shear stress contributions, which have been shown to satisfy the law of the wall. Moreover, turbulent kinetic energy (k) distributions are consistent with experimental data. However, Lai *et al.* hypothesise that the difficulty of RANS models in predicting turbulent kinetic energy may be attributed to variations caused by geometric aspects. In the specific case being considered here, an initial peak in fluctuations is found before they begin to decay towards regions far from the walls. One feature that can be observed is that the maximum normalized k decreases as the angle approaches the centre of the gap between the two rods.
Detailed Reynolds stress transport terms are also analysed: near the walls the production term is dominant while towards the center of the channel turbulent transport and dissipation balance energy. At gap centers between adiacent rod bundles, the Reynolds stresses are mainly transported by the turbulent fluctuations in the triple velocity correlation, feature that is especially challenging to capture with a pure RANS model.

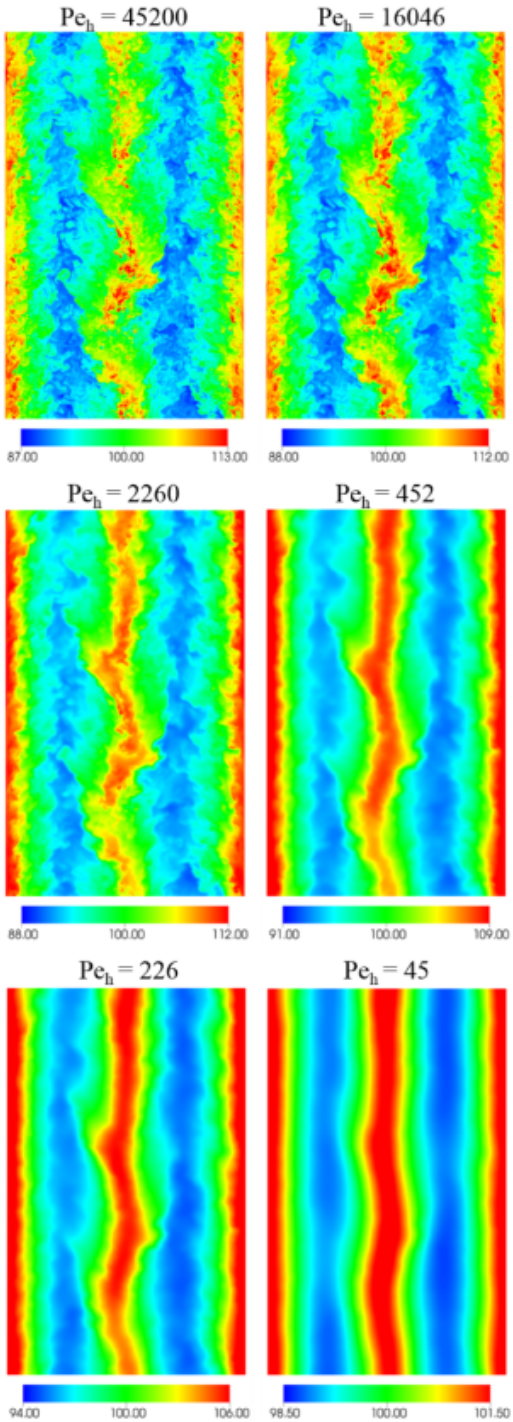

Figure 2.6: Instantaneous temperature contours for different Peclet numbers at the same time frame. [107]

The most interesting aspect to be considered from Lai *et al.* work is the effect of Prandtl number on heat transfer. As Prandtl decreases, thermal diffusivity dominates momentum diffusion. High thermal conductivity in low Prandtl number fluids leads to uniform temperature fields even in complex geometries, with weaker gradients near the wall, as shown for Peclet number of 45 in Figure 2.6. If the gap between rod bundles are considered, the proximity of this location to adjacent center rod results in the radial temperature becoming exceedingly high, leading to almost no variation in radial temperature distribution.
The location of the maximum root mean square (RMS) temperature fluctuation depends strongly on Prandtl: if Peclet number is high, the tren is similar to that of turbulent kinetic energy. However, once the correlation between conductivity and viscosity is no longer valid, the profile becomes much different. The findings demonstrate that the shape of the temperature fluctuations is influenced by the Peclet number, thereby posing a challenge for those modelling heat transfer in this geometry.
Lai *et al.* confirm the results obtained by Grötzbach [2] about the energy spectra of temperature fluctuations: at low Prandtl number, energy is transported with larger scale motions, while transport through smaller eddies is less dominant because of the high value of thermal conductivity.
More recently Zhou *et al.* [108] conduct experimental measurements and CFD simulations to investigate local flow and heat transfer behavior of LBE. A single-rod experiment is performed and a new empirical correlation for the Nussel number is fitted, valid for valid for $P/D = 1.92$ and $Pe \geq 300$. The correlation is validated through CFD studies of three benchmark experiments - the XJTU 7-rod [109], KIT 19-rod [110], and ENEA 37-rod bundles [111] - using the $k-\omega$ SST turbulence model and a turbulent Prandtl number of 1.5. The simulations successfully reproduce experimental temperature and heat transfer data, with temperature deviations below ±10°C and section-averaged Nusselt number deviations below ±25%. It is noteworthy that the outcomes are profoundly influenced by the selection of the turbulent Prandtl number. To select the value of 1.5, a sensitivity study on this parameter was previously conducted by the authors, varying it between four values (Pr_t = 1.5,2.0,2.5,3.0) and selecting the one that yielded the result most consistent with the reference experiment [109].

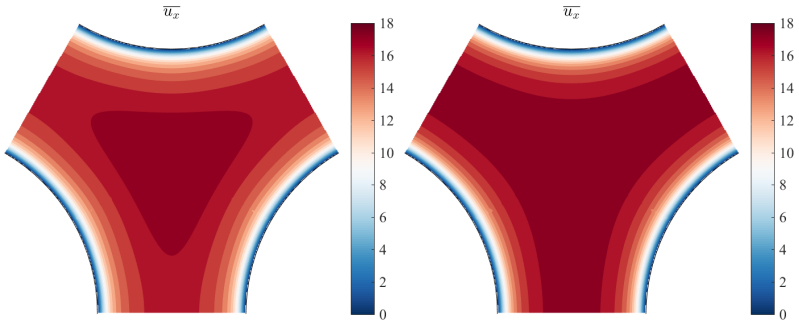

(a) **(b)**

Figure 2.7: Contours of $\overline{u_x}$ in a subchannel for (a) Ri = 0 and (b) Ri = 0.22. [112]

2.4.2. Forced, mixed and natural convetion

Grötzbach [2] outlines that heavy liquid metals often allow for transport of large amounts of thermal energy with rather moderate velocities. As a consequence, strong distortions of the velocity field and its turbulence could be expected due to buoyancy forces. An increase of Nusselt number Nu is found by buoyancy augmented convection at low Re, but also a reduction of Nu by some local relaminarisation at quite high Re. This means, that not only gaining separate effect data for turbulence model development may be quite challenging, but also the selection of adequate models for CFD applications to non-adiabatic liquid metal flows.

Angeli *et al.* [112] report results of DNS of turbulent flow around a triangular bundle of heated rods, cooled by a liquid metal (namely Liquid Lead-Bismuth Eutectic). The computational domain includes four subchannels of a bundle with a pitch-to-diameter ratio of 1.4. Simulations are carried out in both forced (Ri = 0) and mixed convection conditions (Ri = 0.22). The bulk Reynolds number is Re_b = 8290 for Ri = 0 and Re_b = 8650 for Ri = 0.22.

Some relevant results from [112] are provided to facilitate a better understanding of the behaviour of the fluid under conditions of forced or mixed convection. Figure 2.7 shows contours of the average streamwise velocity u_x, for both forced and mixed cases. The effect of buoyancy can be observed: for Ri = 0 (Figure 2.7a), the maximum velocity is found at the centre of the subchannel, while, for Ri = 0.22 ((Figure 2.7b)) the velocity at the center of the narrow gap almost equals that of the

subchannel and the velocity gradients between the large and narrow gaps are much smaller.

The flow about rod bundles in triangular or square arrangements is characterized by non-zero time-averaged cross-flow components, determined by gradients of the mean streamwise velocity between large and narrow gaps. Figure 2.8 report contours of the magnitude of the time-averaged cross-flow velocity vector $\overline{\boldsymbol{u}_\perp} = (\overline{u_y}, \overline{u_z})$, alongside with streamlines of the cross-flow components on the unit flow cells. The circulation is driven towards the rods in the narrowest gap, while it is directed towards the center of the subchannel in the largest gap. For Ri = 0, the intensity of these secondary flow components is around 0.2% of the bulk velocity. As it can be appreciated in the map of Figure 2.7b, in the present case buoyancy determines a strong decrease of the magnitude of $\overline{u_\perp}$, of about 50%, in the large gap, while in the narrow gap the profiles differ from each other only for a shift in the location of the peak value. The attenuation of secondary flow components is a direct consequence of the decrease of the velocity gradients observed between the narrow and large gap.

Figure 2.9 reports contours of average turbulent heat fluxes $\overline{u_x'\theta'}$. From the comparison between the maps at Ri = 0 and Ri = 0.22, again, an overall decrease of the turbulent heat fluxes emerges in the mixed convection case. From their comprehensive analysis, Angeli *et al.* conclude that the velocity fluctuations and the associated reduction in Reynolds stresses due to buoyancy lead to decreased temperature fluc-

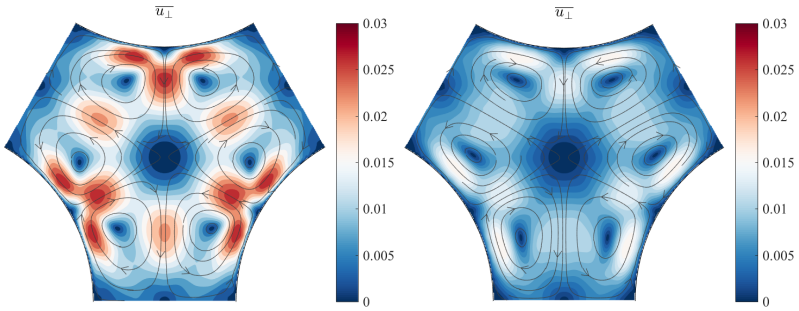

(a) **(b)**

Figure 2.8: Contours of $|u_\perp|$ in a subchannel and computed cross-flow recirculation pattern for (a) Ri = 0 and (b) Ri = 0.22. [112]

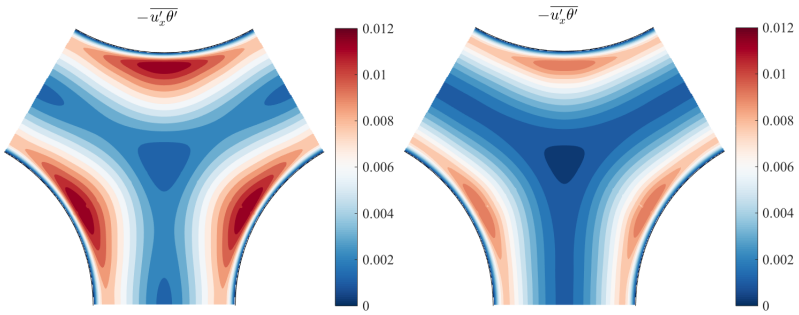

(a) **(b)**

Figure 2.9: Contours of $-\overline{u_x\theta}$ in a subchannel for (a) Ri = 0 and (b) Ri = 0.22. [112]

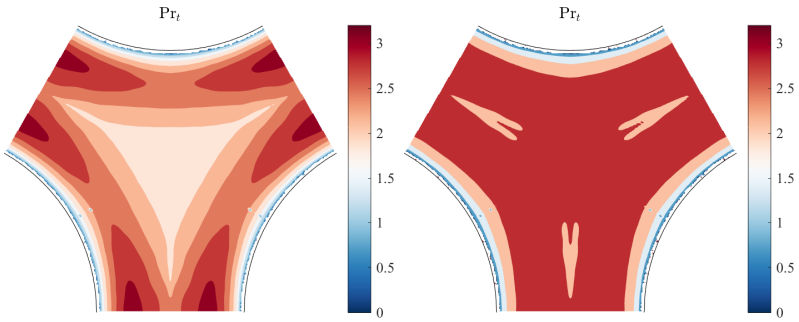

(a) **(b)**

Figure 2.10: Contours of Pr_t in a subchannel for (a) Ri = 0 and (b) Ri = 0.22. [112]

tuations and turbulent heat fluxes. These effects are therefore responsible for the slight reduction in the overall Nusselt number compared with the purely forced case, which decreases from 12.82 to 12.65.

Moreover, distributions of the turbulent Prandtl number Pr_t over a subchannel are reported in Figure 2.10. Although a maximum value of $\mathrm{Pr}_t \approx 3$ is reached in both the forced and mixed convection case, interestingly, near-wall gradients of Pr_t are much steeper for Ri = 0.22. This suggests that turbulent diffusion of heat moving from the wall to the bulk of the flow becomes lower if buoyancy is present.

2.5. Summary

The bibliographic overview presented indicates the level of research conducted on the flow around rod bundles. Nevertheless, a number of points have yet to be explored, despite their significant interest in the field of IV-gen nuclear reactor applications. It is within this framework that the objective of this work is delineated. The present study will analyse liquid metals employed as coolants around rod bundles under not only forced but also mixed convection conditions. Such conditions may arise in the event of malfunction in the facilities, and thus represent a subject of particular interest for safety design. Moreover, the Reynolds numbers of the flow in normal operating conditions fall into the transitional regimes, which are often undocumented and very difficult to reproduce accurately through experiments. The generation of high fidelity data will be accomplished through DNS simulations, ensuring its relevance for the prospective development or validation of turbulence models.

CHAPTER 3

Numerical methods

The application of Direct Numerical Simulations is often restricted to flows in very simple geometries, such as parallel channels, pipes, or flat plates. This limitation mainly arises from the constraints of some of the most widely used discretization techniques, particularly spectral methods, as well as from the numerical errors that frequently affect the resolution of the discrete equations on unstructured grids. Consequently, the development of accurate and efficient methods for DNS in complex geometries remains an important and active area of research in turbulent flow and heat transfer.

In this context, approaches based on representing arbitrary geometries within Cartesian grids using Finite Difference or Finite Volume Methods are promising candidates, thanks to their simple mesh generation procedures and straightforward Cartesian parallelisation. These approaches are commonly referred to as Immersed Boundary Methods. The original formulation of the Immersed Boundary Method was firstly introduced by Peskin [113]: a wide range of methodologies has been proposed to simulate flows over bodies that do not conform to the computational grid. These include the immersed interface method [114], the Cartesian grid method [115], and the cut-cell method [116]. Many of these variants are reviewed and briefly described by Mittal and Iaccarino [117]. However, a common drawback of several Immersed Boundary Method approaches lies in the accurate enforcement of bound-

ary conditions near irregular surfaces, where increased local truncation errors may compromise the global spatial accuracy.
The approach used in this work is the one introduced by Angeli and Stalio [3]. This innovative representation of arbitrarily irregular cylindrical boundaries on Cartesian grids constitutes an extension of the method originally developed by Barozzi *et al.* [118]. The original technique, presented in [3] and briefly described in the following Sections, consists in a linear mapping between the variables defined on stencils and on the main grid. This allows the numerical advantages of the Cartesian approach to be preserved while retaining second-order accuracy.

3.1. Mathematical formulation

The methodology implements a discrete form of the incompressible Navier-Stokes and energy equations for hydro-dynamically and thermally fully-developed flows. All the fluid properties are assumed constant, the rate of heating due to viscous dissipation is neglected. In this work, fully developed flow along x_3-direction is specifically considered for the formulation of governing equations, but the method presented here does not set specific requirements for boundary conditions in directions orthogonal to the mean flow.

3.1.1. Continuity equation

Under the above hypotheses, the continuity equation reads:

$$\frac{\partial u_i}{\partial x_i} = 0 \tag{3.1}$$

where u_i indicates the i-th component of the velocity field and the repeated index notation is implied.

3.1.2. Momentum and energy equations

A formulation of momentum equations excluding momentum sources is

$$\rho^o \left(\frac{\partial u_i}{\partial t} + u_j \frac{\partial u_i}{\partial x_j} \right) = -\frac{\partial p}{\partial x_i} + \mu \frac{\partial^2 u_i}{\partial x_j \partial x_j} \tag{3.2}$$

temperature is solved for in the energy equation

$$\rho^o c_p \left[\frac{\partial T}{\partial t} + u_i \frac{\partial T}{\partial x_i} \right] = \lambda \frac{\partial^2 T}{\partial x_i \partial x_i} + \sigma \tag{3.3}$$

where σ represents a generic source term, expressed in $\mathrm{W/m^3}$.

For statistically steady flows, thermally and hydro dynamically fully developed in the z direction, governing equations (3.1)-(3.3) can be arranged to allow for the representation of all variables, including temperature and pressure through streamwise periodic quantities, see for example [119] where also buoyancy effects are considered. This is in view of the computational efficiency of the numerical code.

For the statistically steady case under scrutiny which is fully developed along direction x_3, a time and superficial average is defined for the generic scalar field f and indicated by angular brackets

$$\langle f \rangle(x_3) \equiv \frac{1}{\Omega\,(t_b - t_a)} \int_{t_a}^{t_b} \int_{\Omega} f(\boldsymbol{x}, t)\, \mathrm{d}\Omega\, \mathrm{d}t \tag{3.4}$$

where Ω is the surface of a cross-flow plane (perpendicular to x_3, the direction of full development) while $[t_a, t_b]$ is a sufficiently large time interval for $\langle f \rangle$ to be independent of time. By averaging equation (3.2) for $i = 3$ and taking the x derivative of the result it is found that the time average of the pressure field must be linear in x_3:

$$\frac{d\langle p \rangle}{dx_3} = \gamma \tag{3.5}$$

for some constant quantity γ which is negative for flows in the positive x_3 direction. A linear function $\widetilde{p}(x_3)$ can be defined with respect to a fixed point x_3^0 along the x_3-axis:

$$\widetilde{p}(x_3) = \langle p \rangle(x_3^0) + \gamma \left(x_3 - x_3^0 \right) \tag{3.6}$$

which allows to split the pressure into a linear part $\widetilde{p}$, and a fluctuation p':

$$p(\boldsymbol{x}, t) = \widetilde{p}(x_3) + p'(\boldsymbol{x}, t) \tag{3.7}$$

where $\langle p' \rangle(x_3) = 0$.

The form of the momentum equations to be solved is then

$$\rho^o\left(\frac{\partial u_i}{\partial t}+u_j\frac{\partial u_i}{\partial x_j}\right)=-\frac{\partial p'}{\partial x_i}+\mu\frac{\partial^2 u_i}{\partial x_j\partial x_j}-\gamma\delta_{i3} \tag{3.8}$$

In the form of equation (3.8), periodic boundary conditions may be enforced along the streamwise direction on all variables, including the fluctuating pressure p'.

The momentum equation writes in terms of dimensionless quantities as

$$\frac{\partial u_i^*}{\partial t^*}+u_j^*\frac{\partial u_i^*}{\partial x_j^*}=-\frac{\partial p'^*}{\partial x_i^*}+\frac{1}{\mathrm{Re}_\tau}\frac{\partial^2 u_i^*}{\partial x_j^*\partial x_j^*}+\frac{\omega^*}{\Omega^*}\delta_{i3} \tag{3.9}$$

where the last term equals the wet perimeter divided by the cross sectional area and it represents the ensemble average of the pressure drop along the streamwise direction. In equation (3.9), the friction Reynolds number Re_τ is defined as:

$$\mathrm{Re}_\tau=\frac{u_\tau L_{\mathrm{ref}}}{\nu} \tag{3.10}$$

where the velocity scale is $u_{\mathrm{ref}}=u_\tau=\sqrt{\tau_w/\rho^o}$.

3.1.3. Normalized form of the energy equation

Thermal boundary conditions selected for the present discussion is of imposed heat flux. Alternatively, temperature can be specified at the walls solving a slightly different set of equations, see the method in [120]. As in the hypothesis of assigned heat flux, the fully developed time-averaged temperature profile in axial direction is linear, the temperature slope in z may be evaluated from an energy balance

$$a=\frac{q''\omega}{\dot{m}c_p} \tag{3.11}$$

In equation (3.11), q'' indicates the imposed wall heat flux over perimeter ω of surface Ω; the sign convention associates a positive heat flux $q''>0$ to the heating of the fluid. The mass flow rate $\dot{m}$ is defined in the standard way

$$\dot{m}\equiv\int_\Omega \rho^o u_3\,\mathrm{d}\Omega \tag{3.12}$$

the cross flow area Ω as well as its perimeter ω are supposed independent of the streamwise coordinate x_3, this is also required by the current implementation of the method presented.

Given the linear behavior of temperature along x_3, periodicity is enforced on the fluid excess temperature θ, defined as

$$\theta(\boldsymbol{x},t) \equiv [T(\boldsymbol{x},t) - \langle T \rangle (x_3)] \tag{3.13}$$

where $\langle \theta \rangle$ is independent of the streamwise coordinate x_3. From equations (3.13) and (3.11)

$$\frac{\partial T}{\partial x_3} = a + \frac{\partial \theta}{\partial x_3}; \qquad \frac{\partial^2 T}{\partial x_3^2} = \frac{\partial^2 \theta}{\partial x_3^2} \tag{3.14}$$

the energy equation (3.3) becomes

$$\rho^o c_p \left[\frac{\partial \theta}{\partial t} + u_i \frac{\partial \theta}{\partial x_i} \right] = \lambda \frac{\partial^2 \theta}{\partial x_i \partial x_i} - \rho^o c_p a u_3 \tag{3.15}$$

where the generic source term σ in equation (3.3) is set to zero while term $\rho^o c_p a u_3$ at the right-hand side of equation (3.15) follows from the normalization of temperature [121]. It represents thermal advection along the streamwise direction x_3 due to averaged temperature variation along x_3. The first component of the local velocity vector u_3 depends upon position and time. Using the same reference quantities as for the momentum equation and

$$T_{\text{ref}} = \frac{q''\, L_{\text{ref}}}{\lambda} \tag{3.16}$$

for temperature, the energy equation writes in its dimensionless form

$$\frac{\partial \theta^*}{\partial t^*} + u_i^* \frac{\partial \theta^*}{\partial x_i^*} = \frac{1}{\text{Re}_\tau \text{Pr}} \frac{\partial^2 \theta^*}{\partial x_i^* \partial x_i^*} - \frac{1}{\text{Re}_\tau \text{Pr}} \frac{\omega^*}{\Omega^*} \frac{u_3^*}{u_m^*} \tag{3.17}$$

And the following is the system of differential equations

$$\frac{\partial u_i^*}{\partial x_i^*} = 0 \tag{3.18}$$

$$\frac{\partial u_i^*}{\partial t^*} + u_j^* \frac{\partial u_i^*}{\partial x_j^*} = -\frac{\partial p'^*}{\partial x_i^*} + \frac{1}{\mathrm{Re}_\tau} \frac{\partial^2 u_i^*}{\partial x_j^* \partial x_j^*} + \frac{\omega^*}{\Omega^*} \delta_{i3} \tag{3.19}$$

$$\frac{\partial \theta^*}{\partial t^*} + u_i^* \frac{\partial \theta^*}{\partial x_i^*} = \frac{1}{\mathrm{Re}_\tau \mathrm{Pr}} \frac{\partial^2 \theta^*}{\partial x_i^* \partial x_i^*} - \frac{1}{\mathrm{Re}_\tau \mathrm{Pr}} \frac{\omega^*}{\Omega^*} \frac{u_3^*}{u_m^*} \tag{3.20}$$

which, complemented with an appropriate set of boundary conditions, is numerically solved in this paper for the Direct Numerical Simulation of fully-developed turbulent flow and heat transfer in direction x_3. Asterisks in (3.18)-(3.20) are dropped in the following text to ease notation. A model differential equation of the form:

$$\frac{\partial \varphi}{\partial t} + u_i \frac{\partial \varphi}{\partial x_i} = \Gamma \frac{\partial^2 \varphi}{\partial x_i \partial x_i} + q \tag{3.21}$$

where q is a general source term and might depend upon position and time, is used in the discussion for the presentation of the numerical method.

3.2. Algorithm implementation

The representation of arbitrarily irregular cylindrical boundaries on Cartesian grids is an extension of the method developed by Barozzi *et al.* [118]. Therefore, the three-dimensional code for the Immersed Boundary Method used to perform the simulations presented in this work is obtained by the extension to the third, homogeneous direction of the two-dimensional theory reported here. A Cartesian grid of points named $\mathscr{G}$ is distributed on a rectangle that contains the physical domain. The spacing of the grid is in general non-uniform. From the superimposition of the orthogonal grid-lines derived from $\mathscr{G}$ and a generically shaped physical domain a set of points $\mathscr{B}$ is obtained. Two types of stencil and Control Volume are defined, these are represented in Figures 3.1a and 3.1b. Stencils of type g are based on grid $\mathscr{G}$ and are not influenced by the shape of the domain while stencils of type b adapt to the domain geometry. When a stencil b is nearby the domain boundary, the points of

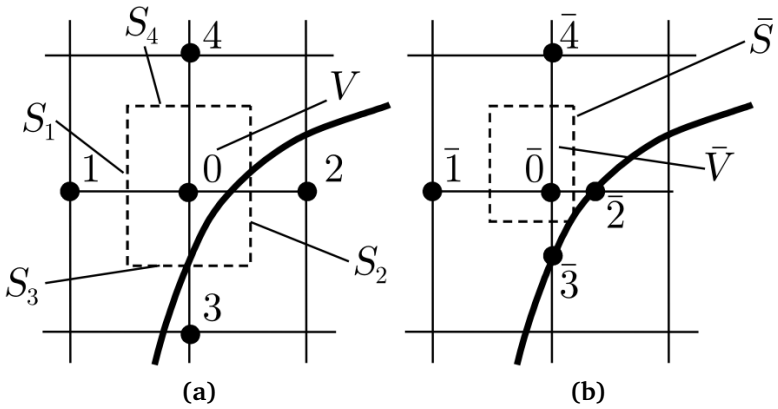

Figure 3.1: Local stencils (a) g and (b) d. [3]

intersection are included. Control Volumes built on g and b stencils are respectively indicated by Ω and $\bar{\Omega}$. Away from the boundaries, the stencils b and g, as well as the Control Volumes Ω and $\bar{\Omega}$, are identical. The Control Volumes always retain a rectangular geometry, and the metrics of cells located near the boundary are suitably rescaled according to the position of the cell center relative to the boundary (see Figures 3.2a and 3.2b). As a result, the union of all $\bar{\Omega}$ Control Volumes does not fully cover the entire domain, as illustrated in Figure 3.1b. Since the g stencils do not contain information about the location of the domain boundary, they cannot directly be used to impose the correct boundary conditions. The proposed methodology introduces a linear mapping between g and b stencils, allowing the discrete equations on the Control Volumes $\bar{\Omega}$ to be expressed in terms of quantities defined on the grid $\mathscr{G}$ and on the g stencils. This method preserves the computational benefits of Cartesian grids while ensuring that boundary conditions are properly enforced, even in presence of irregular boundaries.

The algebraic set of transport equations for a generic scalar function, fully reported in [3], is second-order accurate. In particular, a Crank–Nicolson scheme is used for time integration, combined with a second-order Adams–Bashforth method for the diffusive and advective terms. As previously mentioned, to retain a structured-grid framework even in domains with irregular boundaries, a linear mapping is introduced that expresses the unknowns associated with b stencils in terms of quanti-

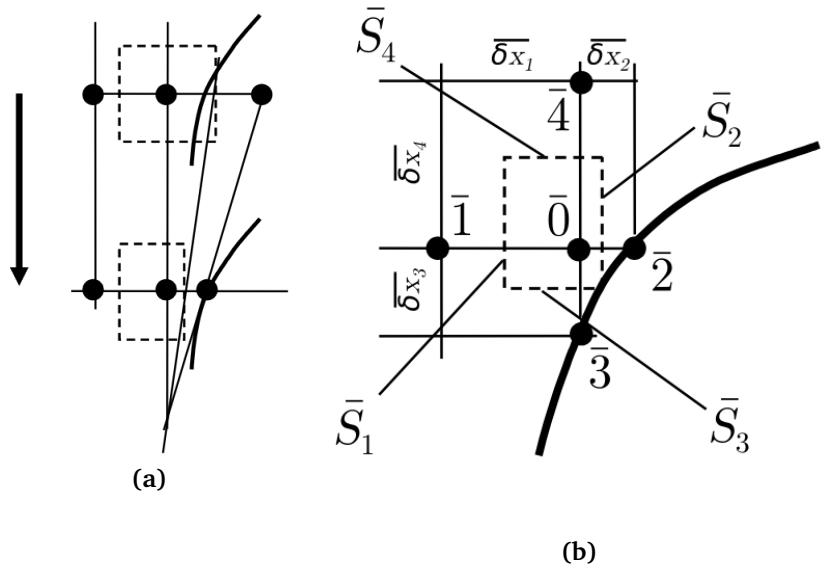

Figure 3.2: Resizing (a) and geometry of the discretization Control Volume (b). [3]

ties defined on g stencils, plus a non-homogeneous term that takes into account the boundary conditions. Because the method relies on pointwise values at the boundary, rather than fluxes or volume averages, the Finite Volume formulation used in the interior of the domain is coupled with a Finite Difference treatment near the boundary. This hybrid strategy preserves spatial accuracy. The use of finite differences in the vicinity of the boundary enables accurate enforcement of boundary conditions even when the boundary is not aligned with the Cartesian grid lines. Combined with the Finite Volume method in the interior, the approach maintains second-order accuracy throughout the entire domain for both uniform and non-uniform meshes.
The numerical method employed is based on staggered grids. Although staggered meshes introduce additional complexity, requiring complex implementation, they also offer substantial advantages. Using separate grids for the energy equation and for each momentum component enables direct evaluation of momentum and energy fluxes across Control Volume faces. Moreover, it prevents the "checker-boarding" phenomenon [122] by ensuring a more stable and physically consistent distribution of variables. As for the pressure-velocity decoupling a Projection Method [123]-[124] is implemented.

The validation of the code is conducted by means of three different test cases. Firstly, the formal accuracy of the method is demonstrated against the analytical solution of a laminar pipe flow. The accuracy at the boundary is further assessed by comparing laminar results of a triangular array of heated rods against the results of previous studies. In conclusion, a Direct Numerical Simulation is conducted for the case of turbulent pipe flow at $\mathrm{Re}_\tau = 180$, thereby confirming the favourable qualities of the present method and its adequacy for turbulent, fully-developed flow simulation in non-rectangular domains.
Furthermore, the findings of the performance tests demonstrate that the computational cost for degree of freedom associated with the proposed procedure is minimal, particularly when compared with a conventional unstructured finite volume solver. Overall the technique developed by Angeli and Stalio [3] proves to be a satisfactory compromise between computational efficiency and accuracy.

CHAPTER 4

Buoyancy effects around a square bundle

The results of DNSs of fully developed flow in a bundle of vertical heated rods in a square arrangement are hereafter presented. The fluid is assumed to be Liquid Lead-Bismuth Eutectic (LBE) by imposing a Prandtl number of 0.031. A total of four cases are examined, one characterised by forced convection (Ra = 0) and three by mixed convection (Ra = 2.5×10^3,2.5×10^4,5.0×10^4).

4.1. Case study

The computational domain consists of a flow around 4 cylindrical rods arranged in a square lattice, as shown in Figure 4.1a. The cylindrical rods have a diameter denoted as D, while the centers are spaced by a pitch P (see Figure 4.1b), with P/D = 1.25: this value is typically found in nuclear reactor core designs, particularly in pressurized water reactors and sometimes boiling water reactors. The domain under consideration might be considered as a cell within a larger set of rods in a bundle and periodic conditions are imposed in the cross-flow directions. The analysis is

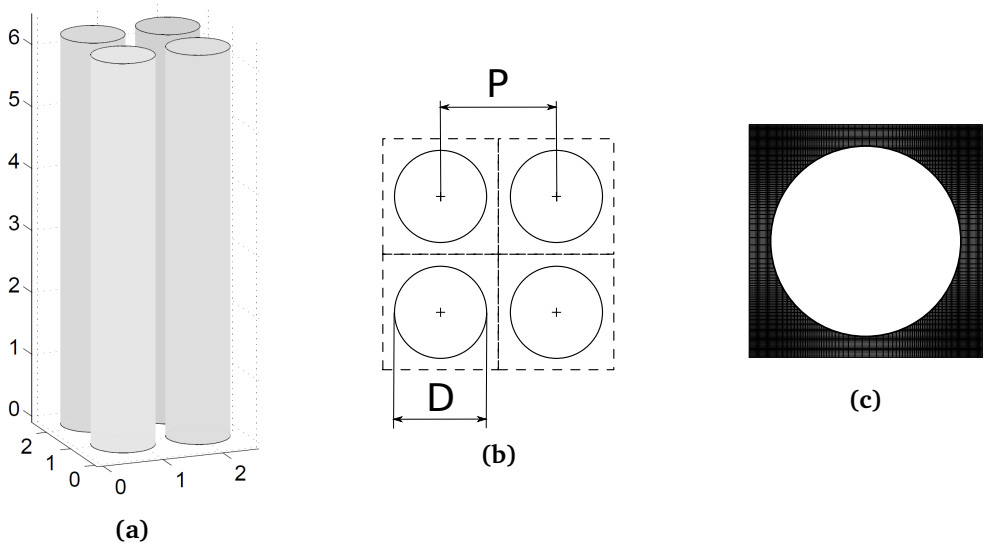

(a) (b) (c)

Figure 4.1: (a) 3D view of the computational domain. (b) Cross-sectional sketch. (c) One-quarter of the 512^2 mesh in the $x-y$ plane.

confined to a periodic segment of length $L_z = 2\pi D_h$, where

$$D_h = D\left[\frac{4}{\pi}\left(\frac{P}{D}\right)^2 - 1\right] \tag{4.1}$$

is the hydraulic diameter of a sub-channel. For the specific case under analysis, $D_h \approx 0.989D$. Each bar is treated as uniformly heated by a constant heat flux q'' and the flow is considered fully developed. Periodic conditions enforced on both the velocity field and the modified pressure field p_m well delineate the physical scenario of a bundle of heated rods under the assumption of fully developed flow. Furthermore, the temperature field needs to be normalized so that periodic boundary conditions can be also set on a modified temperature-like variable θ [125].

The computational grid has constant spacing in the streamwise direction z while it is not uniform in the crossflow direction $x-y$. The conformity of the computational grid spacing to DNS standards is verified by a posteriori evaluation of the minimum Kolmogorov scale η_{min}, where

$$\eta = \left(\frac{\nu^3}{\varepsilon}\right)^{\frac{1}{4}} \tag{4.2}$$

Table 4.1 provides a comprehensive overview of the domain dimensions, computational grid, and its resolution.

In Table 4.2 the dimensionless parameters imposed in the simulations (the friction Reynolds number Re_τ as defined in Eq. 3.10, the Rayleigh number Ra = Gr Pr and and the Prandtl number Pr) are listed alongside some values resulting from the DNSs, such as the bulk Reynolds number Re_b, the Richardson number $Ri = Gr/Re_b$, the Nusselt number Nu and the bulk Peclet number $Pe = Re_b$ Pr. In order to assess the effect of buoyancy on the mean flow, turbulent quantities and heat transfer, four different simulations have been implemented: one purely forced convection case (Ri = 0) and three mixed convection cases (Ri = 0.025, Ri = 0.24 and Ri = 0.75). The Reynolds friction number Re_τ has been set at 180, which is a relatively low value in relation to typical operational parameters. The selected Prandtl number value of 0.031 is associated with LBE at the reference temperature T_0 = 220°C, according to [11].
The Reynolds numbers obtained, with the highest being approximately 1850 for Ri = 0.24 and 1465 for Ri = 0.75, demonstrate that these case studies fall within a transition zone between laminar flow and fully turbulent flow. This provides data for flow regimes that are poorly documented in the literature, especially for mixed convection cases.

In the following, analyses of the first-order statistics of dynamic and thermal fields are shown. Moreover, a focus on the turbulent kinetic energy and turbulent heat flux budgets is presented. The DNS data are presented in two formats: as con-

Table 4.1: Grid

Quantity	-	$(\cdot)_x$	$(\cdot)_y$	$(\cdot)_z$
Domain size	$L_{(\cdot)}/D_h$	2.5	2.5	2π
no. of cells	$n_{(\cdot)}$	512	512	256
spacing	$\Delta(\cdot)^+$	2.6	2.6	4.4
resolution	$\Delta(\cdot)/\eta_{min}$	1.1	1.1	2.3

Table 4.2: Flow and thermal parameters for the DNSs performed and relevant integral values calculated.

Quantity		**Forced**	**Mixed**	**Mixed**	**Mixed**
Friction Reynolds number	Re_τ	180	180	180	180
Rayleigh number	Ra	0	2.5×10^3	2.5×10^4	5.0×10^4
Prandtl number	Pr	0.031	0.031	0.031	0.031
Bulk Reynolds number	Re_b	1785	1780	1850	1465
Nusselt number	Nu	7.60	7.63	7.50	9.30
Richardson number	Ri	0	0.025	0.24	0.75
Bulk Peclet number	Pe_b	55	55	57	45

tours and as profile lines along the paths identified in Figure 4.3a. The profile shape has been selected in order to facilitate the analysis of the fluid's behaviour in different areas of the domain, in accordance with approaches previously employed in the literature for similar geometries [107].

The statistics are performed by applying the Reynolds decomposition: the quantities are averaged both over time, once the flow reaches statistically steady conditions, and along the streamwise direction z. The following convention is therefore used in the following chapters:

$$\phi = \overline{\phi} - \phi_i' \tag{4.3}$$

where ϕ is the instantaneous quantity, $\overline{\phi}$ is the averaged value and ϕ_i' stands for the fluctuation term.
The quantities are presented subsequently in a dimensionless form: the velocity and temperature scales employed for this purpose are u_τ and ΔT_{ref}, as previously defined in Section 3.

4.2. Velocity field statistics

Contours of the time-averaged streamwise velocity component $\overline{u_z}$ are reported in Figure 4.2. Starting from the forced convection case (Ri = 0) in Figure 4.2a some features of the flow can be pointed out: the value of $\overline{u_z}$ reaches the maximum at the center of the channel and it decreases going down to the subchannels. The effect of aiding buoyancy can be observed both in Figures 4.2c and 4.2d: for Ri = 0.24 there is a slightly increase of the value of the streamwise velocity, clearly visible from the green profiles of Figure 4.3b in the region previously identified as path II. The enhanced velocity observed in specific regions of the domain is aligned with the corresponding rise in the bulk Reynolds number, which increased from 1785 to 1850. In examining the mixed case with Ri = 0.75, from Figure 4.2d a remarkable change

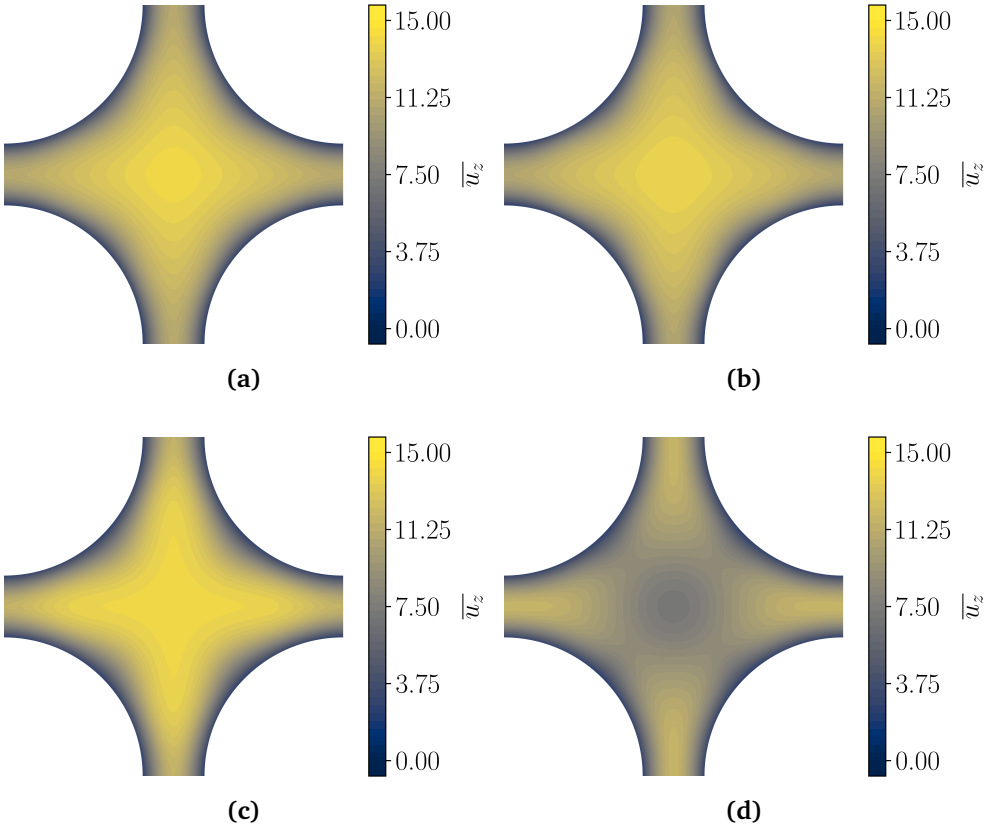

Figure 4.2: Time-averaged streamwise velocity $\overline{u_z}$ contours for: (a) Ri = 0, (b) Ri = 0.025, (c) Ri = 0.24, (d) Ri = 0.75.

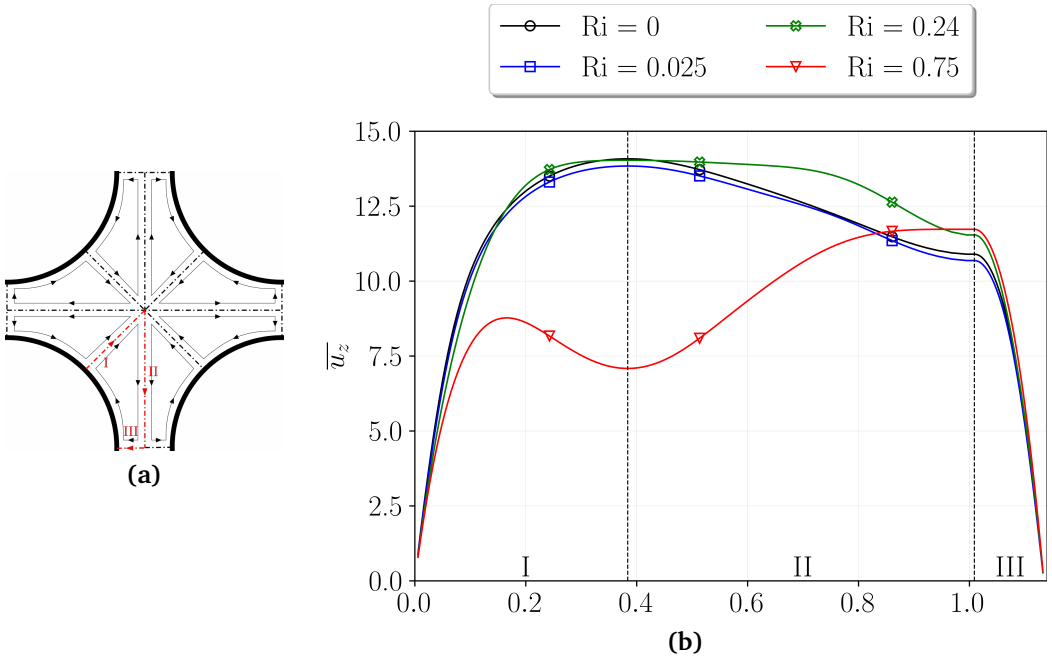

(a) (b)

Figure 4.3: Profiles of $\overline{u_z}$ for: ∘ Ri = 0, □ Ri = 0.025, × Ri = 0.24, ▽ Ri = 0.75.

in the flow behaviour is evident: $\overline{u_z}$ peaks at the center of the subchannels, while all over the domain it is lower with respect to the forced convection case and also the mixed case with Ri = 0.24. Again the average velocity trend ties in with the values of the Reynolds bulk number of Table 4.2, that decreases to a value of 1465 for Ri = 0.75. Moreover, what has been observed is also evident from the profiles in Figure 4.3b, where for the case Ri = 0.75 the maximum value of $\overline{u_z}$ is reached in path III and there is a radical change in the shape of the velocity profile, which undergoes several changes in its derivative over the center of the channel, the region between path I and path II.

A peculiar feature of the flow around rod bundles is the appearence of secondary flow components. Thus, the time-averaged cross-flow velocity field $\overline{u_\perp} = \sqrt{\overline{u_x}^2 + \overline{u_y}^2}$ contours are shown in Figure 4.4 alongside streamlines of the cross-flow components on the unit flow cells as identified in Figure 4.3a. It is evident how buoyancy affects the cross-flow velocities: the contours show a reduction in the magnitude of $\overline{u_\perp}$ with the aiding buoyancy. Furthermore, the streamlines of the cross-flow components

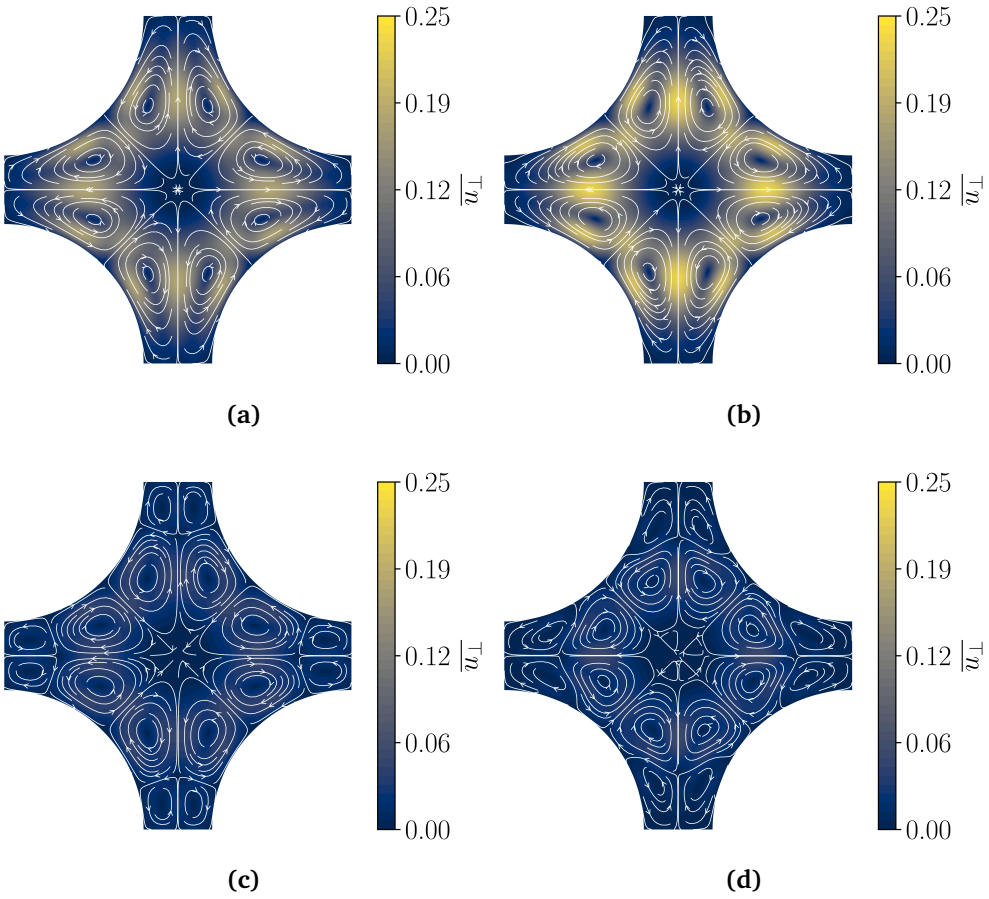

Figure 4.4: Time-averaged crossflow velocity $\overline{u_\perp}$ contours for: (a) Ri = 0, (b) Ri = 0.025, (c) Ri = 0.24, (d) Ri = 0.75.

can be considered: comparing the three cases reveals that the recirculation undergoes changes when buoyancy is introduced. Focusing on the narrowest gap of the domain, the region between two adiacent bundles, the forced case exhibits a recirculation driven from the centre of the gap towards the bundle. In contrast, both cases with aided buoyancy exhibit the exact opposite phenomenon, the recirculation in the narrowest gap is driven from the bundle to the centre of the gap.

In Figure 4.5 contours of time-averaged turbulent kinetic energy defined as:

$$k = \frac{1}{2}\left(\overline{u'_x u'_x} + \overline{u'_y u'_y} + \overline{u'_z u'_z}\right) \tag{4.4}$$

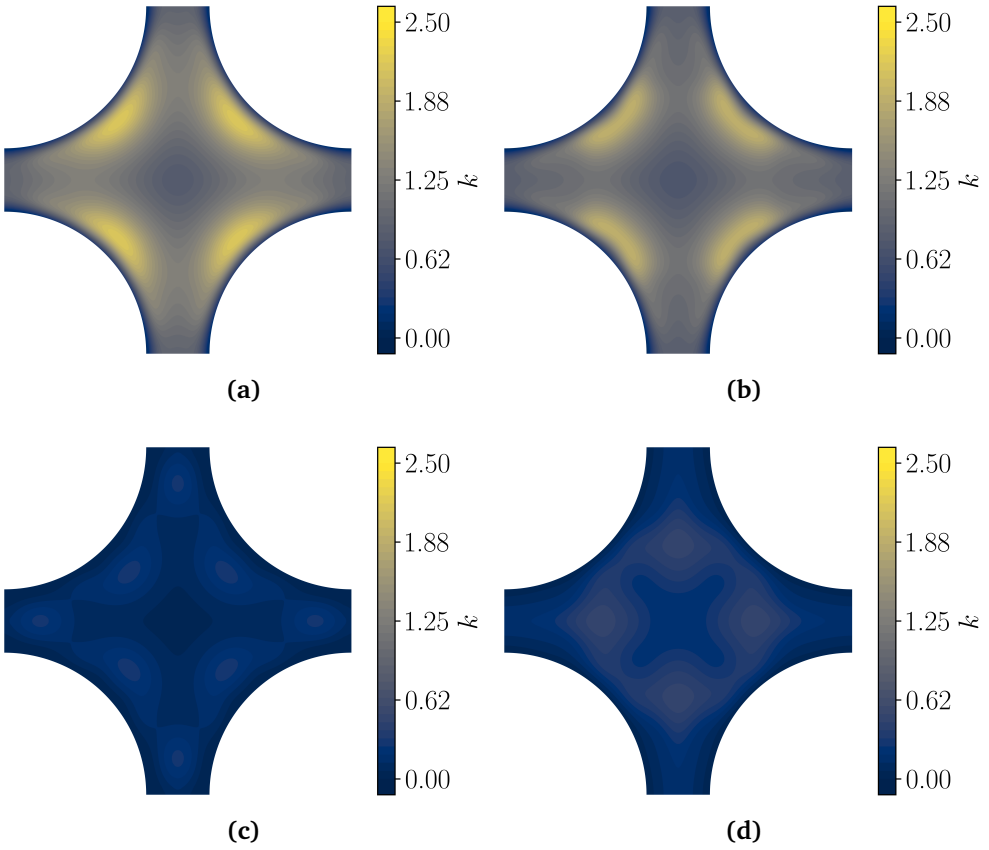

Figure 4.5: Time-averaged turbulent kinetic energy k contours for: (a) Ri = 0, (b) Ri = 0.025, (c) Ri = 0.24, (d) Ri = 0.75.

are reported. As already observed for the Reynolds stresses, a general decrease in the turbulent kinetic energy level is obtained for both the mixed convection cases. For Ri = 0 the maximum is achieved near the bundles: this feature is more evident in Figure 4.6 where the profile peaks at the beginning of path I. The observed behaviour differs when buoyancy is introduced and it is clear once again from the profiles (Figure 4.6): for Ri = 0.24 the overall value of k is approximately one order of magnitude lower in comparison to the forced convection case. For Ri = 0.75 the fluid behaviour is somewhat different: the region exhibiting the highest concentration of turbulent kinetic energy is no longer situated in close proximity to the rod bundle but it is located in the center of path II, a region between the center of the channel and its narrowest gap. The results for the forced case of the present

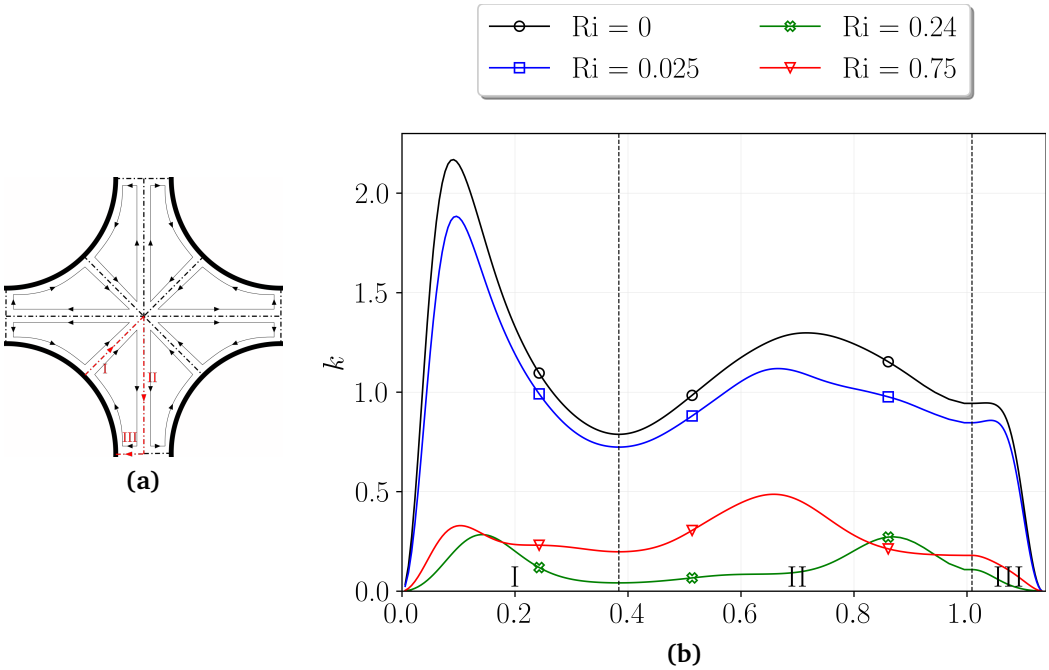

Figure 4.6: Profiles of k for: ∘ Ri = 0, □ Ri = 0.025, × Ri = 0.24, ▽ Ri = 0.75.

study well align with the ones obtained by [107] for rods in square arrangement: although the forced case here reported has a much lower Reynolds number, the turbulent kinetic energy trend is the same, with an initial peak in fluctuations near the rod bundle before they begin to decay toward farwall regions of the geometry.

For the sake of completeness, profiles for $u'_{z,rms}$ and $u'_{x,rms}$, calculated as:

$$u'_{i,rms} = \sqrt{\overline{u'_i u'_i}} \tag{4.5}$$

are presented in Figure 4.7. Of particular interest is the trend of the profiles for the Ri = 0.75 case: for $u'_{z,rms}$, there is not only a peak in proximity to the bundles in path I but also in path II (coinciding with the turbulent kinetic energy peak for the same case). Additionally, it is evident that the $u'_{x,rms}$ component maintains an approximately constant value throughout the domain for cases with higher buoyancy. Conversely, in the forced case, its value diminishes within the smaller gap.

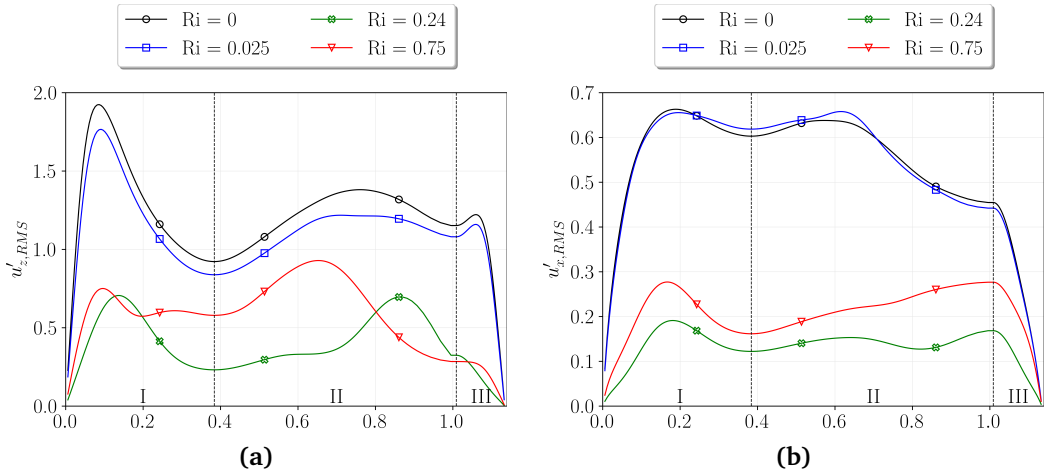

Figure 4.7: Profiles of time-averaged for (a) u'_{zrms} and (b) u'_{xrms}: ∘ Ri = 0, □ Ri = 0.025, × Ri = 0.24, ▽ Ri = 0.75.

Figures 4.8-4.9 report contours of average Reynolds stresses $-\overline{u'_r u'_z}$ and $\overline{u'_\varphi u'_z}$, where u'_r and u'_φ are the projections of the velocity fluctuation vector along the radial and azimuthal directions with respect to the center of each rod. Since the definition of the coordinate system (r, φ) is not unique in a subchannel, color maps of the aforementioned quantities in Figures 4.8-4.9 are limited to one fourth of the subchannel. A near-wall peak region in the distributions of $-\overline{u'_r u'_z}$ can be observed for all the three cases Figure 4.8, however for both the mixed convection cases Ri = 0.24 and Ri = 0.75 the overall value of the Reynolds stress inside the domain more uniform but lower with respect to the forced convection case, thus influencing the peak value which is decreased by ≈ 86% for Ri = 0.75. Th distributions of $\overline{u'_\varphi u'_z}$ in Figure 4.9 exhibit two local extrema (a maximum and a minimum) in each unit flow cell, one close to the wall and another between the center of the subchannel and the narrowest gap (path II), whose sign alternates proceeding along the azimuthal direction. These findings are in accordance to previous results obtained by Angeli *et al.* [112] for rod bundle arranged in triangular shape and with higher Reynolds number. The intensity and location of these extrema change significantly for Ri = 0.24, with the central extremum decreasing in intensity, while the region of the near-wall extremum becomes larger. For Ri = 0.75 $\overline{u'_\varphi u'_z}$ undergoes another change as the two local extremes change sign compared to the cases with Ri = 0 and Ri = 0.24,

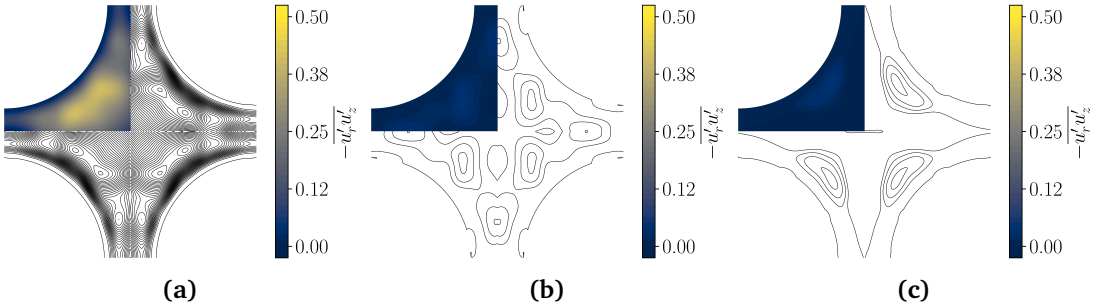

Figure 4.8: Time-averaged Reynolds stresses $-\overline{u_r' u_z'}$ contours for: (a) Ri = 0, (b) Ri = 0.24, (c) Ri = 0.75.

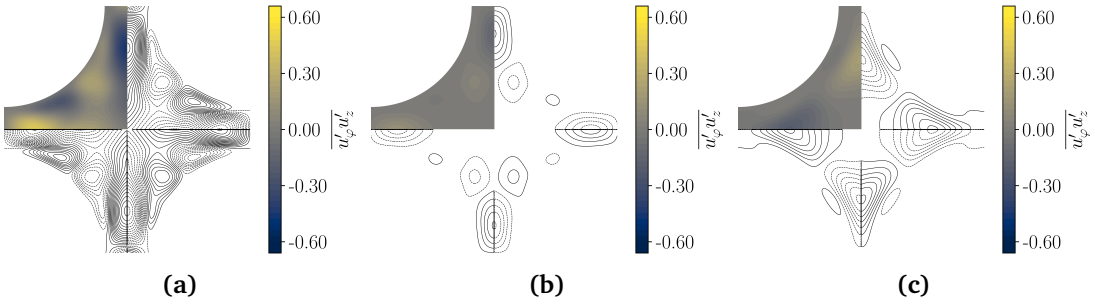

Figure 4.9: Time-averaged Reynolds stresses $\overline{u_\varphi' u_z'}$ contours for: (a) Ri = 0, (b) Ri = 0.24, (c) Ri = 0.75.

and the regions near the wall are flattened more towards the rod bundles. The most interesting aspect of this case is, in agreement with the results for k, the increase in intensity compared to the case Ri = 0.24.

In order to assess the reliability of turbulence models, it is worth considering also the dissipation of turbulent kinetic energy ε as a key indicator. In Figure 4.10 the contours of ε, calculated as

$$\varepsilon = \frac{1}{Re_\tau} \overline{\frac{\partial u_i'}{\partial x_j} \frac{\partial u_i'}{\partial x_j}}. \tag{4.6}$$

are reported. The dissipation ε is reported with a negative sign because it is considered as the dissipative term of the turbulent kinetic energy transport equation that will be analysed in detail in Section 4.4. As expected the greater value of dissipa-

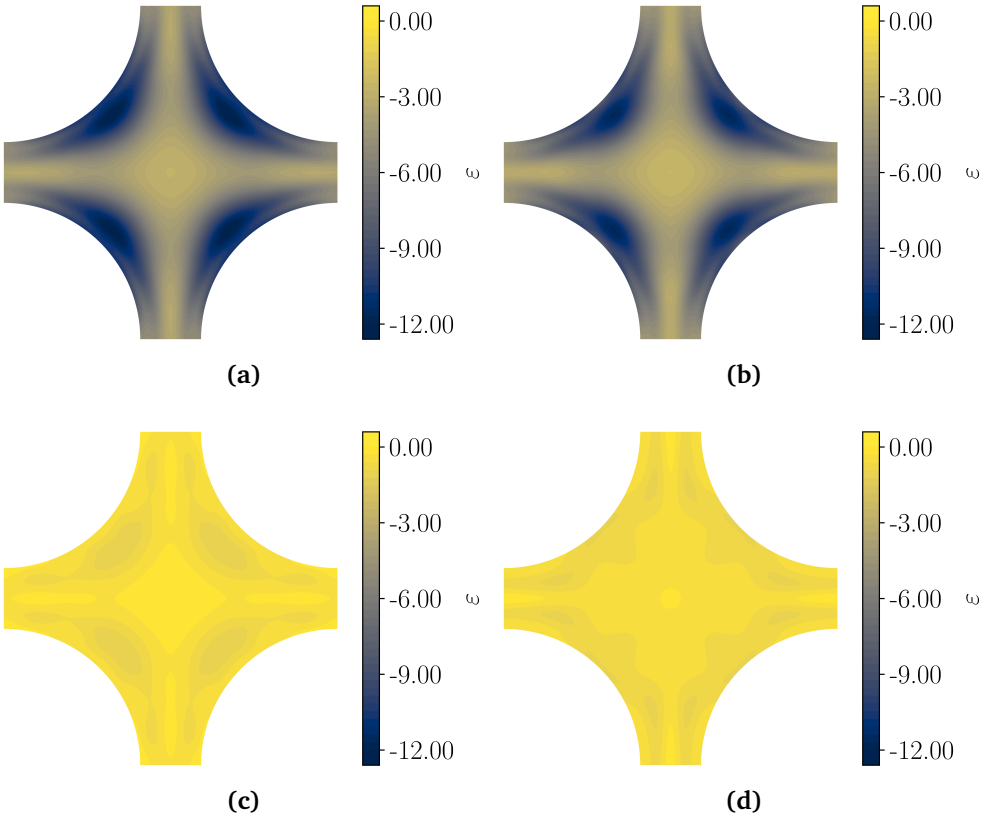

Figure 4.10: Time-averaged turbulent kinetic energy dissipation ε contours for: (a) Ri = 0, (b) Ri = 0.025, (c) Ri = 0.24, (d) Ri = 0.75.

tion is distinctive of the forced case (Figure 4.10a) since it is the one showing the highest contribution for the turbulent kinetic energy. As the buoyancy increases, the dissipation levels decrease considerably, reaching a peak value that is an order of magnitude lower with respect to the forced convection case. It should be noted that, despite a slight increase in turbulent kinetic energy observed for the Ri = 0.75 case, this is not reflected in the dissipation trend, as is also evident from the profiles in the Figure 4.11. This behaviour may be attributed to additional contributions that enhance the dissipation of turbulent kinetic energy. Section 4.4 will be designated to the examination in detail of the turbulent kinetic energy budget.

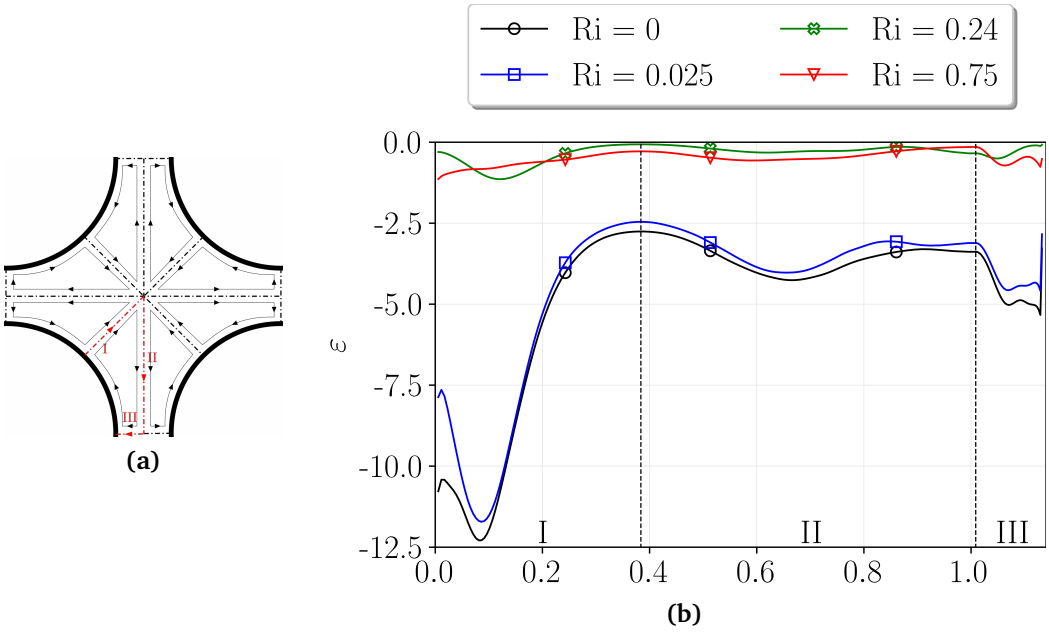

(a) (b)

Figure 4.11: Profiles of ε for: $\circ$ Ri $= 0$, $\square$ Ri $= 0.025$, $\times$ Ri $= 0.24$, $\triangledown$ Ri $= 0.75$.

4.3. Thermal field statistics

It is of significant importance to report some thermal field properties as temperature, temperature variance, turbulent heat fluxes and dissipation of temperature variance. Numerous turbulence models enhance the complexity of the thermal dynamics by incorporating separate transport equations for some thermal field variables. For instance, these models typically employ at least one transport equation for the temperature variance, and in the case of fluids with Prandtl numbers that differ from unity, they also utilise a transport equation for temperature variance dissipation ε_θ [2].

In order to make the results comparable between forced and mixed cases, in

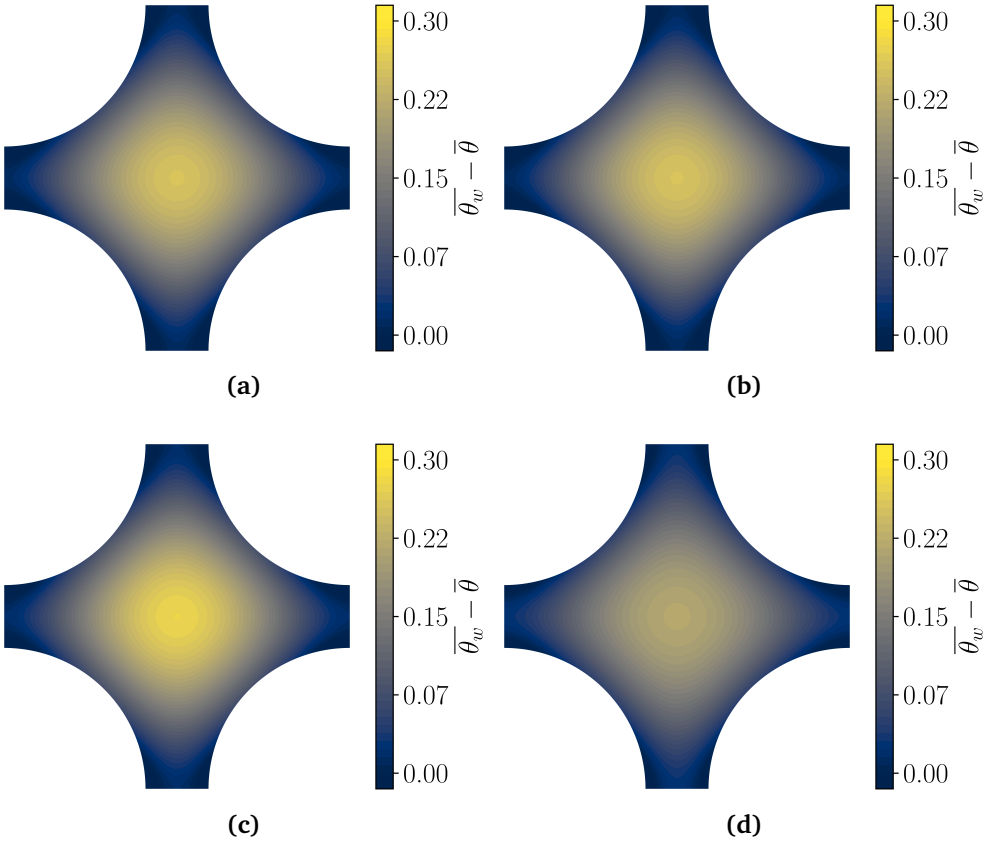

Figure 4.12: Time-averaged temperature $\overline{\theta_w} - \overline{\theta}$ contours for: (a) Ri = 0, (b) Ri = 0.025, (c) Ri = 0.24, (d) Ri = 0.75.

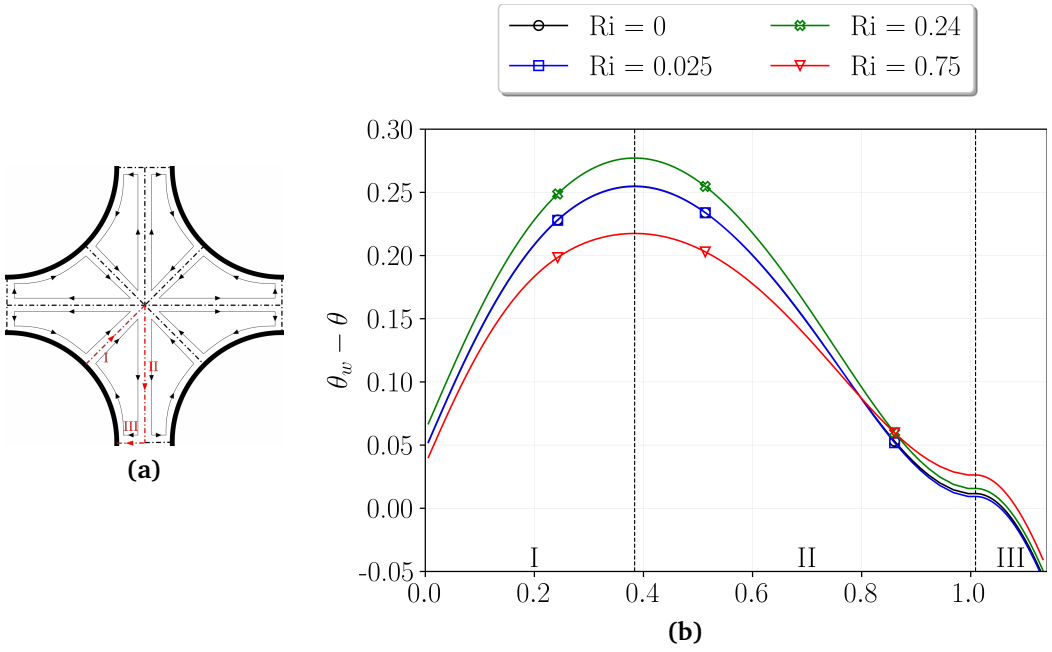

Figure 4.13: Profiles of $\overline{\theta_w} - \overline{\theta}$ for: ∘ Ri = 0, □ Ri = 0.025, × Ri = 0.24, ▽ Ri = 0.75.

Figure 4.12 are reported the temperature fields $\overline{\theta_w} - \overline{\theta}$, where $\overline{\theta_w}$ is the average wall temperature and θ is the excess temperature as previously stated. As expected for low Prandlt numbers, there is no similarity between time-averaged velocity and temperature profiles [2]. The findings well align with the Nusselt number in Table 4.2: higher values are indeed found all over the domain for the forced convection case, with Nu = 7.60, while lower values are evident for the mixed convection case with Ri = 0.75 corresponding to Nu = 9.30, with an increse of 26% compared to the forced case. This is more notable from the profiles reported in Figure 4.13: the highest value of $\overline{\theta_w} - \overline{\theta}$ is found for Ri = 0.24 while for Ri = 0.75 the decrease is evident in path I and II. It is noteworthy that the temperature difference in the radial direction along path I, then towards the centre of the channel, is indeed minimal for all the analysed cases as this feature is commonly observed in flows with high thermal conductivity and low Peclet numbers [107]. These findings are also consistent with previous literature on canonical case of channel flow with Re_τ [29] or turbulent pipe flow [126] characterised by low Prandtl number: the conduction region

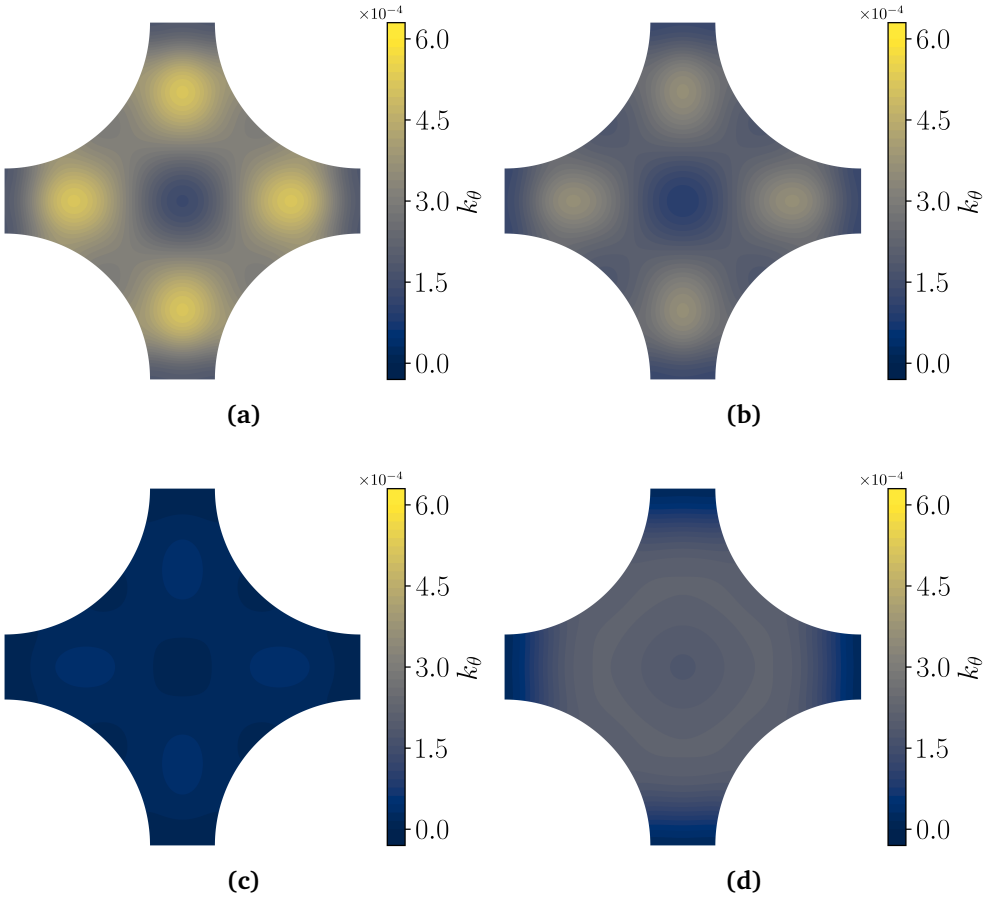

Figure 4.14: Time-averaged temperature fluctuations k_θ contours for: (a) Ri = 0, (b) Ri = 0.025, (c) Ri = 0.24, (d) Ri = 0.75.

extends more profoundly into the core region as the Prandtl number decreases.

The low Prandtl number considered in this study implies that temperature fluctuations k_θ calculated as

$$k_\theta = \frac{1}{2}\overline{\theta'\theta'} \tag{4.7}$$

are generally extremely low. Furthermore, in agreement with previous observations of the fluctuating velocity field, the buoyancy aid reduces the temperature fluctuations even further up to a certain Rayleigh number. To highlight this behaviour, the three cases are shown in Figure 4.14: compared to the forced case, as the Rayleigh

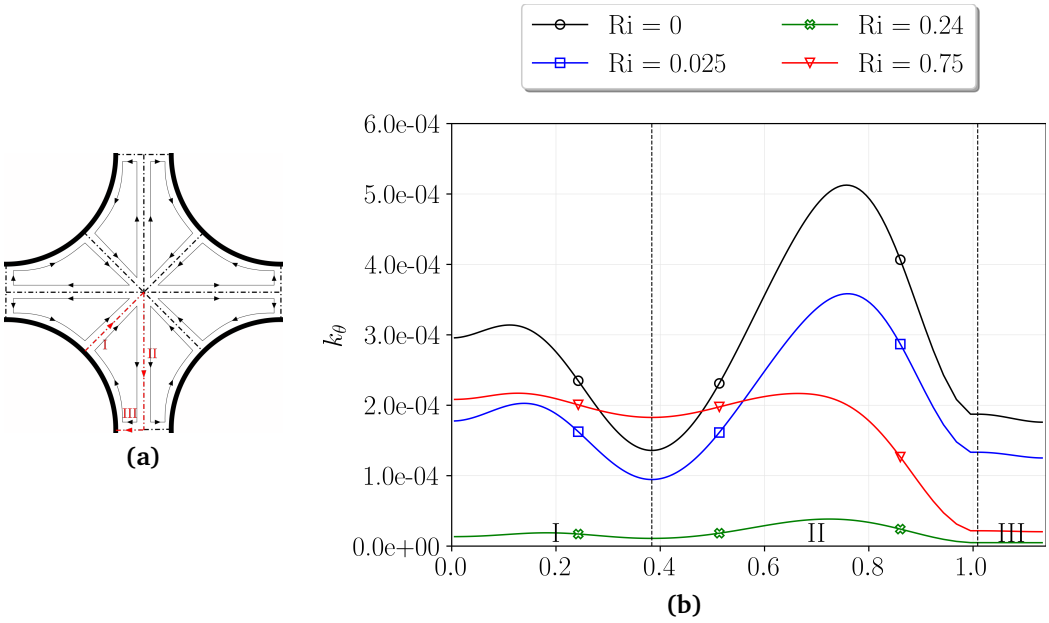

Figure 4.15: Profiles of k_θ for: ∘ Ri = 0, □ Ri = 0.025, × Ri = 0.24, ▽ Ri = 0.75.

number is increased, it can be seen that the temperature fluctuations undergo a drastic decrease throughout the domain for both mixed cases (see Figures 4.14c-4.14d). However the profiles illustrated in Figure 4.15, demonstrate that, for the case with Ri = 0.75, not only there is an increasing value of k_θ with respect to the case with Ri = 0.24 but also the value at the centre of the domain, between path I and II, is higher with respect to the forced case.

The streamwise turbulent heat fluxes $-\overline{u_z'\theta'}$ contours are reported in Figure 4.16: in general the values are really low and this result is expected for low Prandtl numbers because in terms of the transport of thermal energy, conduction plays a more prominent role than convection [35]. In Figure 4.16a the forced convection case exhibits peak values distributed in the proximity of the rod bundle, decreasing it in the center of the doamin and in the narrowest gaps between two adjacent rods. A general decrease is observed for the mixed convection case with Ri = 0.24 and Ri = 0.75 all over the domain, with also a little change in the position of the maximum values. Looking at the profiles in Figure 4.17 it can be pointed out that for the mixed case with Ri = 0.75 at the center of the domain there is a peculiar behaviour

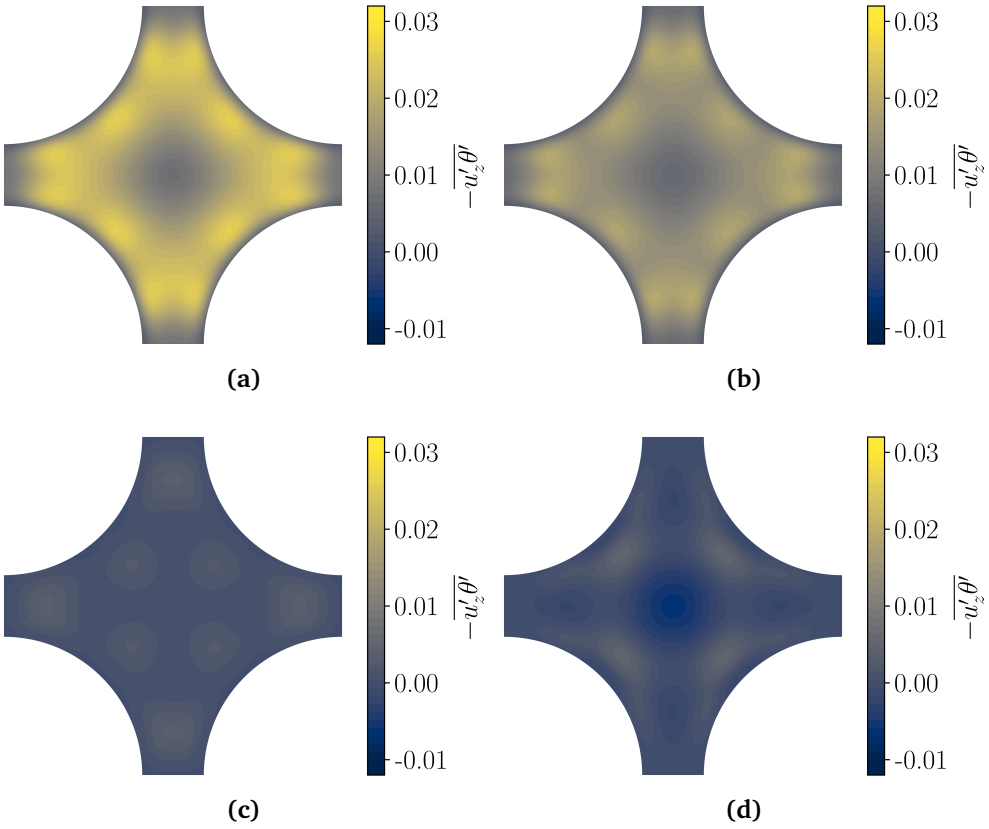

Figure 4.16: Time-averaged streamwise turbulent heat fluxes $-\overline{u_z'\theta'}$ for: (a) Ri = 0, (b) Ri = 0.025, (c) Ri = 0.24, (d) Ri = 0.75.

of the turbulent heat fluxes as the sign of this product changes and it is important to note that this coincides with the same area of the domain where a change in sign of the streamwise velocity derivative is observed (see Figure 4.3b). Furthermore, the profile shape for the forced case is coherent with previous findings for flow in a channel [31].

In addition to the streamwise turbulent heat fluxes, in Figures 4.18-4.19 time-averaged contours are reported for the turbulent heat fluxes $\overline{u_r'\theta'}$ and $\overline{u_\varphi'\theta'}$. From the comparison between the maps at Ri = 0, Ri = 0.24 and Ri = 0.75 it emerges that the behaviour of $\overline{u_r'\theta'}$ and $\overline{u_\varphi'\theta'}$ is similar to that of the Reynolds stresses $\overline{u_r'u_z'}$ and $\overline{u_\varphi'u_z'}$. An overall decrease of the turbulent heat fluxes emerges with aiding buoyancy,

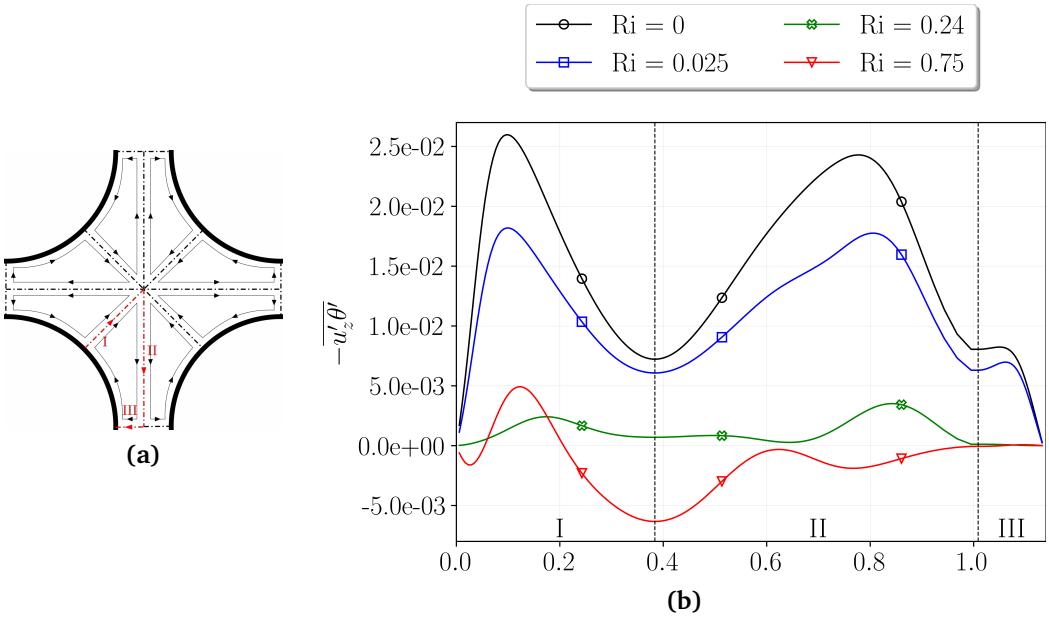

Figure 4.17: Profiles of $-\overline{u_z'\theta'}$ for: ∘ Ri = 0, □ Ri = 0.025, × Ri = 0.24, ▽ Ri = 0.75.

with a significant reduction for the wall-normal fluxes $\overline{u_r'\theta'}$, in accordance to the results obtained by Angeli *et al.* [112]. For $\overline{u_\varphi'\theta'}$ in Figure 4.18c (Ri = 0.75) there is an overall increasing of the value with respect to the case with Ri = 0.24, other then a change of sign as observed and described for $\overline{u_\varphi' u_z'}$ (Figure 4.9c).

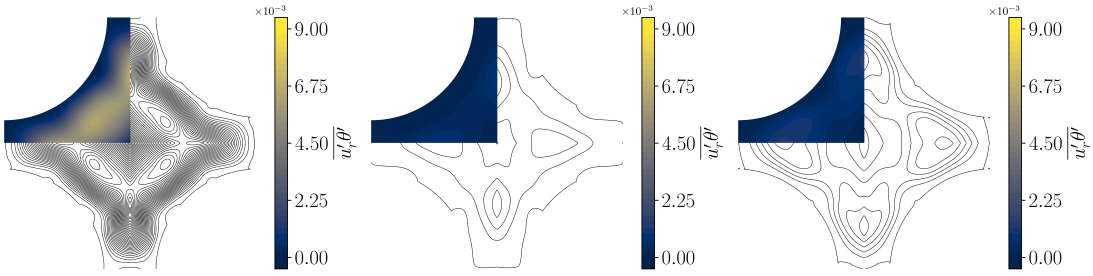

Figure 4.18: Time-averaged turbulent heat fluxes $\overline{u'_r\theta'}$ contours for: (a) Ri = 0, (b) Ri = 0.24, (c) Ri = 0.75.

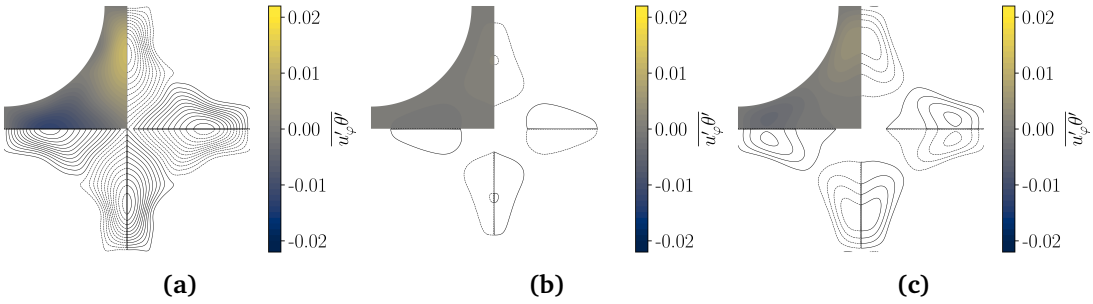

Figure 4.19: Time-averaged turbulent heat fluxes $\overline{u'_\varphi\theta'}$ contours for: (a) Ri = 0, (b) Ri = 0.24, (c) Ri = 0.75.

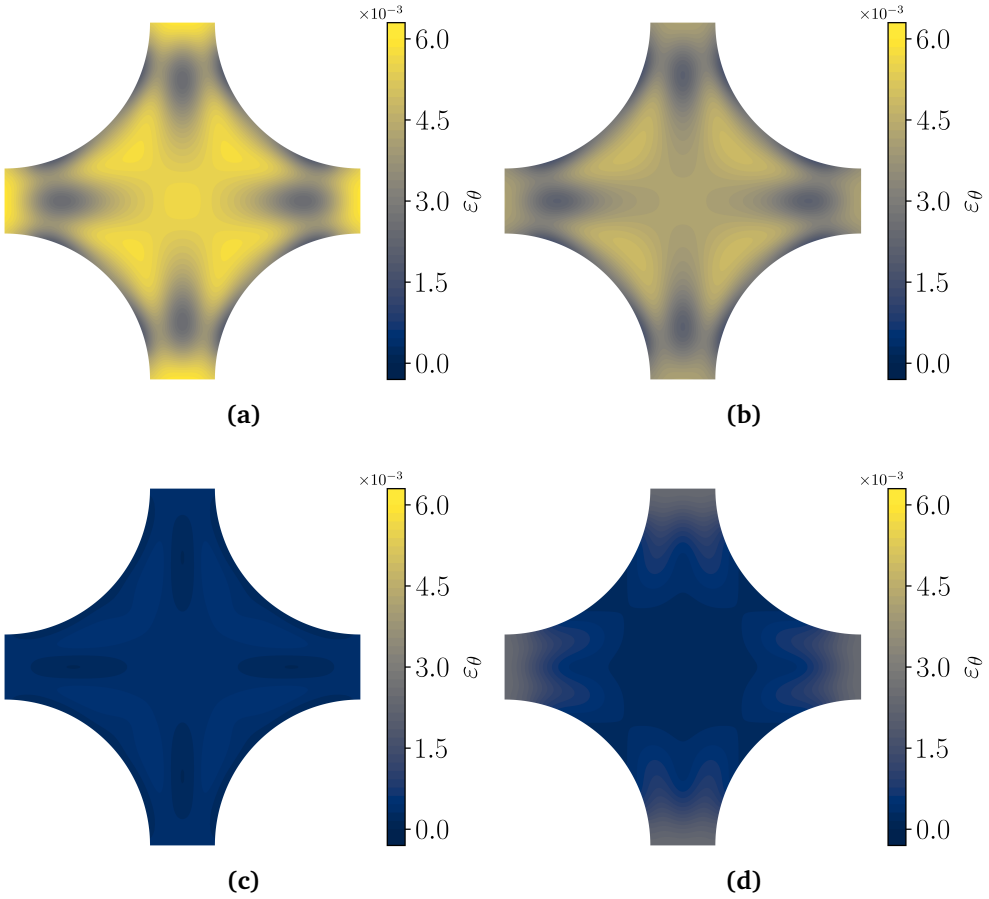

Figure 4.20: Time-averaged dissipation of the temperature variance ε_θ contours for: (a) Ri = 0, (b) Ri = 0.025, (c) Ri = 0.24, (d) Ri = 0.75.

The dissipation rate of the temperature variance ε_θ is defined as:

$$\varepsilon_\theta = \frac{1}{\mathrm{Re}_\tau \mathrm{Pr}} \left(\overline{\frac{\partial \theta'}{\partial x_i} \frac{\partial \theta'}{\partial x_i}} \right) \tag{4.8}$$

and its contours are shown in Figure 4.20. As expected for low Prandtl numbers, the values are minimal for both forced and mixed convection cases, with peak values achieved in the center of the channel. For Ri = 0 higher value are noted all over the domain and they decrease with the increasing Rayleigh number. For Ri = 0.75 it can be pointed out an increase of ε_θ in the region between adjacent rods, as highlighted in Figure 4.20d. The increased value is even more clear from the profiles in Figure

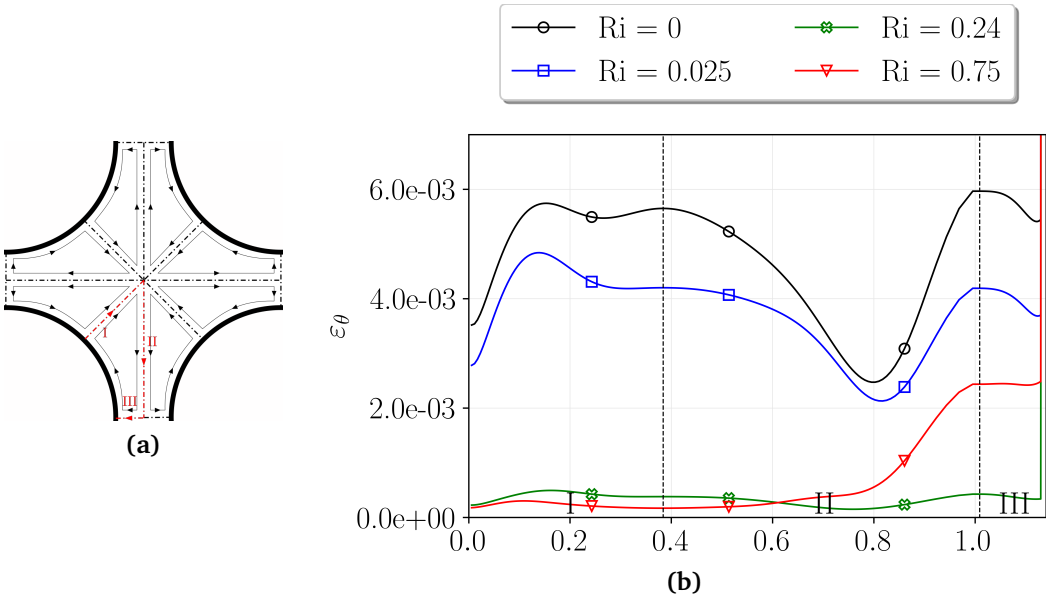

Figure 4.21: Profiles of ε_θ for: ∘ Ri = 0, □ Ri = 0.025, × Ri = 0.24, ▽ Ri = 0.75.

4.21, where the level of ε_θ for Ri = 0.75 starts to rise at the end of path II with respct to the case with Ri = 0.24.

As outlined in Chapter 2, the turbulent Prandtl number Pr_t is one of the most frequently occurring parameters in turbulence models. In most models, the turbulent Prandtl number is set to a constant value. This can lead to errors in the model's accuracy when it is applied to fluids with a low Prandtl number, or in conditions involving mixed or natural convection. It is therefore essential to formulate an expression that describes the behaviour of the turbulent Prandtl number, which varies within the domain. The general expression for the turbulent Prandtl number can be expressed as:

$$Pr_t = \nu_t/\alpha_t \tag{4.9}$$

where ν_t is the eddy kinematic viscosity and α_t is the thermal kinematic diffusivity.

By expanding the terms, the following equation is obtained:

$$Pr_t = \frac{-\overline{u_i' u_j'} / \left(\frac{\partial \overline{u_i}}{\partial x_j} \right)}{-\overline{u_j' \theta'} / \left(\frac{\partial \overline{\theta}}{\partial x_j} \right)} \tag{4.10}$$

Given that the domain under consideration is characterised by cylindrical geometries, while discussing about Pr_t the indices i and j will not be refered in terms of the Cartesian coordinates, but rather in terms of the cylindrical coordinates r and φ, defined as:

$$r = \sqrt{x^2 + y^2}, \varphi = \arctan(y, x) \tag{4.11}$$

Consequently, Pr_t can be written as:

$$Pr_t = \frac{-\overline{u_r' u_z'} \left(\frac{\partial \overline{\theta}}{\partial r} \right)}{-\overline{u_r' \theta'} \left(\frac{\partial \overline{u_z}}{\partial r} \right)} \tag{4.12}$$

in accordance with previously documented expression of the turbulent Prandtl number [112]. The contours of the turbulent Prandtl number as stated in Eq. 4.12 are reported in Figure 4.22. For the cases characterised by forced convection or weakly mixed convection, the value of Pr_t is uniformly around 2.5 within the domain for Ri = 0, while its value decreases slightly and takes on a less uniform trend for Ri = 0.025. In Figures 4.22c-4.22d, it is evident that there is a decrease in the value of Pr_t throughout the domain, with values decreasing to below 1.0 for Ri = 0.24 and approaching zero for Ri = 0.75. As shown in the contour plots presented in Figure 4.22, discontinuities are observed in proximity to the rods for all four cases, as well as within the fluid region when buoyancy effects become significant. This behaviour is primarily numerical in nature and may be attributed to the presence of steep gradients, as well as to the very small values of the turbulent heat flux observed for Ri = 0.24 and Ri = 0.75.

However, it is noteworthy that this formulation of Pr_t involves a further simplifi-

cation: as highlighted in Chapter 2.4, the original definition of the turbulent thermal diffusivity is tensorial in nature [127]. Moreover, in presence of mixed convection and anisotropic heat transfer, the tensor is non symmetric and as a consequence simplifying the contribution of Pr_t to purely the one defined in Eq. 4.12 could lead to inaccuracies. This point has also been emphasised in previous studies [36,128,129]. In this context, the Generalized Gradient Diffusion Hypothesis (GGDH), firstly introduced by Daly and Harlow [130], is a turbulence modeling approach that preserves the tensorial nature of the turbulent thermal diffusivity, which is more appropriately denoted as D_{ij} rather than α_t. For this reason, the GGDH model generally provides improved accuracy in complex geometries and in high-Rayleigh-number convection, albeit at a higher computational cost due to the need to resolve the Reynolds stresses. In light of the above considerations, in cases such as the one investigated in the present study the formulation of the turbulent Prandtl number as a constant number throughout the entire domain represents a considerable simplification. In reality, it would be more appropriate to treat it as a tensorial quantity. Exploring and modelling this property in a tensorial framework therefore is of significant interest for future investigation.

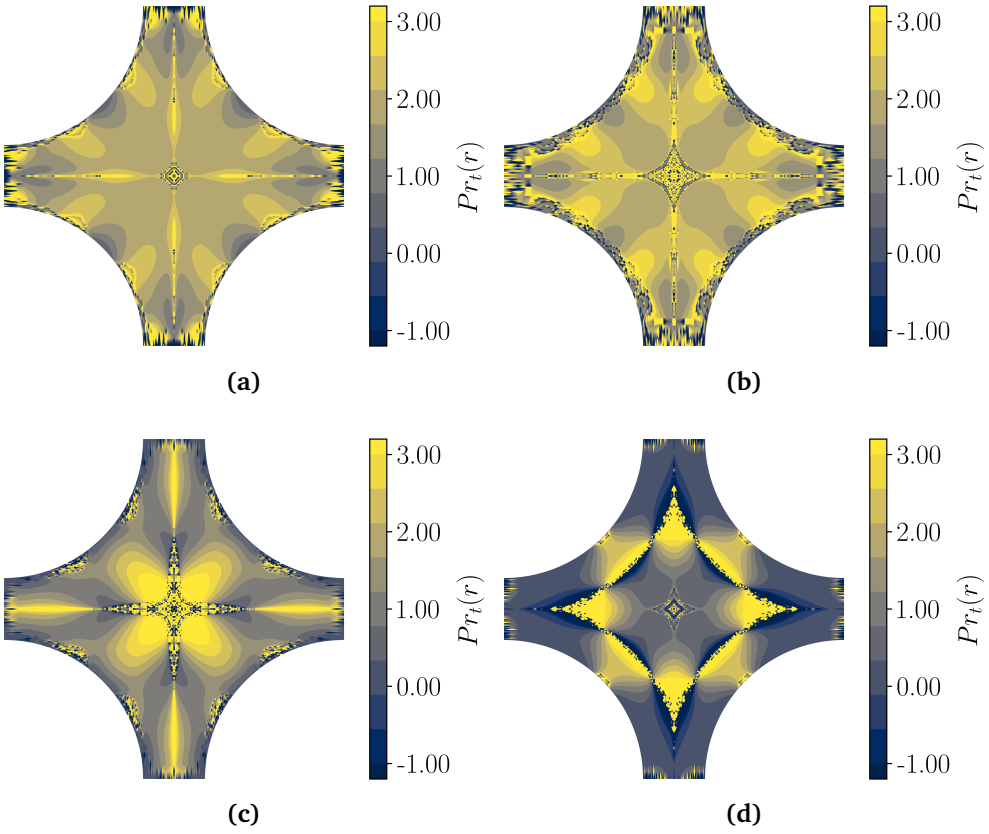

Figure 4.22: Time-averaged turbulent Prandtl number $Pr_t(r)$ contours for: (a) Ri = 0, (b) Ri = 0.025, (c) Ri = 0.24, (d) Ri = 0.75.

4.4. Turbulent budgets

In Chapter 2 it has been widely discussed how the assumptions in the most commonly used turbulence models are not ideal for fluids with a very low Prandtl number. Hence, development of more advanced turbulence models can be obtained with knowledge of the turbulent budgets. In this chapter the contributions to the turbulent kinetic energy and turbulent heat fluxes budgets will be briefly presented and discussed, examining the effects that the introduction of buoyancy has on the redistribution of contributions in the budgets.

4.4.1. Turbulent kinetic energy k budget

The turbulent kinetic energy (TKE) k balance equation is derived from the adimensional form of the continuity and momentum equation (3.9), by partitioning the variables into an average component and a fluctuating component and by multiplying these fuctuations with the momentum equation for the flutuating part. Subsequently, an averaging procedure is applied to the stress equations in both temporal and spatial domains. The resulting TKE balance equation, with detailed derivation in Appendix 8, is:

$$\frac{\partial k}{\partial t} = P_{ii} + C_{ii} + T_{ii} + \Pi_{ii} + D_{ii} + \varepsilon_{ii} + B_{ii} \tag{4.13}$$

where

$$\begin{aligned} &P_{ii} = -\overline{u_i' u_j'}\frac{\partial \overline{u_i}}{\partial x_j},\ C_{ii} = -\overline{u_j}\frac{1}{2}\frac{\partial \overline{u_i' u_i'}}{\partial x_j},\ T_{ii} = -\frac{1}{2}\frac{\partial \overline{u_i' u_i' u_j'}}{\partial x_j},\ \Pi_{ii} = -\frac{\partial \overline{p_m' u_i'}}{\partial x_j}\delta_{ij} \\ &D_{ii} = \frac{1}{\mathrm{Re}_\tau}\frac{\partial}{\partial x_j}\left(\overline{u_i'\frac{\partial u_i'}{\partial x_j}}\right),\ \varepsilon_{ii} = -\frac{1}{\mathrm{Re}_\tau}\overline{\frac{\partial u_i'}{\partial x_j}\frac{\partial u_i'}{\partial x_j}},\ B_{ii} = \frac{\mathrm{Gr}}{\mathrm{Re}_\tau^2}\overline{\theta' u_i'}\delta_{i3} \end{aligned} \tag{4.14}$$

Taking into consideration the forced case in Figure 4.23a, the peak production P_{ii} is reached in path I in the region close to the bundle and the maximum value (in modulus) of the dissipation ε_{ii} is observed in the same location. In the centre of the channel, on the other hand, we find a predominance of transport by Reynolds stresses T_{ii} . The positive contributions in this balance (mainly production and transport by Reynolds stresses) align with the trend observed in the previously analysed turbulent kinetic energy profiles, particularly in terms of the peak of turbulent ki-

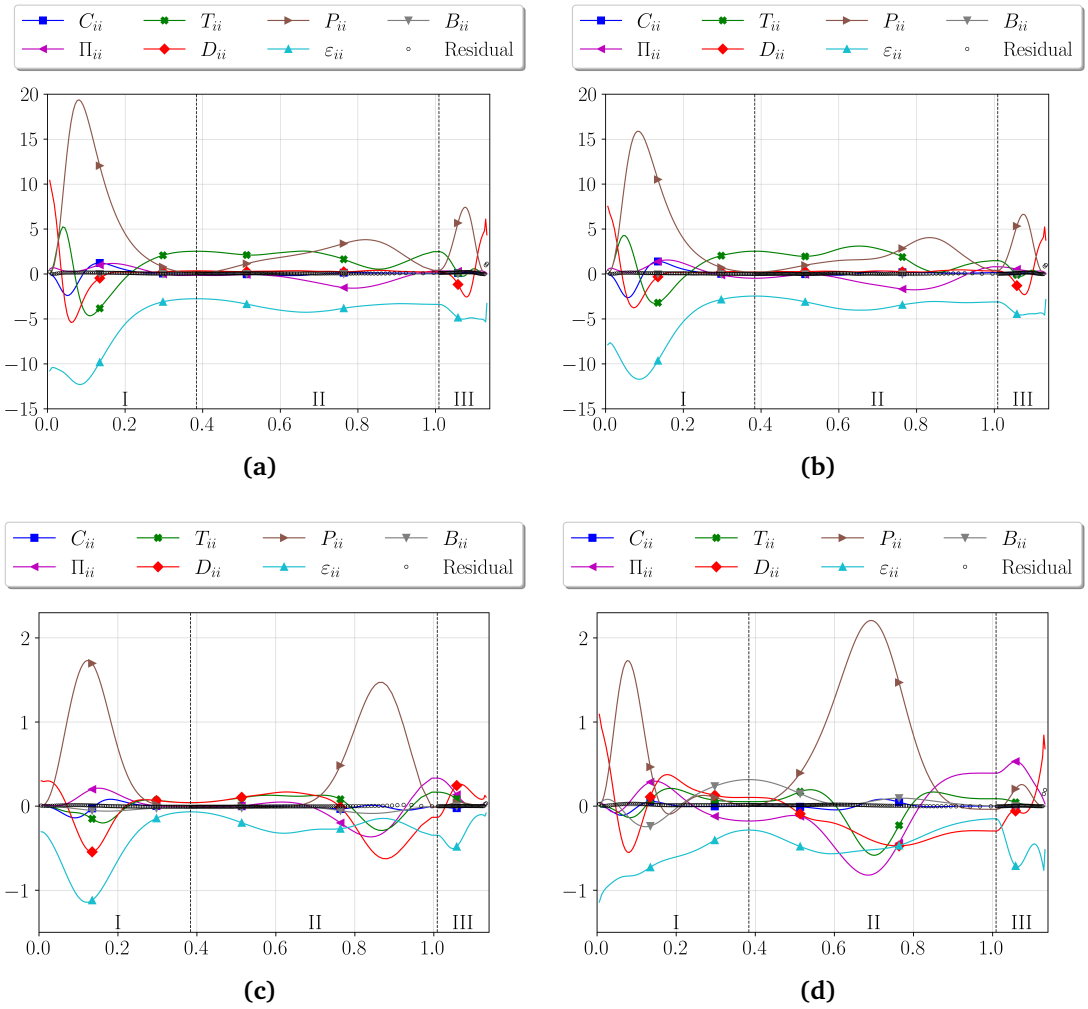

Figure 4.23: Profiles of TKE budget contributions for: (a) Ri = 0, (b) Ri = 0.025, (c) Ri = 0.24, (d) Ri = 0.75.

netic energy being situated at the maximum production value. The same contribution trend can be observed for the case with Ri = 0.025 in Figure 4.23b, confirming that this case behaves very similarly to the forced convection case. With the aiding buoyancy, there is a notable decline in contributions, which is observed to be approximately an order of magnitude and the same phenomenon is also evident in the turbulent kinetic energy profiles previously analysed. For this reason both Figure 4.23c and Figure 4.23d have a differently scaled y-axis compared to the two previous cases. For Ri = 0.24 (Figure 4.23c), two equivalent peaks of production are

observed: these peaks are located in the areas of path I and path II, respectively, not far from the bundles. The scenario undergoes a slight alteration when the mixed convection case with Ri = 0.75 is taken into consideration (Figure 4.23d). In this instance, the highest peak of production is no longer situated in path I, but rather in the middle of path II. This is in accordance with the observation that the turbulent kinetic energy has experienced an increase in value in this specific part of the domain when compared to the case with Ri = 0.24 (see Figure 4.6). Another aspect that stands out from the analysis of this case is how in the centre of the channel (the area at the intersection of path I and path II) the positive contribution to the balance is no longer made by the transport by Reynolds stresses but by the buoyancy term B_{ii}.

4.4.2. Turbulent heat flux $\overline{u_z'\theta'}$ budget

The momentum and energy equations 3.9 - 3.17 have been combined to derive the budget for the turbulent heat fluxes budget: for the sake of brevity, this discussion will focus only on the equation and the resulting outcomes for the transport of the quantity $\overline{u_z'\theta'}$:

$$\frac{\partial \overline{u_z'\theta'}}{\partial t} = P_{3\theta} + C_{3\theta} + \Phi_{3\theta} + T_{3\theta} + \Pi_{3\theta} + D_{3\theta} + \varepsilon_{3\theta} + B_{3\theta} \tag{4.15}$$

with

$$\begin{aligned}
P_{3\theta} &= -\left(\overline{\theta' u_j'}\frac{\partial \overline{u_z}}{\partial x_j} + \overline{u_z' u_j'}\frac{\partial \overline{\theta}}{\partial x_j}\right),\ C_{3\theta} = -\overline{u_j}\frac{\partial \overline{u_z'\theta'}}{\partial x_j},\ \Phi_{3\theta} = \overline{p_m'\frac{\partial \theta'}{\partial z}},\\
T_{3\theta} &= -\frac{\partial \overline{u_j' u_z'\theta'}}{\partial x_j},\ \Pi_{3\theta} = -\frac{\partial \overline{\theta' p_m'}}{\partial z},\ D_{3\theta} = \frac{1}{\mathrm{Re}_\tau}\frac{\partial}{\partial x_j}\left(\overline{\theta'\frac{\partial u_z'}{\partial x_j}} + \frac{1}{\mathrm{Pr}}\overline{u_z'\frac{\partial \theta'}{\partial x_j}}\right),\\
\varepsilon_{3\theta} &= -\left(\frac{1}{\mathrm{Re}_\tau} + \frac{1}{\mathrm{Re}_\tau \mathrm{Pr}}\right)\overline{\frac{\partial u_z'}{\partial x_j}\frac{\partial \theta'}{\partial x_j}},\ B_{3\theta} = \frac{\mathrm{Gr}}{\mathrm{Re}_\tau^2}\overline{\theta'\theta'} + \frac{\omega}{\Omega}\frac{1}{\mathrm{RePr}}\overline{u_z' u_z'}
\end{aligned} \tag{4.16}$$

In order to understand these graphs correctly, it is necessary to take into account the following convection: positive values denote a loss, while negative values indicate a gain. Starting from the forced case in Figure 4.24a the main contribution to the gain for $\overline{u_z'\theta'}$ is given, as expected, mainly by the production term $P_{3\theta}$, while

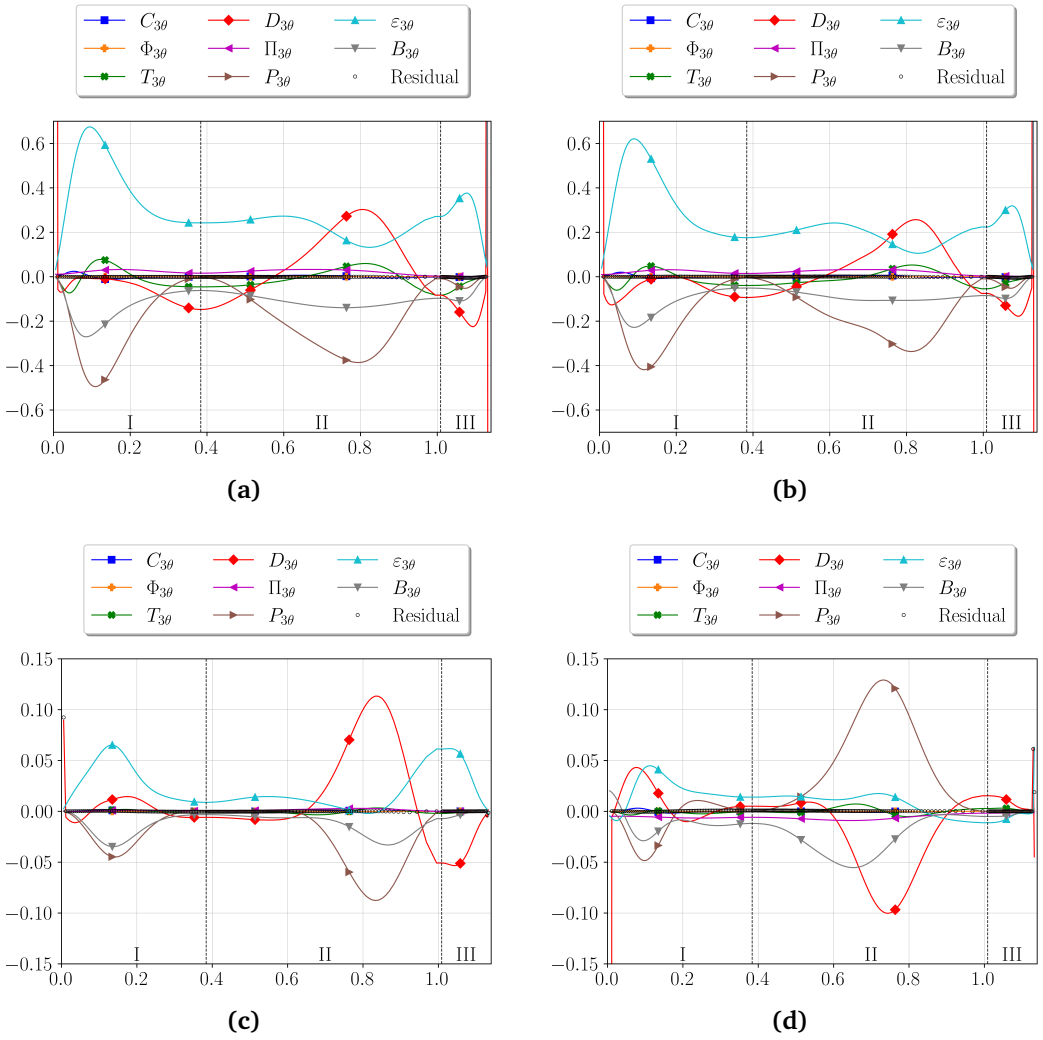

Figure 4.24: Profiles of turbulent heat flux $\overline{u_z'\theta'}$ budget contributions for: (a) Ri = 0, (b) Ri = 0.025, (c) Ri = 0.24, (d) Ri = 0.75.

for the loss part the dissipation $\varepsilon_{3\theta}$ emerges as the dominant factor in the loss component. As previously highlighted by [29] for a channel flow with $\mathrm{Re}_\tau = 180$, this behaviour is typical of low Prandtl number fluids: for fluids with $\mathrm{Pr} \geq 0.7$, the $\varepsilon_{i\theta}$ term is negligible. In contrast, dissipation $\varepsilon_{i\theta}$ is dominant in low Prandtl number fluids, because it takes place in eddies of a larger scale. One of the terms that seem to have an interesting behaviour is the transport by viscous stresses $D_{3\theta}$ which acts as gain in the center of the channel (between path I and II) and in the narrowest gap of

the domain (path III) and as loss in path II, with values even higher with respect to the dissipation itself. For the slightly mixed convection case the results are reported in Figure 4.24b: the details will not be listed for brevity since the budget terms assume almost the same behaviour as the forced convection case. Focusing now on the mixed convection case with Ri = 0.24 in Figure 4.24c some changes are noted: firstly the amplitude of the terms is lower with respect to the forced case (again note differently scaled y-axis). This was expected since also the value of $\overline{u_z'\theta'}$ commented in the previous sections showed lower values for the mixed convection cases. Apart from the lower value, the terms have almost the same behaviour: once again the main contribution to the gain is the the production, while for the loss the dissipation term is higher in path I and III but the peak value is achieved by the transport by viscous stresses in path II. The terms start to behave differently with increasing buoyancy, as can be seen in Figure 4.24d: for Ri = 0.75 the principal contribution to gain are due to the production term only near the bundle (beginning of path I) while all over the domain the heat fluxes are maintened by the buoyancy term $B_{3\theta}$ and expecially by the transport by viscous stresses in path II. At the maximum value of trasport by viscous in module corresponds the maximum value of loss which unexpectedly is given by the production term.

4.5. Final considerations

The statistical analyses presented in this chapter demonstrate that the characteristics of the flow undergo a substantial transformation as buoyancy assumes a more pronounced role. It is evident that for Ri = 0.75, the fluid exhibits distinct behaviour not only in comparison to the forced case, as would be anticipated, but also in contrast to another scenario of mixed convection (Ri = 0.24). This difficulty in predicting flow behaviour is a common occurrence in mixed convection regimes and thus presents a valuable opportunity for further study, both from a basic research perspective and in terms of developing new turbulence models for engineering applications.

Chapter 5

Flow development around a triangular rod bundle: a PIV-DNS cross-comparison

This case study is part of a benchmark exercise initiated by the Expert Group on Reactor Core Thermal-Hydraulics and Mechanics (EGTHM), utilizing the Advanced LFR European Demonstrator (ALFRED) as the reference system [131]. The EGTHM group provides coordinated international guidance to strengthen the modeling and validation of reactor core thermal-hydraulics for both existing and advanced nuclear systems. Moreover, the EGTHM group identifies data and methodological gaps, preserving and certifying high-quality experimental dataset, while also promoting international knowledge exchange through workshops, benchmarks, and training activities. [4]

To improve modeling accuracy for Lead-cooled Fast Reactors (LFRs) through comparison of simulations and experimental data, the benchmark proposed by the EGTHM group is structured in three phases. The present work focuses on Phase I, which examines spacer grid modeling by analyzing full-scale, isothermal, high-resolution Partial Image Velocimetry measurements conducted at Texas A&M University in collaboration with Westinghouse Electric Company [5]. Based on the provided specifi-

cations, a Direct Numerical Simulation (DNS) of fully developed flow in a bare rod bundle domain was performed to generate high-fidelity comparative results. As discussed in Chapter 2, expanding the current dataset to better represent liquid-metal fast reactor conditions is a primary motivation for conducting DNS. While it is inherent to DNS simulations that there is a embedded simplification of the domain with respect to the real application, this did not affect the usefulness of the collected data: in fact, it was possible to investigate features associated with the absence or presence of spacer grids, despite the inability to replicate the spacer grid in the DNS simulation. The absence of the spacer grid and the assumption of fully developed flow preclude analysis of developing boundary layers along the flow direction. Nonetheless, the DNS approach facilitated exploration of thermal phenomena not addressed in the experimental setup, thereby contributing valuable thermal hydraulic data.

5.1. Problem Statement

5.1.1. Reference Experiment

The experimental test section, described in detail by Menezes et al. [5], comprises a 127-pin assembly arranged in a triangular lattice within a transparent PMMA hexagonal flow channel. Each of the 127 pins is an annular borosilicate glass rod with an outside diameter of 11 mm, a rod-to-rod pitch of 13.66 mm, and a hexagonal flat-to-flat distance of 165.3 mm. The working fluid enters the assembly through a honeycomb flow straightener located at the lower end, then flows downstream where it encounters three asymmetrical honeycomb spacer grids. These spacer grids maintain constant rod spacing at specified axial intervals and introduce localized turbulence by obstructing the fluid flow. The hydraulic diameter of the bundle, D_h, is 9.347 mm. Measurement planes were selected at three locations: VP1 near the wall, VP2 in the intermediate region, and VP3 near the center of the assembly. Three axial elevations within the measurement window were chosen to assess the downstream effects of the spacer grid. As illustrated in Figure 5.1b, these planes are L_1 at $Y/D_h = 0.5$, L_2 at $Y/D_h = 2$, and L_3 at $Y/D_h = 10$.

The experiment was conducted by Menezes et al. [5] in isothermal conditions and at a Reynolds number (Re) of 6000, as part of the collection of PIV images. According to the Pacio-Chen-Todreas Detailed (PCTD) correlation [132, 133], for this Reynolds number, the flow lies in the transition regime. Steady flow conditions were ensured

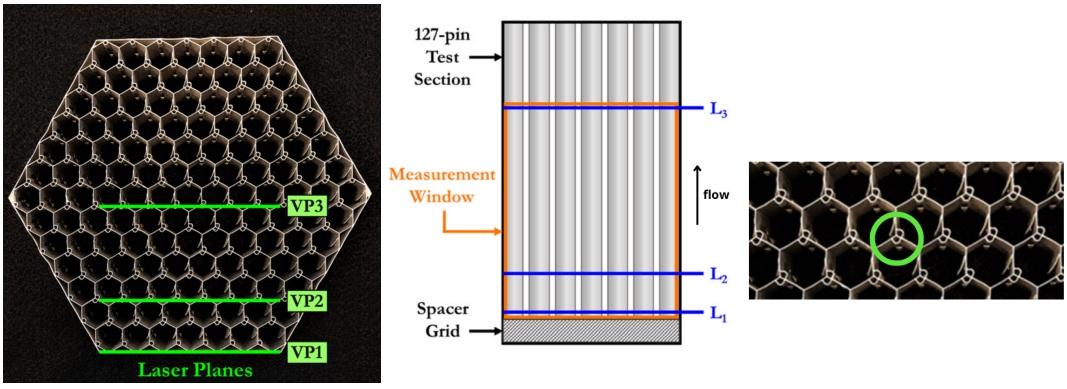

Figure 5.1: (a) Grid spacer [5], (b) Experimental setup [5], (c) Detail of rigid supports [5].

by allowing a sufficient flow circulation time prior to data acquisition.

5.1.2. Numerical Test Case

The numerical simulation is based on a partial representation of the experimental rod bundle described above. A periodic module of an infinite triangular lattice of rods with a pitch-to-diameter ratio $P/D = 1.24$ is considered as the numerical domain, representative of the centre bundles of the full 127-pin assembly (Figure 5.2a). In the cross-flow direction the module is made up of a rectangular cell consisting of 4 sub-channels, see figure 5.2b. Although the experiment did not include an investigation of heat transfer and this was not explicitly requested at this stage of the benchmark, heat transfer has also been considered. In this regard, each rod is assumed to be uniformly heated with a constant heat flux, while buoyancy effects are not considered.

The size of the computational domain is $1.77D_h \times 3.07D_h \times 6\pi D_h$, where D_h is the hydraulic diameter, calculated as 7.7046 mm for the specific configuration of the reference bundle. The number of control volumes along the three directions is $256 \times 440 \times 2048$. The grid has a constant spacing both in both the transverse x-y plane and the streamwise direction. With these parameters, the spacing is approximately $\Delta x^+ \approx \Delta y^+ \approx 2.8$, $\Delta z^+ \approx 3.7$. With an a posteriori estimation of the

Table 5.1: Grid

Quantity	-	$(\cdot)_x$	$(\cdot)_y$	$(\cdot)_z$
Domain size	$L_{(\cdot)}/D_h$	1.77	3.07	6π
no. of cells	$n_{(\cdot)}$	256	440	2048
spacing	$\Delta(\cdot)^+$	2.8	2.8	3.7
resolution	$\Delta(\cdot)/\eta_{min}$	1.7	1.7	2.2

Kolmogorov length scale, a value of $\Delta z \approx 2.2\eta_{min}$ is obtained. Additional parameters of interest are listed in Table 5.1.

To conduct a meaningful comparison between simulation data and experimental results, a friction Reynolds number (Re_τ) of 400 is set, leading to a corresponding bulk Reynolds number (Re_b) of 5843 once stability and self-similarity criteria are met. As the DNS method also allows the heat transfer part to be analysed, a Prandtl number value is chosen to represent eutectic liquid-bismuth lead (LBE) as the working fluid ($\mathrm{Pr} = 0.031$). Some of the flow and thermal parameters set for the simulation, along with relevant calculated integral values, are listed in Table 5.2.

5.2. Results and discussion

The following section will present an overview of the DNS results, starting with a comparison between the mean and fluctuating velocity fields with the reference

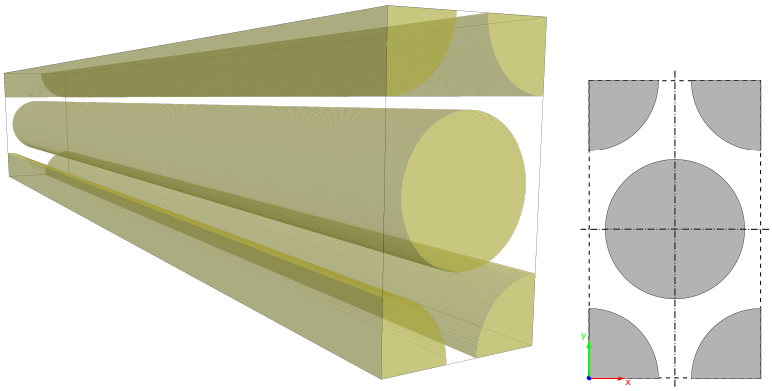

(a) **(b)**

Figure 5.2: (b) DNS cross section, (a) DNS 3D domain.

Table 5.2: Flow and thermal parameters for the DNSs performed and relevant integral values calculated.

Quantity		**Present DNS**
Friction Reynolds number	Re_τ	400
Prandtl number	Pr	0.031
Bulk Reynolds number	Re_b	5843
Bulk Peclet number	Pe_b	181
Nusselt number	Nu	10.6

experimental data. The final section will discuss the heat transfer aspects that the DNS accounts for. To ensure the comparability of the data, reference is made to the VP3 plane of the assembly (see Figure 4.1), which is most distant from wall effects, a condition similar to the periodic one present in the computational domain, and to the axial elevation L3, as it is the one most distant downstream of the spacer grid and shows self-similar behaviour. Although closer to the wall, profiles along VP1 line are also considered, due to the fact that the flow in the corresponding region is less perturbed by the spacer grid. Before going into the details, it should be noted that the quantities under analysis have been properly normalised, thus facilitating the establishment of meaningful comparisons. With regard to the velocity statistics, the velocity scale used is u_0 which is equal to 0.805 m/s for the DNS and it is calculated considering the bulk Reynolds number at statistically steady flow ($Re_b = 5843$), with $\nu = 1.077 \times 10^{-6}$ m^2/s; for the experimental set-up u_0 is the rod bundle bulk flow velocity, evaluated to be 0.676 m/s [5], corresponding to the assembly Reynolds number Re = 6000.

The normalised time-averaged streamwise velocity $\overline{u_z}/u_0$ contour field obtained from the computational analysis is illustrated in Figure 5.3a: it is evident that the maximum velocity value is observed at the centre of the subchannel, which can be interpreted as an anticipated outcome, as a similar trend has been found for similar configurations in previous simulations [3]. Profiles along the line represented in Figure 5.3a were then singled out to extrapolate data comparable the experimental

measurements obtained along the VP3 plane represented in Figure 5.1b. In Figure 5.3b the computed and the experimental profiles are presented in a side-by-side comparison: the DNS trend is characterised by a period P (rod-to-rod pitch of 13.66 mm), a feature also exhibited by the experimental profile VP3, but a different shape is

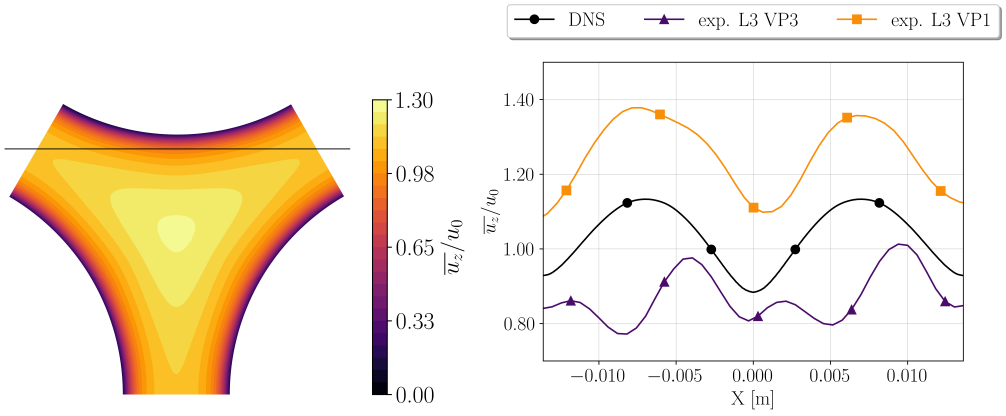

(a) **(b)**

Figure 5.3: (a) DNS contour of time-averaged streamwise velocity $\overline{u_z}/u_0$, (b) DNS and experimental profiles of $\overline{u_z}/u_0$.

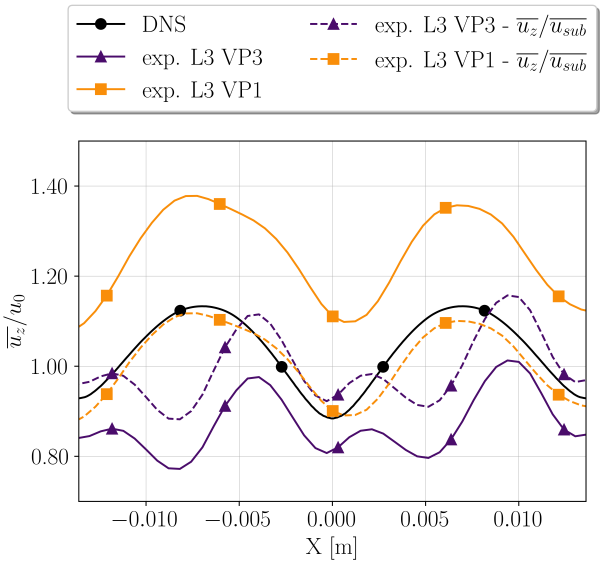

Figure 5.4: DNS and experimental profiles of streamwise velocity $\overline{u_z}$ normalised by u_0 or local average subchannel velocity $\overline{u_{sub}}$.

Table 5.3: Root Mean Square Error (RMSE) and Normalised Integral Error (NIE) for time-averaged streamwise velocity and time-averaged turbulent kinetic energy.

	$\overline{u_z}/u_0$ VP3	$\overline{u_z}/u_0$ VP1	k/u_0^2 VP3	k/u_0^2 VP1
RMSE	0.19	0.22	0.006	0.006
NIE	0.19	0.18	0.44	0.90

noted, probably due to the structure of the spacer grid, which has rigid supports (see Figure 5.1c) in the centre of the subchannels that could influence the velocity profile. In this regard, it becomes evident that when considering the profile identified in VP1, its shape conforms much better with the numerical profile, albeit with a higher mean velocity. The observed disparity in the mean velocity values is ascribable to the fact that, in the finite, 127-pin bundle, different flow rates estabilish in central and near-wall subchannels, and in the latter, the larger gap available produces a higher mean velocity. It is noteworthy that the absence of the rigid supports in the near-wall subchannels is reflected in the shape of the profiles. Evidence for these observations is provided by Figure 5.4, which shows the velocity profiles in VP1 and VP3, scaled with the local average velocity of the subchannel $\overline{u_{sub}}$. The velocity $\overline{u_{sub}}$ is calculated based on the experimental values found for the VP plane taken into consideration at axial elevation L3. The graph illustrates the congruence between the experimental profiles, which have been carefully scaled, and the simulation trend, thereby substantiating the hypothesis that in the absence of rigid supports within the domain, the experimental profile aligns with the numerical one.

In order to better assess the level of agreement between the DNS time-averaged streamwise velocity profile compared to the experimental data, Table 5.3 reports the Root Mean Square Error (RMSE) and the Normalised Integral Error (NIE) values: a RMSE value of 0.19 is observed if the data in the VP3 plane are considered while this value rises to 0.22 if the data in the VP1 plane are taken into account. Since the velocity profiles shown are already normalized with respect to the mean velocity, the orders of magnitude of the RMSE and NIE are obviously similar (see again Table 5.3), and they indicate that the relative deviations are of the order of 20%. Clearly, such deviations are mainly to be ascribed to the offset between the mean values of

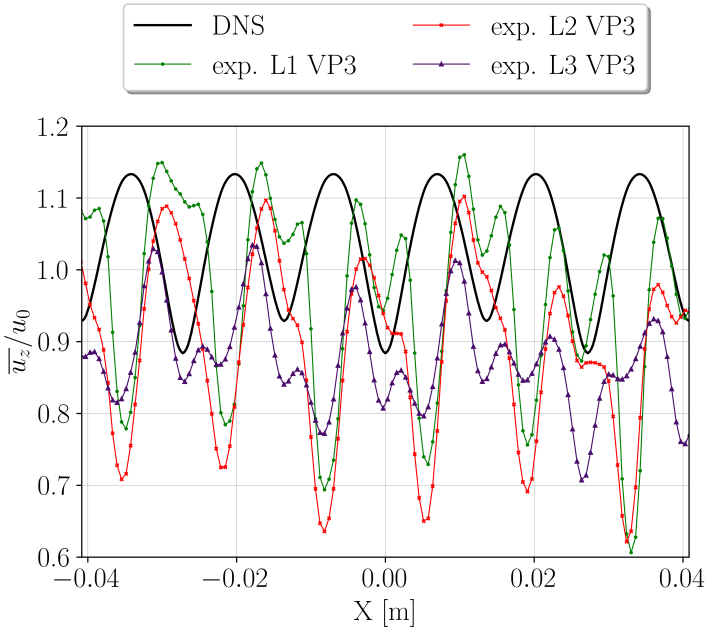

Figure 5.5: DNS and experimental profiles at different axial elevation (L1 - L2 - L3) of streamwise velocity $\overline{u_z}$ normalised by u_0.

the different profiles. However, since the mean flow rate of each subchannel in the experiment is not available, any further attempt towards an alignment of the profiles would be rather arbitrary.

Before proceeding with the analysis, the profiles presented in Figure 5.5 offer a comparative evaluation of the streamwise velocity $\overline{u_z}$ profiles in the VP3 plane at varying axial elevations with respect to the DNS profile. Considering the simulation domain, data across the entire width of the assembly are not available; consequently, the available DNS data have been extended by utilising the periodicity condition. Observing the profiles, beginning at the point immediately subsequent to the spacergrid L1 and extending towards the downstream location L3, the flow undergoes a transition towards a state of fully developed flow. Indeed, the profile most closely aligned with the behaviour of the DNS, which provides the most precise representation of fully developed flow, is the one at L3 axial elevation, both for its average value and for its shape.

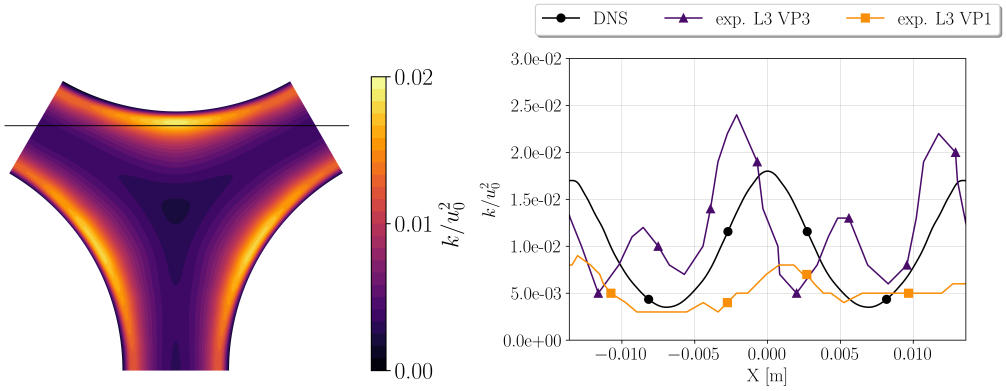

(a) **(b)**

Figure 5.6: (a) DNS contour of time-averaged turbulent kinetic energy k/u_0^2, (b) DNS and experimental profiles of k/u_0^2.

Similarly to what observed for velocity fields, the turbulent kinetic energy profiles exhibit some mutual differences when the reference profile VP3 is taken into consideration. However, if the quantities measured in VP1 are taken into account, the shape of the curve is more similar to that of the numerical simulation, albeit with a significantly lower average value, due to the presence of boundary effects (Figure 5.6b). The VP3 profile exhibits a higher maximum value than the DNS profile, primarily due to the presence of the spacer grid. This structural element not only preserves the geometric configuration but also enhances turbulence within the cross-flow plane, thereby contributing to the observed discrepancies [5]. This finding is supported by an inspection of the quantities $u'_{z,rms}$ and $u'_{x,rms}$: it is evident that, while the component in the streamwise direction ($u'_{z,rms}$) possesses nearly the same mean value (Figure 5.7a) as the spanwise component ($u'_{x,rms}$), which is significantly affected by the presence of the grid, as can be clearly seen in Figure 5.7b. It is important to note that the formula used for calculating the in-plane turbulent kinetic energy is the same as in the experiment: $k = \frac{1}{2}\left(\overline{u'_x u'_x} + \overline{u'_z u'_z}\right)$. In the context of the PIV assessment, the available data are confined to a single plane and thereby justifying the expression of k as defined above. Conversely, the computational approach provides a more comprehensive representation of k across all three components.
In Table 5.3, RMSE values are also reported for turbulent kinetic energy: these amount to 0.006 for both the VP3 and VP1 planes. Such low values are due to

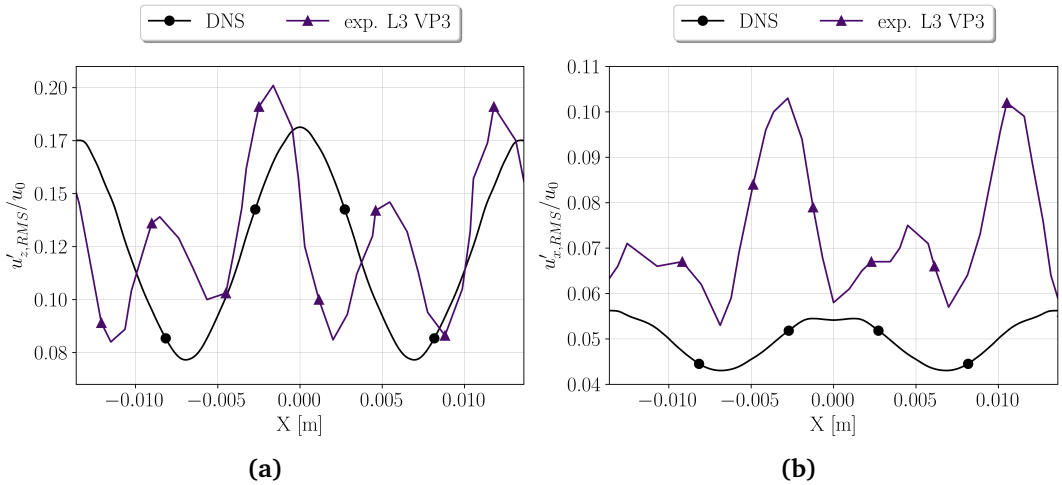

Figure 5.7: (a) Profiles of $u'_{z,rms}/u_0$, (b) Profiles of $u'_{x,rms}/u_0$.

the very small scale of the data taken into consideration and the RMSE alone may not reflect the real size of the error. To avoid this issue, Table 5.3 also shows the values obtained for the Normalised Integral Error (NIE): as previously noted, the values deviate more in the case of the VP1 plane, with a value of 0.90 for the NIE compared to 0.44 for the VP3 plane; this is in accordance with the large differences observed in the profiles.

In addition to velocity statistics, an obvious advantage of the present numerical approach is the possibility of obtaining heat transfer data. In the implemented code, the energy equation is expressed as a function of the fluid excess temperature θ, defined as the difference between the actual temperature and the reference temperature ($\theta(x,y,z) = T(x,y,z) - T_b(x)$) [3]. As demonstrated in Figure 5.8a the value of the time-averaged $\overline{\theta}$ field decreases moving from the bundle to the centre of the channel: this temperature difference is very small and this is a typical behaviour of flows with high thermal conductivity and low Péclet numbers [107]. The value of other heat transfer quantities can also be obtained, such as the temperature variance k_θ (Figure 5.8b) and the turbulent heat flux $-\overline{u'_z\theta'}$ (Figure 5.8c). In terms of temperature variance, the overall value is very low, as expected for liquid metals; the maximum value is reached at the centre of the channel, close to the rod. The same behaviour can be described for the heat fluxes $-\overline{u'_z\theta'}$. One aspect that would

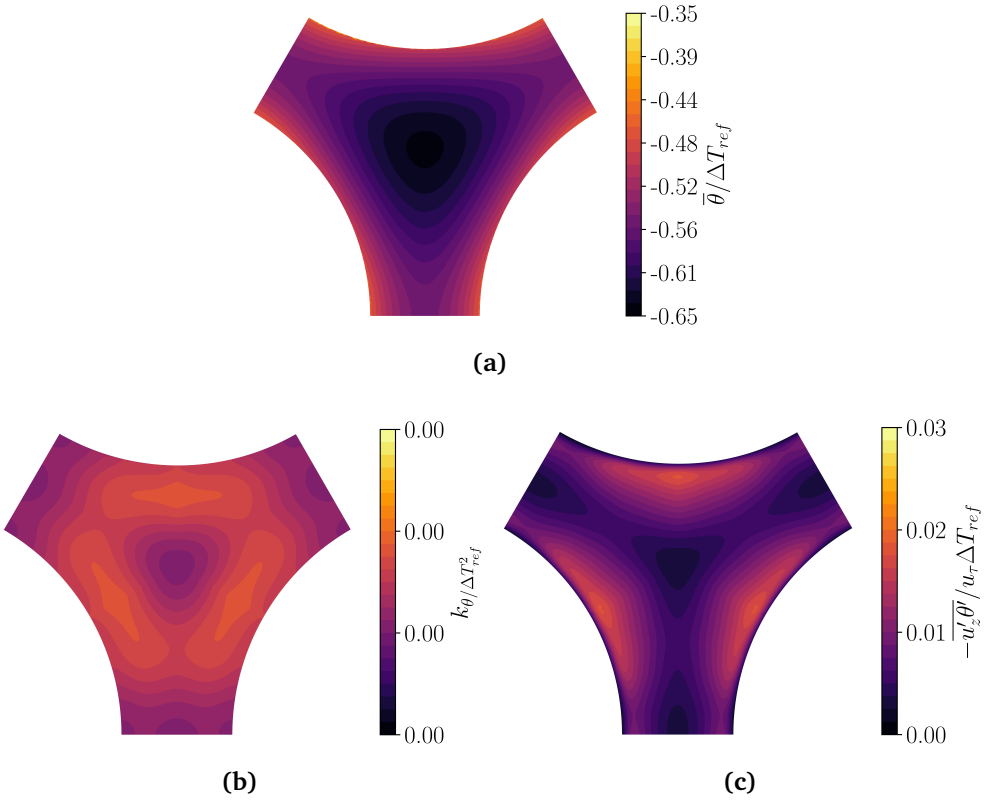

Figure 5.8: (a) DNS contour of time-averaged $\overline{\theta}/\Delta T_{ref}$, (b) DNS contour of time-averaged temperature variance $k_\theta/\Delta T_{ref}^2$, (c) DNS contour of time-averaged heat flux $-\overline{u_z'\theta'}/u_\tau\Delta T_{ref}$.

certainly need to be investigated is how the presence of the spacer grid (and thus of the rigid supports), whether through experiment or alternative numerical simulation, may affect the behaviour of these quantities. It has been demonstrated by prior research [134, 135] that the presence of the grid increases heat transfer. However, it is important to note that these analyses refer to configurations that utilise water or gas as a coolant.

To further assess the accuracy of the findings and contextualise this case within existing literature, reference to previously gathered correlations is now made. As already shown in Table 5.2, the Nusselt number obtained from the DNS is 10.6. In Figure 5.9 this value is compared with some correlation from the review of Mikityuk [136]:

- Subbotin *et al.* (1965) [137]:

$$Nu = 0.58\left(\frac{2\sqrt{3}}{\pi}\left(\frac{P}{D}\right)^2 - 1\right)^{0.55} Pe^{0.45} \tag{5.1}$$

- Borishanski *et al.* (1969) [138]:

$$Nu = 24.15log\left(-8.12 + 12.76\left(\frac{P}{D}\right) - 3.65\left(\frac{P}{D}\right)^2\right) + 0.0174(1 - \exp^{-6(P/D-1)})B \tag{5.2}$$

  where $B = 0$ for $Pe < 200$ and $B = (Pe - 200)^{0.9}$ for $Pe \geq 200$

- Gräber and Rieger (1972) [139]:

$$Nu = 0.25 + 6.2\left(\frac{P}{D}\right) + \left(0.032\left(\frac{P}{D}\right) - 0.007\right) Pe^{0.8 - 0.024P/D} \tag{5.3}$$

- Mikityuk (2009) [136]:

$$Nu = 0.047(1 - \exp^{-3.8(P/D-1)})(Pe^{0.77} + 250) \tag{5.4}$$

For the previous correlations, a value of $P/D = 1.24$, consistent with that of the case study, is selected. The evolution of the Nusselt number as a function of the Peclet number ($Pe = RePr$) is illustrated in Figure 5.9. To compare the numerical findings with existing literature, the obtained Nusselt number is evaluated against the correlations proposed by Gräber and Rieger [139] and Mikityuk [136]. While these correlations originate from experimental analyses with slight differences in domain configuration, the numerical result align more closely with the Gräber and Rieger correlation. Notably, Mikityuk identifies the Gräber and Rieger correlation as one of the most reliable, using it as a reference in a comprehensive review of existing correlations [136]. From the correlations considered, it is evident that the simulation value is more closely aligned with more recently extrapolated correlation curves than with 'older' ones. This underscores the ongoing necessity for fundamental research (both numerical and experimental) in the field of heat transfer around cylindrical rods.

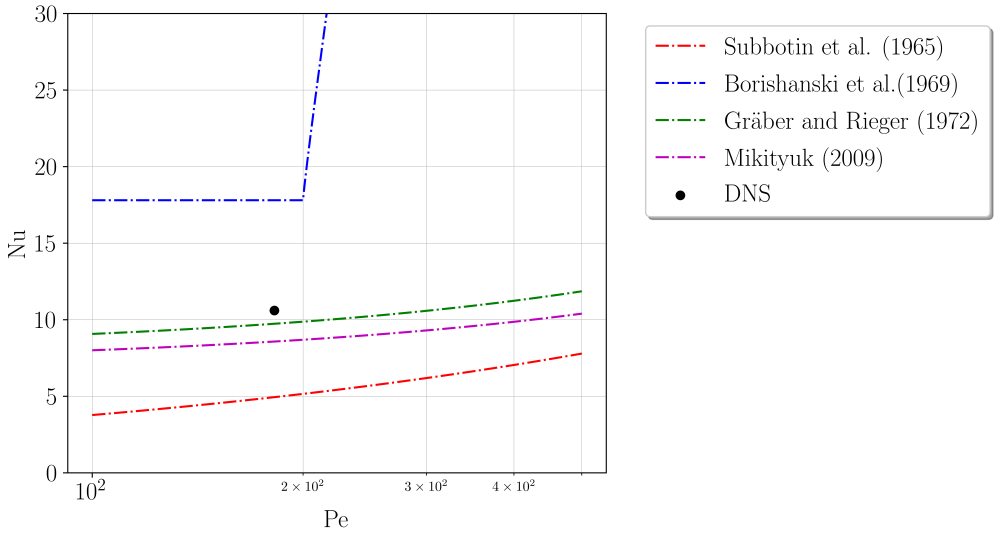

(a)

Figure 5.9: DNS vs literature correlations for P/D = 1.24.

5.3. Turbulent budgets

The section presents a brief overview on the budget contributions for the turbulent kinetic energy and turbulent heat fluxes transport equations.
In order to facilitate a more comprehensive understanding on the outcomes of the contributions, reference will be made to three segments that have been identified along the perimeter of a unit flow cell. As illustrated in the Figure 5.10, it is possible to recognise the six unit flows that characterise the subchannel, in addition to the three segments designated as I, II and III.

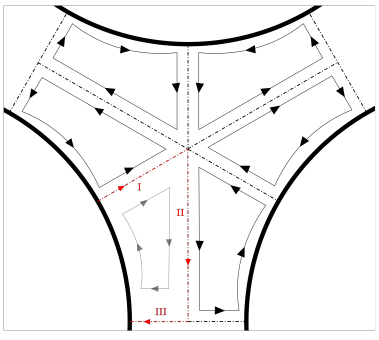

Figure 5.10: Schematic of a subchannel containing 6 unit flow cells.

The turbulent kinetic energy (TKE) balance equation is derived from the adimensional form of the continuity (3.1) and momentum equation (3.9):

$$\frac{\partial k}{\partial t} = P_{ii} + C_{ii} + T_{ii} + \Pi_{ii} + D_{ii} + \varepsilon_{ii} + B_{ii} \tag{5.5}$$

where

$$\begin{aligned} P_{ii} &= -\overline{u_i' u_j'}\frac{\partial \overline{u_i}}{\partial x_j},\ C_{ii} = -\overline{u_j}\frac{1}{2}\frac{\partial \overline{u_i' u_i'}}{\partial x_j},\ T_{ii} = -\frac{1}{2}\frac{\partial \overline{u_i' u_i' u_j'}}{\partial x_j},\ \Pi_{ii} = -\frac{\partial \overline{p_m' u_i'}}{\partial x_j}\delta_{ij} \\ D_{ii} &= \frac{1}{\mathrm{Re}_\tau}\frac{\partial}{\partial x_j}\left(\overline{u_i'\frac{\partial u_i'}{\partial x_j}}\right),\ \varepsilon_{ii} = -\frac{1}{\mathrm{Re}_\tau}\overline{\frac{\partial u_i'}{\partial x_j}\frac{\partial u_i'}{\partial x_j}},\ B_{ii} = \frac{\mathrm{Gr}}{\mathrm{Re}_\tau^2}\overline{\theta' u_i'}\delta_{i3} \end{aligned} \tag{5.6}$$

The analysis of Figure 5.11 indicates that, in the regions closest to the bundle, the budget is predominantly influenced by production P_{ii} and dissipation ε_{ii} contributions, while transport phenomena T_{ii} manifest more prominently in the central part of the subchannel. A key area of future research interest lies in the understanding of how the spacer grid's interaction with the flow can modify the Reynolds stress transport term T_{ii}.

The momentum and energy equations (3.9) - (3.17) have been combined to derive the budget for the turbulent heat fluxes budget: for the sake of brevity, this discussion will focus only on the equation and the resulting outcomes for the transport of the quantity $-\overline{u_z'\theta'}$:

$$\frac{\partial \overline{u_z'\theta'}}{\partial t} = P_{3\theta} + C_{3\theta} + \Phi_{3\theta} + T_{3\theta} + \Pi_{3\theta} + D_{3\theta} + \varepsilon_{3\theta} + B_{3\theta} \tag{5.7}$$

with

$$\begin{aligned} P_{3\theta} &= -\left(\overline{\theta' u_j'}\frac{\partial \overline{u_z}}{\partial x_j} + \overline{u_z' u_j'}\frac{\partial \overline{\theta}}{\partial x_j}\right),\ C_{3\theta} = -\overline{u_j}\frac{\partial \overline{u_z'\theta'}}{\partial x_j},\ \Phi_{3\theta} = \overline{p_m'\frac{\partial \theta'}{\partial z}}, \\ T_{3\theta} &= -\frac{\partial \overline{u_j' u_z'\theta'}}{\partial x_j},\ \Pi_{3\theta} = -\frac{\partial \overline{\theta' p_m'}}{\partial z},\ D_{3\theta} = \frac{1}{\mathrm{Re}_\tau}\frac{\partial}{\partial x_j}\left(\overline{\theta'\frac{\partial u_z'}{\partial x_j}} + \frac{1}{\mathrm{Pr}}\overline{u_z'\frac{\partial \theta'}{\partial x_j}}\right), \\ \varepsilon_{3\theta} &= -\left(\frac{1}{\mathrm{Re}_\tau} + \frac{1}{\mathrm{Re}_\tau \mathrm{Pr}}\right)\overline{\frac{\partial u_z'}{\partial x_j}\frac{\partial \theta'}{\partial x_j}},\ B_{3\theta} = \frac{\mathrm{Gr}}{\mathrm{Re}_\tau^2}\overline{\theta'\theta'} + \frac{\omega}{\Omega}\frac{1}{\mathrm{RePr}}\overline{u_z' u_z'} \end{aligned} \tag{5.8}$$

As with the TKE budget, the major contributions are made by the $P_{3\theta}$ and $\varepsilon_{3\theta}$ terms. However, as one moves towards the centre of the subchannel, the profiles generally flatten out towards an almost zero contribution, in accordance with the very low $-\overline{u_z'\theta'}$ values identified in Figure 5.8c.

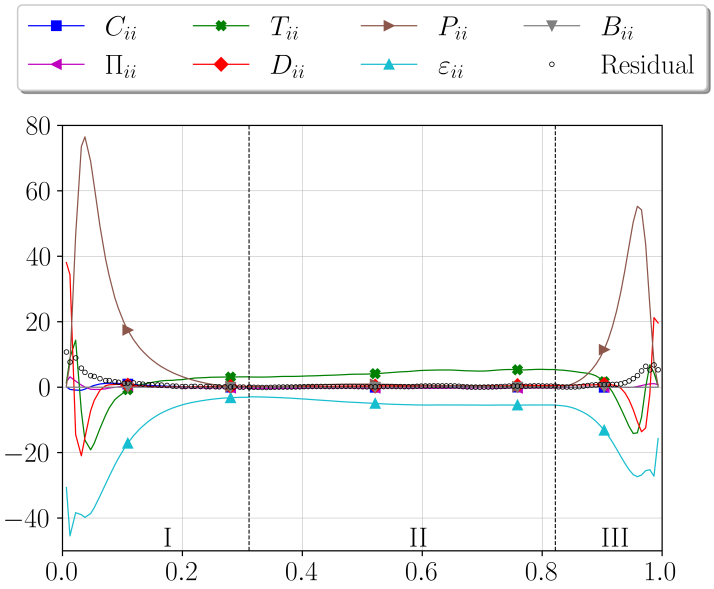

Figure 5.11: Profiles of TKE budget contributions.

5.4. Final considerations

DNS results have been compared with experimental measurements of turbulent flow in rod bundles. The study focuses on a benchmark problem exercise by EGTHM, based on experiments conducted at Texas A&M University in collaboration with Westinghouse Electric Company. Overall, the DNS results show good agreement with the experimental data. For example, the time-averaged velocity profiles are similar, even though their shapes differ because, in the experiments, the spacer grid and structural supports significantly affect the flow. The influence of the spacer grid becomes even more evident when examining turbulent kinetic energy and its components. In the experiments, the presence of the grid produces much larger fluctuations in the crossflow direction than observed in the simulations, where the grid is absent. The DNS data can serve as an effective alternative to experimental measurements taken downstream of the spacer grids, where fully developed flow conditions

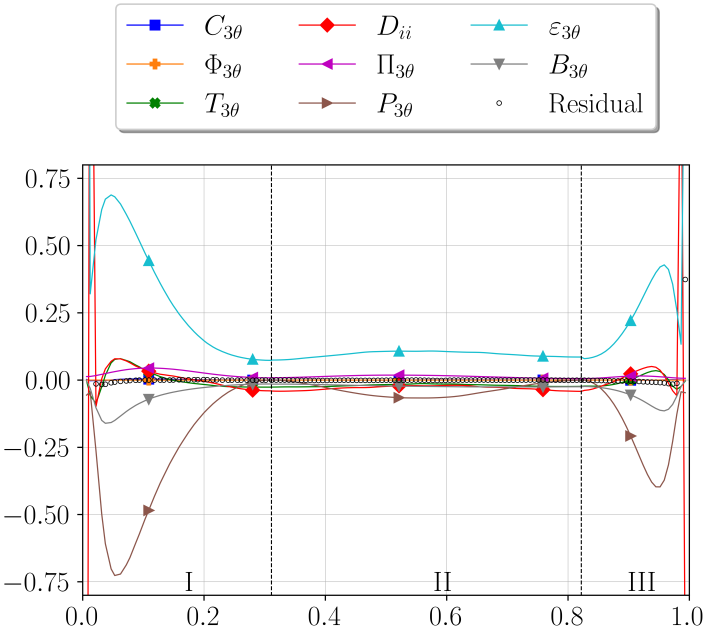

Figure 5.12: Profiles of $-\overline{u_z'\theta'}$ budget contributions.

are re-established. This can be very beneficial in the context of the benchmark, as it provides participants with an additional reference point to help them better interpret the experimental results. In general, the results are consistent with previous findings reported in the literature. Looking ahead, this work represents an important link between CFD and experimental research, supporting the development and validation of thermo hydraulic models for current and next-generation reactors. Future efforts could include studying the thermal side of the experiment where feasible, or extending DNS to additional operating conditions, such as mixed convection scenarios.

CHAPTER 6

Hybrid turbulence modelling

In the following section, an alternative application of high-fidelity data to the development of new models will be discussed. As stated in Chapter 2, if large industrial facilities are taken into account, LES models entail a high computational cost while RANS models are not able to fully predict the behaviour of fluids that diverge from the most frequently employed. Hybrid turbulence models can represent a good compromise: in the context of this study, a hybrid turbulence model using data-driven techniques will be presented. This work was carried out during a research stay at *von Karman Institute for Fluid Dynamics* (Sint-Genesius-Rode, Belgium) under the supervision of Dr. L. Koloszar and Dr. M. Fiore.

Starting from a reference DNS dataset, a target viscosity is determined, which is then used to define an α parameter that corrects the sub-grid viscosity of the Smagorinsky model. This α parameter is estimated using an Artificial Neural Network (ANN). The inputs to the ANN consist of parameters that are considered to provide the most accurate description of the flow characteristics.

6.1. LES filtering

The data obtained from the DNS case previously presented in Chapter 5 are used to reproduce LES simulation outcome. A filtering operation is defined to decompose

the quantity ϕ into the sum of a filtered (or resolved) component $\tilde{\phi}$ and a residual (or subgrid-scale, SGS) component ϕ_{sg} :

$$\phi = \tilde{\phi} + \phi_{sg} \tag{6.1}$$

The filtered field $\tilde{\phi}$ - which is three-dimensional and time-dependent - represents the motion of the large eddies. The equations for the evolution of the filtered velocity field are derived from the Navier-Stokes equations. These equations are of the standard form, with the momentum equation containing the SGS stress tensor that arises from the residual motions. The closure of these equations is obtained by modelling the residual-stress tensor, most simply by an eddy-viscosity model. [140] The general filtering operation is defined by:

$$\tilde{\phi} = \int_{-\inf}^{\inf} \phi(\boldsymbol{r}, t) G(\boldsymbol{r} - \zeta, t) d\zeta \tag{6.2}$$

In the present case, the resolved field $\tilde{\phi}$ is obtained filtering the existing DNS data through a box filter:

$$G(\boldsymbol{r}, \zeta) = \begin{cases} \frac{1}{\overline{\Delta}}, & \text{if } |\boldsymbol{r} - \zeta| \leq \frac{\overline{\Delta}}{2}, \\ 0, & \text{otherwise} \end{cases} \tag{6.3}$$

where $\overline{\Delta}$ is the cut-off length. The cut-off length used in the filer is defined as a multiple of the grid resolution:

$$f_{coars} = \frac{\overline{\Delta}}{\Delta_{grid}} \tag{6.4}$$

The box filter is applied in the three directions of the computational domain, with the coarsening factor f_{coars} varying in order to obtain a dataset that includes different grid resolutions.

Due to the nature of the domain, certain adjustments had to be made during the filtering phase. In order to apply the periodicity conditions (listed below), it is necessary to increase the size of the matrix, according to the coarsening factor f_{coars} adopted, to prevent the convolution operations from 'cutting' the data at the edges

(see Figure 6.1). Furthermore, the presence of immersed boundaries must be considered: as the box filter approaches the edge of the rods, the convolution operation will inevitably include cells with a value of zero (inside the rod). This will affects the result of the filtered quantity. To overcome this problem, a zero value is imposed in an area equal to an annulus around the rods, the thickness of which is a function of the chosen coarsening factor f_{coars} (see Figure 6.2). This will result in the exclusion of all affected values downstream of the filtering operations.

In the padded part of the matrix periodic conditions are applied in the streamwise and spanwise directions:

$$\phi(-x,-y,-z) = \phi(L_x - x, L_y - y, L_z - z) \tag{6.5}$$

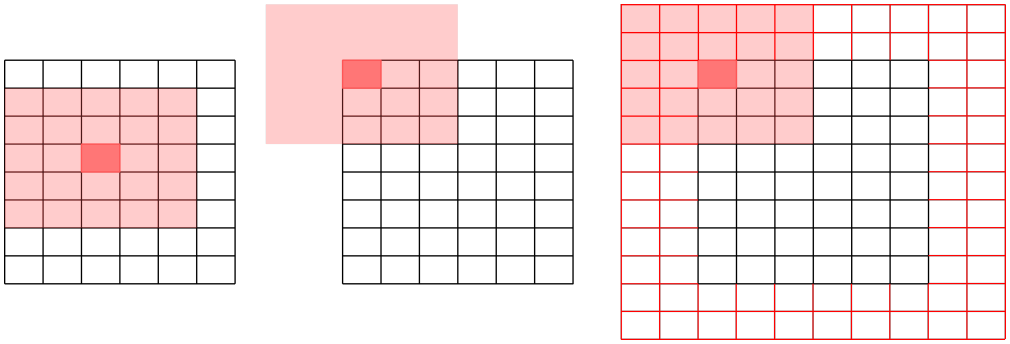

(a)

Figure 6.1: Padding matrix

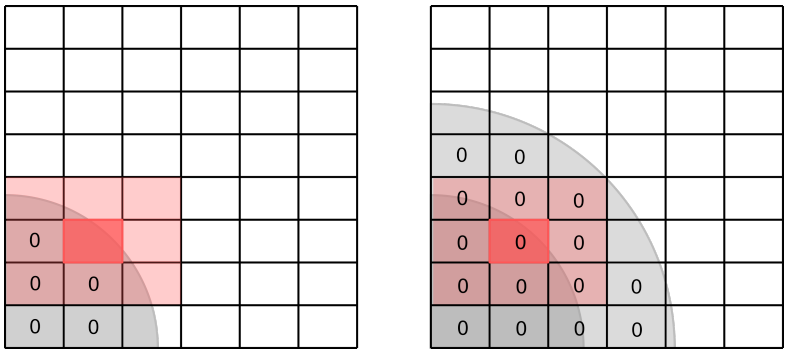

(a)

Figure 6.2: Immersed boundaries

$$\phi(L_x + x,\, L_y + y,\, L_z + z) = \phi(x,\, y,\, z) \tag{6.6}$$

Some results for filtered streamwise velocity $\tilde{u_z}$ fields are shown in Figure 6.3: the images presented demonstrate that, for coarsening factors f_{coars} greater than 8, the outcomes may be compromised due to the inherent characteristics of the computational domain. In the specific cases of $f_{coars} = 10$ and $f_{coars} = 15$, the excluded parts near the rods are found to be in close proximity, thereby significantly diminishing the available data.

Figure 6.4 shows the wall velocity profile $\tilde{u_z^+}$ obtained for different coarsening factors. The wall velocity profile $\tilde{u}_z^+$ extracted from path I, as shown in Figure 5.10, complies with the log-law of the wall. However, as a consequence of the exclusion of certain points in proximity to the rods (as previously discussed), some information is, ineluctably, excluded.

From the available DNS dataset, the sub-grid stress tensor τ_{ij} and $\tilde{S}_{ij}$ resolved strain tensor are calculated, for different grid resolution, as:

$$\tau_{ij} = \widetilde{u_i u_j} - \tilde{u}_i \tilde{u}_j \tag{6.7}$$

$$\tilde{S}_{ij} = \frac{1}{2}\left(\partial_i \tilde{u}_j + \partial_j \tilde{u}_i\right) \tag{6.8}$$

The eddy viscosity is then defined as the proportionality constant between the deviatoric stress tensor and the strain tensor:

$$\tau_{ij} - \delta_{ij}\frac{\tau_{kk}}{3} = -2\nu_{sg}\,\tilde{S}_{ij} \tag{6.9}$$

It follows that the target is to be defined as the proportionality constant between the two tensors, such that the following relationship is established:

$$\nu_{sg}^{target} = -\frac{1}{2}\frac{\tau^D : \tilde{S}}{\tilde{S} : \tilde{S}} \tag{6.10}$$

The results obtained for the target sub-grid eddy viscosity ν_{sg}^{target} are reported in Figure 6.5: as is evident also from the analysis of ν_{sg}^{target}, the findings are no

longer reliable for values of f_{coars} greater than 8. The target sub-grid eddy viscosity increases with the increasing coarsening factor, as expected, until $f_{coars} = 8$.

The target sub-grid eddy viscosity is used to define the correction factor α:

$$\alpha = \frac{\nu_{sg}^{target}}{\nu_{sg}^{Smag}} \tag{6.11}$$

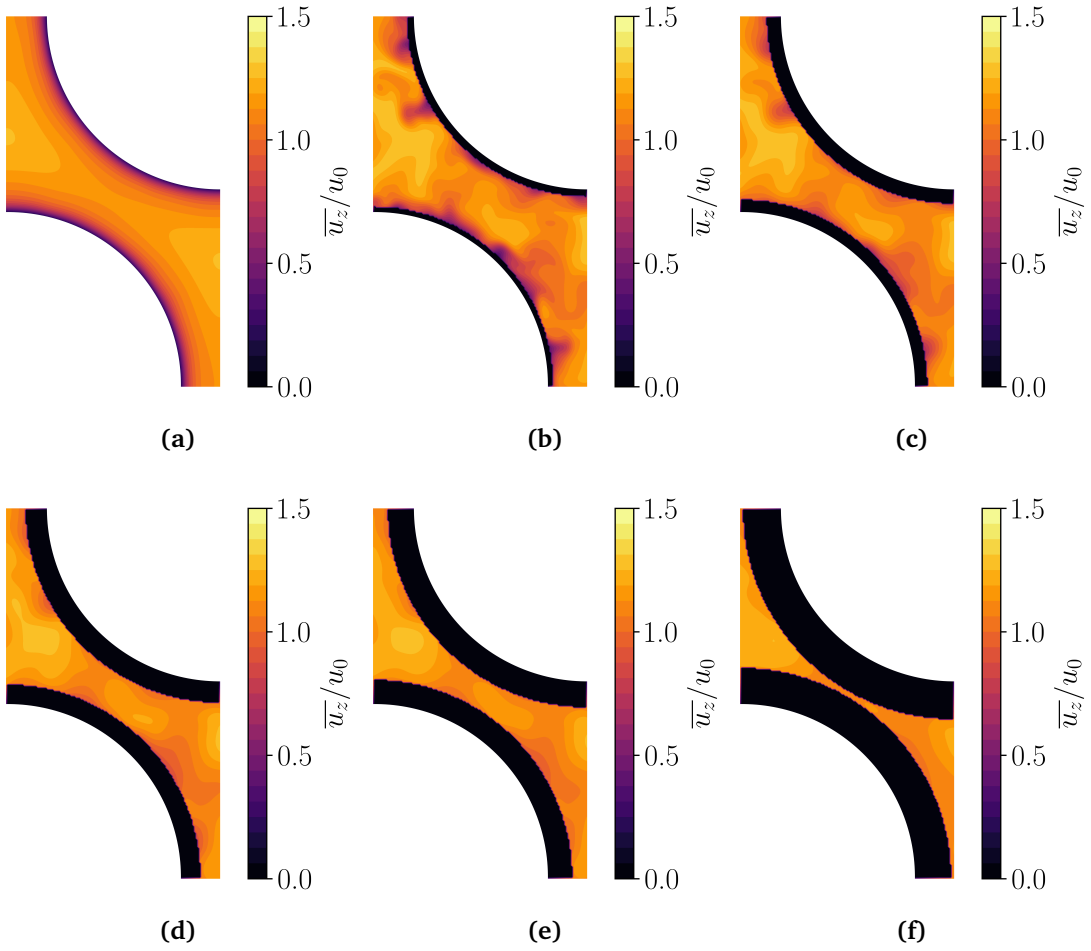

Figure 6.3: Streamwise velocity $\tilde{u}_z$ contours for: (a) DNS, (b) $f_{coars} = 2$, (c) $f_{coars} = 5$, (d) $f_{coars} = 8$, (e) $f_{coars} = 10$, (f) $f_{coars} = 15$

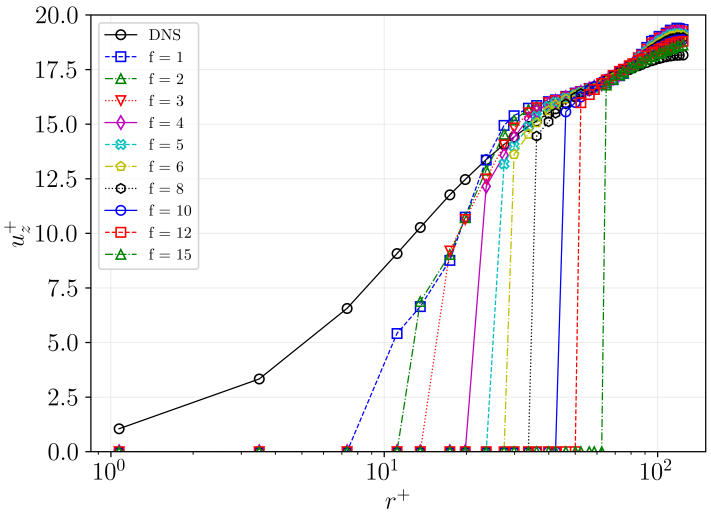

Figure 6.4: Profiles of $\widetilde{u_z^+}$ for different coarsening factors f_{coars}

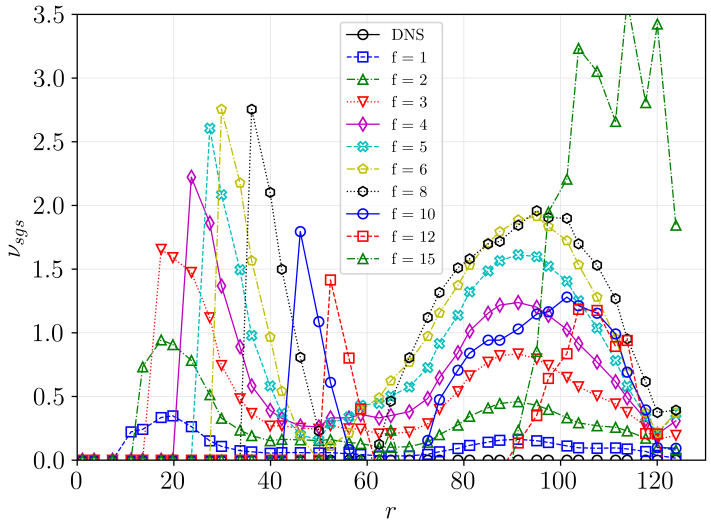

Figure 6.5: Profiles of ν_{sg}^{target} for different coarsening factors f_{coars}

where ν_{sg}^{Smag} is the eddy-viscosity described in the Smagorinsky model, with:

$$\nu_{sg}^{Smag} = (C_s\Delta)^2\sqrt{2\tilde{S}_{ij}\tilde{S}_{ij}} \tag{6.12}$$

$$C_s = 0.15 \tag{6.13}$$

$$\Delta = 2f_{coars}\sqrt[3]{\Delta_x\Delta_y\Delta_z} \tag{6.14}$$

6.2. Artificial Neural Network training

The eddy viscosity correction α is defined as a functional relationship of flow and simulation parameters as:

$$\alpha = f(\tilde{S}, \tilde{\Omega}, \tilde{k}, \tilde{\omega}, \Delta, d, \nu) \tag{6.15}$$

where $\tilde{S}$ is the strain tensor as defined in Equation 6.8, Δ is the cell size as in Equation 6.14, d is the distance from the wall boundaries, ν is the visosity. The vorticity tensor $\tilde{\Omega}$, the turbulent kinetic energy $\tilde{k}$ and the dissipation rate $\tilde{\omega}$ are defined as:

$$\tilde{\Omega}_{ij} = \frac{1}{2}\left(\partial_j\tilde{u}_i - \partial_i\tilde{u}_j\right) \tag{6.16}$$

$$\tilde{k} = \frac{1}{2}\overline{\tilde{u}_i'\tilde{u}_i'} \tag{6.17}$$

$$\tilde{\omega} = \frac{\tilde{\varepsilon}}{\tilde{k}0.09} = \nu\frac{\overline{\partial_k\tilde{u}_i'\partial_k\tilde{u}_i'}}{0.18\overline{\tilde{u}_i'\tilde{u}_i'}} \tag{6.18}$$

A dimensional analysis employing the Buckingham Pi theorem [141] resulted in

the definition of eight non-dimensional numbers:

$$\begin{aligned}
\pi_1 &= \left(\frac{1}{\tilde{\omega}}\right)^2 \{\tilde{S}^2\}, & \pi_2 &= \left(\frac{1}{\tilde{\omega}}\right)^2 \{\tilde{\Omega}^2\} \\
\pi_3 &= \left(\frac{1}{\tilde{\omega}}\right)^3 \{\tilde{S}^3\}, & \pi_4 &= \left(\frac{1}{\tilde{\omega}}\right)^3 \{\tilde{\Omega}^2\tilde{S}\} \\
\pi_5 &= \left(\frac{1}{\tilde{\omega}}\right)^4 \{\tilde{\Omega}^2\tilde{S}^2\}, & \pi_6 &= \frac{\tilde{k}}{\tilde{\omega}\,\nu} \\
\pi_7 &= \sqrt{\tilde{k}}\,\frac{\bar{\Delta}}{\nu}, & \pi_8 &= \sqrt{\tilde{k}}\,\frac{d}{\nu}
\end{aligned} \tag{6.19}$$

Equation 6.15 then becomes:

$$\alpha = g(\pi_1, ..., \pi_8) \tag{6.20}$$

The model employed in the following was developed by *von Karman Institute for Fluid Dynamics* and presented at the 1st European Fluid Dynamics Conference in Aachen (2024) under the title "*Data-driven scale-adaptive turbulence closure modelling*" [142]. It is therefore recommended that readers refer to the aforementioned source for a comprehensive overview of the architectural design of the model.

The Artificial Neural Network (ANN) has been trained on flow around rod bundle with $\mathrm{Re}_\tau = 400$ and different grid resolution by changing the coarsening factor f_{coars}. The data used is only a part (1/10) of the computational domain in z of the original case to mitigate the computational time associated to the training phase. However, the ANN approach is advantageous because it allows for the resumption of model training allowing more data to be used at later stage to reinforce the prediction capabilities.

The training process is tracked by examining the evolution of the training loss and by evaluating how well the predictions matched the targets on the validation sets. As shown in Figure 6.6, the training error displays a slightly oscillatory pattern. Nevertheless, the validation error reaches a plateau after approximately 50 iterations. Monitoring the model's performance on the validation sets made it pos-

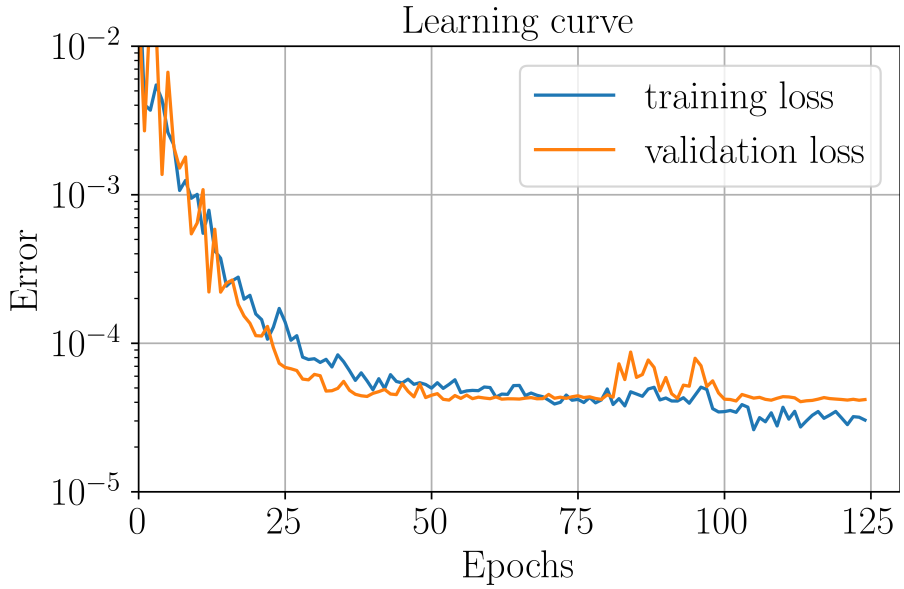

(a)

Figure 6.6: Evolution of the loss function evaluated on training and validation sets

sible to identify an optimal convergence point at around 60 iterations.

The a-priori validation process involves the estimation of the model's performance on data that was not observed during the validation phase. The contours in Figure 6.7 point out that is able to capture the overall shape and order of magnitude of the target eddy viscosity. The network appears to be resilient to the truncation of the training data in the vicinity of the wall and is capable of reproducing the subgrid viscosity gradients even better in this region with respect to the center of the channel, where the model underpredicts the target value.

The model can definitely be improved in several areas. A primary step in this process shall be enlarging the data network utilised for the training of the model. It is noteworthy that thus far, a single time step has been employed, derived from the DNS simulation; however, in order to improve the quality of the model's predictions, it would be advisable to utilise additional time steps, in conjunction with an extension of the data sampled in the z-direction. Another point of considerable importance is the nature of the inputs π_i: the inputs used so far are based on quanti-

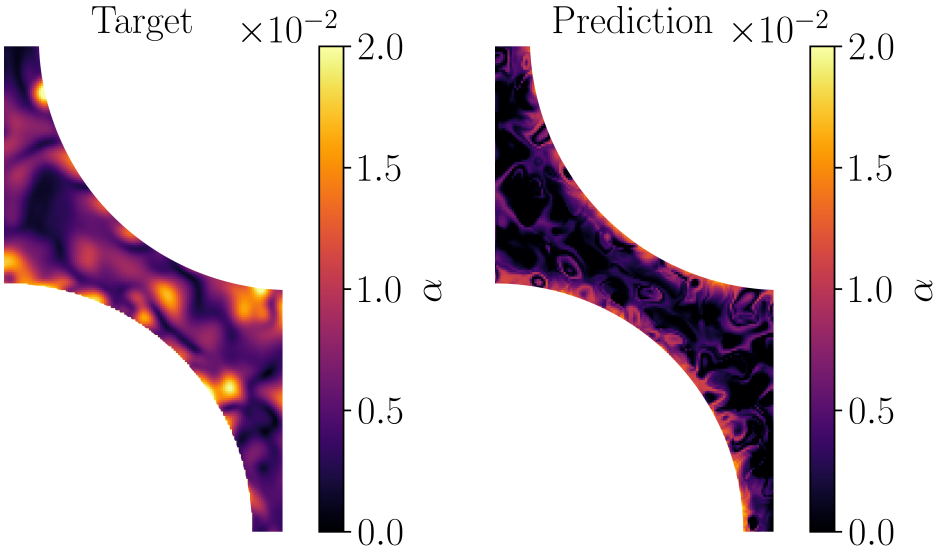

(a) **(b)**

Figure 6.7: (a) Target and (b) model prediction of α for $f_{coars} = 4$.

ties that adequately represent a $k-\omega$ SST model. However, given that in the case in question α is defined on the basis of the eddy-viscosity as in the Smagorinsky model, it would be useful to understand whether there are any inputs to be provided to the model that could better describe the behaviour of the fluid in case this application will be used for LES. The results obtained, although apparently positive, are therefore to be considered purely preliminary and require further in-depth investigation and validation.

Chapter 7

Conclusions

The aim of this research was to investigate the flow behaviour around rod bundles characterised by a low Prandtl number. This particular type of study is of significant interest in the context of the design of new IV generation nuclear reactors, which will adopt new refrigerant fluids (such as liquid metals) that require updated studies.

As demonstrated in Chapter 2, the existing literature indicates that the characterisation of flow around rod bundles has historically been a subject of interest for a variety of engineering applications. Indeed, a considerable number of correlations exist for the evaluation of the friction factor or the Nusselt number in specific configurations. Existing correlations are frequently founded upon very early experiments conducted in a limited range of geometric and thermo hydraulic configurations. Consequently, they often fall short in accurately depicting behaviour in innovative applications. In this regard, CFD emerges as a valuable investigative instrument, with numerous examples illustrating its efficacy. These include the development of high-fidelity data through DNS simulations and the successful application of LES and RANS models in complex geometries.However, upon consideration of the objective of this thesis and a focus on fluids with low Prandtl numbers, it becomes evident that certain critical issues arise for flows around rod bundles. Specifically, the nature of the fluid, which no longer complies with the so-called *Reynolds analogy*, results in

many turbulence models failing to accurately predict the behaviour of the fluid. In light of these challenges, novel models are currently being developed and validated. Nevertheless, the validation of these models is conditional upon the availability of high-fidelity datasets for low Prandtl number fluids under transient conditions, typical of IV-gen nuclear reactors. It is within this paradigm that the present work is situated.

The first part of this study in Chapter 4 investigated the effects that buoyancy can have on a weakly turbulent flow around a square-arranged bundle of heated rods, cooled by Liquid Lead-Bismuth Eutectic (LBE) at $Pr = 0.031$. Four different simulations are performed for forced ($Ri = 0$) and mixed convection conditions ($Ri = 0.025, 0.24, 0.75$). Statistics show that at these Reynolds numbers values the effect of buoyancy can be appreciated by looking at the average velocity profile (especially cross-flow components), but even more so by focusing on the fluctuations related to turbulent kinetic energy. Moreover, the effects on the mean temperature fields is almost negligible. The Nusselt number reveals a slight deterioration of the heat transfer rate for $Ri = 0.24$ and an increase of its value for the mixed convection case for $Ri = 0.75$. One of the most interesting aspects emerging from this analysis is that for the case $Ri = 0.75$, which is characterised by a lower Reynolds number than the other cases, heat exchange appears to occur more efficiently. From the analysis of both velocity profiles and turbulent budgets, it appears that this is due to a particular flow configuration under these conditions, which presents velocity derivatives that change sign and is strongly influenced by the presence of buoyancy.

In Chapter 5 the results of a benchmark exercise proposed by EGTHM are reported. The numerical case is a semplification of an existing experimental domain and it is constituted by turbulent flow around rod bundles arranged in a triangular lattice. The objective of the benchmark is to analyse the effects that the presence of spacer grids has on the flow around rod bundles. DNS simulations have the capacity to contribute to the scientific understanding of the phenomenon by providing a high-fidelity dataset in the absence of the grid. This additional dataset offers benchmark participants a point of comparison that extends beyond the experimental data alone. The data obtained are consistent with the experimental results and also pro-

vide information on thermal aspects, as the simulation was conducted using heated rod bundles surrounded by a fluid representative of liquid metal.

The creation of these datasets, however, is not an end in itself. Chapter 6 highlights how these data can be used to develop new turbulence models. During my period abroad at *von Karman Institute for Fluid Dynamics* (Sint-Genesius-Rode, Belgium), by employing an Artificial Neural Network, the first training phase of a predictive model for a corrective factor of sub-grid eddy viscosity, as present in commonly used turbulence models, has been initiated. Using the available DNS data from Chapter 5, it was possible to apply filtering to generate LES data at various filtering levels, which were then used to train the model. The model seems to predict the behaviour of the sub-grid eddy viscosity near the bundles fairly accurately, while further validation and training dataset are needed to better describe the behaviour of the flow deeper at the center of the subchannels.

Whilst the preceding literature review identified certain gaps in the characterisation of fluids surrounding rod bundles, this study indicates that CFD is a highly effective investigative tool in critical areas of the research field. In particular, DNS calculations, as employed in the present study, despite their limitations in terms of high computational cost and simplified domains, provide high-fidelity data that can most accurately capture the thermo hydraulic behaviour of the fluid under specific operating conditions, where both common turbulence models and experimental tests may face challenges. Consequently, the approach presented in this work offers a valuable tool for investigating the thermo-fluid dynamic behaviour of liquid metals around rod bundles, particularly in the context of low Reynolds number regimes and mixed convection conditions. The generation of new high-fidelity datasets through CFD is of considerable importance for the development of new, more reliable turbulence models. The data presented in this work could be made available in the future upon request for model validation, or new investigations could be conducted based on requests from the community.

CHAPTER 8

Appendix: Derivation of turbulent budgets

8.1. Equations

As seen in Chapter 3, the continuity equation for the case under analysis is:

$$\frac{\partial u_i}{\partial x_i} = 0 \tag{8.1}$$

The momentum equation can be written as:

$$\rho\left(\frac{\partial u_i}{\partial t} + u_j\frac{\partial u_i}{\partial x_j}\right) = -\frac{\partial p}{\partial x_i} + \mu\frac{\partial^2 u_i}{\partial x_j \partial x_j} + \rho g_i \tag{8.2}$$

By applying the definition for p_m, the form of the momentum equations to be solved is then:

$$\rho\left(\frac{\partial u_i}{\partial t} + u_j\frac{\partial u_i}{\partial x_j}\right) = -\frac{\partial p'_m}{\partial x_i} + \mu\frac{\partial^2 u_i}{\partial x_j \partial x_j} + (\rho g\beta\theta + \sigma)\delta_{i3} \tag{8.3}$$

As for the energy equation, the followig expression can be considered:

$$\rho c_p\left(\frac{\partial \theta}{\partial t} + u_i\frac{\partial \theta}{\partial x_i}\right) = \lambda\frac{\partial^2 \theta}{\partial x_i \partial x_i} - \rho c_p a u_3 \tag{8.4}$$

8.2. Turbulent kinetic energy budget

To obatain the transport equation for the turbulent kinetic energy, the momentum equation as to be taken into account (8.3). The equation is written using the Reynolds decomposition:

$$\rho\left[\frac{\partial(\overline{u_i}+u_i')}{\partial t}+(\overline{u_j}+u_j')\frac{\partial(\overline{u_i}+u_i')}{\partial x_j}\right]=-\frac{\partial(\overline{p_m}+p_m')}{\partial x_i}+\mu\frac{\partial^2(\overline{u_i}+u_i')}{\partial x_j\partial x_j}+\Big[\rho g\beta(\overline{\theta}+\theta')+\sigma\Big]\delta_{i3} \tag{8.5}$$

The Reynolds Average Equation obtained from (8.2):

$$\rho\left[\frac{\partial\overline{u_i}}{\partial t}+\overline{u_j}\frac{\partial\overline{u_i}}{\partial x_j}+\overline{u_j'\frac{\partial u_i'}{\partial x_j}}\right]=-\frac{\partial\overline{p_m}}{\partial x_i}\mu\frac{\partial^2\overline{u_i}}{\partial x_j\partial x_j}+\left(\rho g\beta\overline{\theta}\right)\delta_{i3} \tag{8.6}$$

The following is obtained by subtracting (8.5) - (8.6):

$$\begin{aligned}\rho\left[\frac{\partial u_i'}{\partial t}+u_j'\frac{\partial\overline{u_i}}{\partial x_j}+u_j'\frac{\partial u_i'}{\partial x_j}-\overline{u_j'\frac{\partial u_i'}{\partial x_j}}+\overline{u_j}\frac{\partial u_i'}{\partial x_j}\right]=\\ -\frac{\partial p_m'}{\partial x_i}+\mu\frac{\partial^2 u_i'}{\partial x_j\partial x_j}+\left(\rho g\beta\theta'\right)\delta_{i3}\end{aligned} \tag{8.7}$$

The equation (8.7) is multiplied by u_k'

$$\begin{aligned}\rho\left[u_k'\frac{\partial u_i'}{\partial t}+u_j'u_k'\frac{\partial\overline{u_i}}{\partial x_j}+u_j'u_k'\frac{\partial u_i'}{\partial x_j}-u_k'\overline{u_j'\frac{\partial u_i'}{\partial x_j}}+\overline{u_j}u_k'\frac{\partial u_i'}{\partial x_j}\right]=\\ -u_k'\frac{\partial p_m'}{\partial x_i}+\mu u_k'\frac{\partial^2 u_i'}{\partial x_j\partial x_j}+\left(\rho g\beta u_k'\theta'\right)\delta_{i3}\end{aligned} \tag{8.8}$$

and then averaged. With a proper reorganisation of the terms, it becomes:

$$\begin{aligned}\rho\left[\overline{u_k'\frac{\partial u_i'}{\partial t}}+\overline{u_j'u_k'\frac{\partial\overline{u_i}}{\partial x_j}}+\overline{u_j'u_k'\frac{\partial u_i'}{\partial x_j}}+U_j\overline{u_k'\frac{\partial u_i'}{\partial x_j}}\right]=\\ -\overline{u_k'\frac{\partial p_m'}{\partial x_i}}+\mu\overline{u_k'\frac{\partial^2 u_i'}{\partial x_j\partial x_j}}+\left(\rho g\beta\overline{u_k'\theta'}\right)\delta_{i3}\end{aligned} \tag{8.9}$$

The indices i and k of equation (8.9) are swapped, obtaining:

$$\begin{aligned}\rho\left[\overline{u_i'\frac{\partial u_k'}{\partial t}}+\overline{u_j'u_i'\frac{\partial \overline{u_k}}{\partial x_j}}+\overline{u_j'u_i'\frac{\partial u_k'}{\partial x_j}}+\overline{u_j}\,\overline{u_i'\frac{\partial u_k'}{\partial x_j}}\right]=\\ \overline{-u_i'\frac{\partial p_m'}{\partial x_k}}+\mu\overline{u_i'\frac{\partial^2 u_k'}{\partial x_j\partial x_j}}+\left(\rho g\beta\overline{u_i'\theta'}\right)\delta_{i3}\end{aligned} \tag{8.10}$$

The equations (8.9) and (8.10) are now summed:

$$\begin{aligned}&\underbrace{\rho\left(\overline{u_k'\frac{\partial u_i'}{\partial t}}+\overline{u_i'\frac{\partial u_k'}{\partial t}}\right)}_{\text{I}}+\underbrace{\rho\overline{u_j}\left(\overline{u_k'\frac{\partial u_i'}{\partial x_j}}+\overline{u_i'\frac{\partial u_k'}{\partial x_j}}\right)}_{\text{II}}\\ &=\underbrace{-\left(\overline{u_k'\frac{\partial p_m'}{\partial x_i}}+\overline{u_i'\frac{\partial p_m'}{\partial x_k}}\right)}_{\text{III}}\underbrace{-\rho\left(\overline{u_j'u_k'\frac{\partial u_i'}{\partial x_j}}+\overline{u_j'u_i'\frac{\partial u_k'}{\partial x_j}}\right)}_{\text{IV}}+\underbrace{\mu\left(\overline{u_k'\frac{\partial^2 u_i'}{\partial x_j\partial x_j}}+\overline{u_i'\frac{\partial^2 u_k'}{\partial x_j\partial x_j}}\right)}_{\text{V}}\\ &\underbrace{-\rho\left(\overline{u_j'u_k'\frac{\partial \overline{u_i}}{\partial x_j}}+\overline{u_j'u_i'\frac{\partial \overline{u_k}}{\partial x_j}}\right)}_{\text{VI}}+\underbrace{\left[\rho g\beta\left(\overline{u_k'\theta'}+\overline{u_i'\theta'}\right)\right]\delta_{i3}}_{\text{VII}}\end{aligned} \tag{8.11}$$

obtaining the Reynolds-stress equation.

However, some terms can be rewritten to better intepret the equation. Considering term III:

$$-\left(\overline{u_k'\frac{\partial p_m'}{\partial x_i}}+\overline{u_i'\frac{\partial p_m'}{\partial x_k}}\right)=-\left[\overline{-p_m'\left(\frac{\partial u_i'}{\partial x_k}+\frac{\partial u_k'}{\partial x_i}\right)}+\frac{\partial}{\partial x_j}\left(\overline{p_m'u_i'}\,\delta_{kj}+\overline{p_m'u_k'}\,\delta_{ij}\right)\right] \tag{8.12}$$

Term IV can be also rearranged as:

$$-\rho\left(\overline{u_j'u_k'\frac{\partial u_i'}{\partial x_j}}+\overline{u_j'u_i'\frac{\partial u_k'}{\partial x_j}}\right)=-\rho\frac{\partial}{\partial x_j}\overline{u_i'u_j'u_k'} \tag{8.13}$$

For term V it can obtained:

$$\mu\left(\overline{u'_k\frac{\partial^2 u'_i}{\partial x_j\partial x_j}}+\overline{u'_i\frac{\partial^2 u'_k}{\partial x_j\partial x_j}}\right)=\mu\left[-\left(\overline{\frac{\partial u'_k}{\partial x_j}\frac{\partial u'_i}{\partial x_j}}+\overline{\frac{\partial u'_i}{\partial x_j}\frac{\partial u'_k}{\partial x_j}}\right)+\frac{\partial}{\partial x_j}\left(\overline{u'_i\frac{\partial u'_k}{\partial x_j}}+\overline{u'_k\frac{\partial u'_i}{\partial x_j}}\right)\right] \tag{8.14}$$

After these term modifications, the Reynolds-stress equation 8.11 becomes:

$$\begin{aligned}&\rho\left(\overline{u'_k\frac{\partial u'_i}{\partial t}}+\overline{u'_i\frac{\partial u'_k}{\partial t}}\right)+\rho\overline{u_j}\left(\overline{u'_k\frac{\partial u'_i}{\partial x_j}}+\overline{u'_i\frac{\partial u'_k}{\partial x_j}}\right)\\&=\overline{p'_m\left(\frac{\partial u'_i}{\partial x_k}+\frac{\partial u'_k}{\partial x_i}\right)}+\frac{\partial}{\partial x_j}\left[-\left(\overline{p'_m u'_i}\,\delta_{kj}+\overline{p'_m u'_k}\,\delta_{ij}\right)-\rho\overline{u'_i u'_j u'_k}+\mu\left(\overline{u'_k\frac{\partial u'_i}{\partial x_j}}+\overline{u'_i\frac{\partial u'_k}{\partial x_j}}\right)\right]\\&\quad-\rho\left(\overline{u'_j u'_k\frac{\partial\overline{u_i}}{\partial x_j}}+\overline{u'_j u'_i\frac{\partial\overline{u_k}}{\partial x_j}}\right)-\mu\left(\overline{\frac{\partial u'_k}{\partial x_j}\frac{\partial u'_i}{\partial x_j}}+\overline{\frac{\partial u'_i}{\partial x_j}\frac{\partial u'_k}{\partial x_j}}\right)+\rho g\beta\left(\overline{u'_k\theta'}+\overline{u'_i\theta'}\right)\delta_{i3}\end{aligned} \tag{8.15}$$

which, in its dimensionless form, becomes:

$$\begin{aligned}&\left(\overline{u'_k\frac{\partial u'_i}{\partial t}}+\overline{u'_i\frac{\partial u'_k}{\partial t}}\right)+\overline{u_j}\left(\overline{u'_k\frac{\partial u'_i}{\partial x_j}}+\overline{u'_i\frac{\partial u'_k}{\partial x_j}}\right)\\&=\overline{p'_m\left(\frac{\partial u'_i}{\partial x_k}+\frac{\partial u'_k}{\partial x_i}\right)}+\frac{\partial}{\partial x_j}\left[-\left(\overline{p'_m u'_i}\,\delta_{kj}+\overline{p'_m u'_k}\,\delta_{ij}\right)-\rho\overline{u'_i u'_j u'_k}+\frac{1}{Re_\tau}\left(\overline{u'_k\frac{\partial u'_i}{\partial x_j}}+\overline{u'_i\frac{\partial u'_k}{\partial x_j}}\right)\right]\\&\quad-\rho\left(\overline{u'_j u'_k\frac{\partial\overline{u_i}}{\partial x_j}}+\overline{u'_j u'_i\frac{\partial\overline{u_k}}{\partial x_j}}\right)-\frac{1}{Re_\tau}\left(\overline{\frac{\partial u'_k}{\partial x_j}\frac{\partial u'_i}{\partial x_j}}+\overline{\frac{\partial u'_i}{\partial x_j}\frac{\partial u'_k}{\partial x_j}}\right)+\frac{Gr}{Re_\tau^2}\left(\overline{u'_k\theta'}+\overline{u'_i\theta'}\right)\delta_{i3}\end{aligned} \tag{8.16}$$

From the Reynolds-stress equation 8.16, contracting the free indice ($k\rightarrow i$) and dividing by 2, the turbulent kinetic energy (TKE) budget equation is finally obtained:

$$\frac{\partial k}{\partial t}=P_{ii}+C_{ii}+T_{ii}+\Pi_{ii}+D_{ii}+\varepsilon_{ii}+B_{ii} \tag{8.17}$$

where

$$P_{ii} = -\overline{u_i' u_j'} \frac{\partial \overline{u_i}}{\partial x_j},\ C_{ii} = -\overline{u_j} \frac{1}{2} \frac{\partial \overline{u_i' u_i'}}{\partial x_j},\ T_{ii} = -\frac{1}{2} \frac{\partial \overline{u_i' u_i' u_j'}}{\partial x_j},\ \Pi_{ii} = -\frac{\partial \overline{p_m' u_i'}}{\partial x_j} \delta_{ij}$$
$$D_{ii} = \frac{1}{\mathrm{Re}_\tau} \frac{\partial}{\partial x_j} \left(\overline{u_i' \frac{\partial u_i'}{\partial x_j}} \right),\ \varepsilon_{ii} = -\frac{1}{\mathrm{Re}_\tau} \overline{\frac{\partial u_i'}{\partial x_j} \frac{\partial u_i'}{\partial x_j}},\ B_{ii} = \frac{\mathrm{Gr}}{\mathrm{Re}_\tau^2} \overline{\theta' u_i'} \delta_{i3} \tag{8.18}$$

8.3. Turbulent heat fluxes budget

To write the transport equation of turbulent heat flux $-\overline{u_j' \theta'}$, the following observation can be stated:

$$\frac{\partial u_j' \theta'}{\partial t} = \theta' \frac{\partial u_j'}{\partial t} + u_j' \frac{\partial \theta'}{\partial t} \tag{8.19}$$

To obtain an expression for what is written above in Eq. 8.19, it is necessary to repeat the previous steps taken for the momentum equation also for the energy equation, to obtain an expression similar to 8.7. From the energy equation 8.4 it can be obtained:

$$\rho c_p \frac{\partial \theta'}{\partial t} + \rho c_p \overline{u_i} \frac{\partial \theta'}{\partial x_i} + \rho c_p u_i' \frac{\partial \overline{\theta}}{\partial x_i} + \rho c_p u_i' \frac{\partial \theta'}{\partial x_i} - \rho c_p \overline{u_i' \frac{\partial \theta'}{\partial x_i}} = \lambda \frac{\partial^2 \theta'}{\partial x_i \partial x_i} - \rho c_p a u_3' \tag{8.20}$$

By multiplying Eq. 8.7 by θ' and Eq. 8.20 by u_i', from 8.19 it can be derived:

$$\mu \left(\overline{u_k' \frac{\partial^2 u_i'}{\partial x_j \partial x_j}} + \overline{u_i' \frac{\partial^2 u_k'}{\partial x_j \partial x_j}} \right) = \mu \Bigg[-\left(\overline{\frac{\partial u_k'}{\partial x_j} \frac{\partial u_i'}{\partial x_j}} + \overline{\frac{\partial u_i'}{\partial x_j} \frac{\partial u_k'}{\partial x_j}} \right) + \frac{\partial}{\partial x_j} \left(\overline{u_i' \frac{\partial u_k'}{\partial x_j}} + \overline{u_k' \frac{\partial u_i'}{\partial x_j}} \right) \Bigg] \tag{8.21}$$

Eq. 8.21 is then averaged, resulting in:

$$\begin{aligned}\rho\frac{\partial\overline{u_i'\theta'}}{\partial t}&+\rho\Big(\overline{\theta'u_j'}\frac{\partial\overline{u_i}}{\partial x_j}+\overline{\theta'u_j'\frac{\partial u_i'}{\partial x_j}}+\overline{u_j}\,\overline{\theta'\frac{\partial u_i'}{\partial x_j}}\Big)\\&+\rho c_p\Big(\overline{u_j}\,\overline{u_i'\frac{\partial\theta'}{\partial x_j}}+\overline{u_i'u_j'}\frac{\partial\overline{\theta}}{\partial x_j}+\overline{u_i'u_j'\frac{\partial\theta'}{\partial x_j}}\Big)\\&=\mu\overline{\theta'\frac{\partial^2u_i'}{\partial x_j\partial x_j}}+\lambda\overline{u_i'\frac{\partial^2\theta'}{\partial x_j\partial x_j}}+\rho g\beta\overline{\theta'\theta'}-\rho c_p a\overline{u_i'u_3'}\end{aligned}\tag{8.22}$$

Eq. 8.22 can be rearranged and expressed in its dimensionless form for $i=3$. This results in the following turbulent heat flux budget equation for $\overline{u_z'\theta'}$:

$$\frac{\partial\overline{u_z'\theta'}}{\partial t}=P_{3\theta}+C_{3\theta}+\Phi_{3\theta}+T_{3\theta}+\Pi_{3\theta}+D_{3\theta}+\varepsilon_{3\theta}+B_{3\theta}\tag{8.23}$$

with

$$\begin{aligned}&P_{3\theta}=-\left(\overline{\theta'u_j'}\frac{\partial\overline{u_z}}{\partial x_j}+\overline{u_z'u_j'}\frac{\partial\overline{\theta}}{\partial x_j}\right),\ C_{3\theta}=-\overline{u_j}\frac{\partial\overline{u_z'\theta'}}{\partial x_j},\ \Phi_{3\theta}=\overline{p_m'\frac{\partial\theta'}{\partial z}},\\&T_{3\theta}=-\frac{\partial\overline{u_j'u_z'\theta'}}{\partial x_j},\ \Pi_{3\theta}=-\frac{\partial\overline{\theta'p_m'}}{\partial z},\ D_{3\theta}=\frac{1}{\mathrm{Re}_\tau}\frac{\partial}{\partial x_j}\left(\overline{\theta'\frac{\partial u_z'}{\partial x_j}}+\frac{1}{\mathrm{Pr}}\overline{u_z'\frac{\partial\theta'}{\partial x_j}}\right),\\&\varepsilon_{3\theta}=-\left(\frac{1}{\mathrm{Re}_\tau}+\frac{1}{\mathrm{Re}_\tau\mathrm{Pr}}\right)\overline{\frac{\partial u_z'\partial\theta'}{\partial x_j\partial x_j}},\ B_{3\theta}=\frac{\mathrm{Gr}}{\mathrm{Re}_\tau^2}\overline{\theta'\theta'}+\frac{\omega}{\Omega}\frac{1}{\mathrm{RePr}}\overline{u_z'u_z'}\end{aligned}\tag{8.24}$$

List of Figures

List of Tables

Bibliography

[1] F. Roelofs. Introduction to liquid metal cooled reactors. In *Thermal Hydraulics Aspects of Liquid Metal Cooled Nuclear Reactors*. Woodhead Publishing / Elsevier, Duxford, UK, 2018.

[2] G. Grötzbach. Challenges in low-prandtl number heat transfer simulation and modelling. *Nuclear Engineering and Design*, 264:41–55, 2013.

[3] D. Angeli and E. Stalio. A fast algorithm for direct numerical simulation of turbulent convection with immersed boundaries. *Computers and Fluids*, 183:148–159, 2019.

[4] OECD/NEA. Lead-cooled fast reactor (lfr) benchmark.

[5] C. Menezes, T. Melsheimer, and Y.A. Hassan. Flow field characteristics of a 127-pin rod bundle with hexagonal spacer grids. *Physics of Fluids*, 35:067119, 2023.

[6] IAEA. Status of fast reactor research and technology development. Technical Report Technical Report 474, International Atomic Energy Agency, Vienna, Austria, 2012.

[7] IAEA. Status of innovative fast reactor designs and concepts. Technical report, International Atomic Energy Agency, Vienna, Austria, 2013.

[8] I. Pioro. *Handbook of Generation IV Nuclear Reactors*. Number 103 in Woodhead Publishing Series in Energy. Woodhead Publishing, Duxford, UK, 2016.

[9] GIF. A technology roadmap for generation iv nuclear energy systems. Technical Report GIF-002-00, Generation IV International Forum, USA, 2002.

[10] GIF. Technology roadmap update for generation iv nuclear energy systems. Technical report, Generation IV International Forum, Paris, France, 2014.

[11] OECD. Handbook on lead-bismuth eutectic alloy and lead properties, materials compatibility, thermal-hydraulics and technologies. Technical report, OECD Nuclear Energy Agency, Paris, France, 2015.

[12] N. Forgione, D. Castelliti, A. Gerschenfeld, M. Polidori, A.D. Nevo, and R. Hu. System thermal hydraulics for liquid metals. In F. Roelofs, editor, *Thermal Hydraulics Aspects of Liquid Metal Cooled Nuclear Reactors*, pages 157–184. WP – Woodhead Publishing, Duxford, UK, 2018.

[13] F. Roelofs, A. Shams, I. Otic, M. Böttcher, M. Duponcheel, Y. Bartosiewicz, D. Lakehal, E. Baglietto, S. Lardeau, and X. Cheng. Status and perspective of turbulence heat transfer modelling for the industrial application of liquid metal flows. *Nuclear Engineering and Design*, 290:99–106, 2015a.

[14] A. Shams, F. Roelofs, E. Baglietto, S. Lardeau, and S. Kenjeres. Assessment and calibration of an algebraic turbulent heat flux model for low-prandtl fluids. *International Journal of Heat and Mass Transfer*, 79:589–601, 2014.

[15] A. Shams. Assessment and calibration of an algebraic turbulent heat flux model for high rayleigh number flow regimes. In *Proceedings of ERMSAR-2017*, Warsaw, Poland, 2017.

[16] S. Manservisi and F. Menghini. Triangular rod bundle simulations of a cfd κ-ε-κ_θ-ε_θ heat transfer turbulence model for heavy liquid metals. *Nuclear Engineering and Design*, 273:251–270, 2014.

[17] S. Manservisi and F. Menghini. Cfd simulations in heavy liquid metal flows for square lattice bare rod bundle geometries with a four-parameter heat transfer turbulence model. *Nuclear Engineering and Design*, 295:251–260, 2015.

[18] X. Cheng. Subchannel analysis for lmr. In F. Roelofs, editor, *Thermal Hydraulics Aspects of Liquid Metal Cooled Nuclear Reactors*, pages 186–211. Woodhead Publishing / Elsevier, Duxford, UK, 2019.

[19] F. Roelofs, P. Planquart, and L. Koloszar. Best practice guidelines for nuclear liquid metal cfd. In F. Roelofs, editor, *Thermal Hydraulics Aspects of Liquid Metal Cooled Nuclear Reactors*, pages –. Woodhead Publishing / Elsevier, Duxford, UK, 2018.

[20] F. Roelofs, V.R. Gopala, S. Jayaraju, A. Shams, and E.M.J. Komen. Review of fuel assembly and pool thermal hydraulics for fast reactors. *Nuclear Engineering and Design*, 265:1205–1222, 2013.

[21] F. Menter, B. Hemstrom, M. Henriksson, R. Karlsson, A. Latrobe, A. Martin, P. Muhlbauer, M. Scheuerer, B. Smith, T. Takacs, and S. Willemsen. Cfd best practice guidelines for cfd code validation for reactor safety applications. Technical Report D01, ECORA, Germany, 2002.

[22] D. Bestion, A. Martin, F. Menter, M. Boucker, S. Pigny, M. Scheuerer, M. Heitsch, U. Rohde, S. Willemsen, H. Paillere, D. Sweet, and M. Andreani. Recommendation on use of cfd codes for nuclear reactor safety analysis. Technical Report D14, ECORA, France, 2004.

[23] R. Johnson, R. Schultz, P. Roache, I. Celik, W. Pointer, and Y. Hassan. Processes and procedures for application of cfd to nuclear reactor safety analysis. Technical Report INL/EXT-06-11789, Idaho National Laboratory, Idaho, USA, 2006.

[24] OECD. Best practice guidelines for the use of cfd in nuclear reactor safety applications. Technical Report NEA/CSNI/R(2007)5, OECD Nuclear Energy Agency, Paris, France, 2007.

[25] F. Roelofs. Thins wp3 cfd recommendations. Technical Report NRG-note 22622/10.103086, NRG, Petten, Netherlands, 2010.

[26] I. Tiselj, E. Stalio, D. Angeli, and J. Oder. Direct numerical simulations for liquid metal applications. In F. Roelofs, editor, *Thermal Hydraulics Aspects of Liquid Metal Cooled Nuclear Reactors*, pages 219–244. Woodhead Publishing / Elsevier, Duxford, UK, 2018.

[27] J. Kim and P. Moin. Transport of passive scalars in a turbulent channel flow. In *Turbulent Shear Flows VI*, page 85. Springer-Verlag, Berlin, 1989.

[28] N. Kasagi, Y. Tomita, and A. Kuroda. Direct numerical simulation of passive scalar field in a turbulent channel flow. *Journal of Heat Transfer, ASME*, 114:598–606, 1992.

[29] H. Kawamura, K. Ohsaka, H. Abe, and K. Yamamoto. Dns of turbulent heat transfer in channel flow with low to medium-high prandtl number fluid. *International Journal of Heat and Fluid Flow*, 19:482–491, 1998.

[30] Y. Na and T.J. Hanratty. Limiting behavior of turbulent scalar transport close to a wall. *International Journal of Heat and Mass Transfer*, 43:1749–1758, 2000.

[31] M. Piller, E. Nobile, and T.J. Hanratty. Dns study of turbulent transport at low prandtl numbers in a channel flow. *Journal of Fluid Mechanics*, 458:419–441, 2002.

[32] H. Abe, H. Kawamura, and Y. Matsuo. Surface heat-flux fluctuations in a turbulent channel flow up to $re_s = 1020$ with $pr = 0.025$ and 0.71. *International Journal of Heat and Fluid Flow*, 25:404–419, 2004.

[33] I. Tiselj and L. Cizelj. Dns of turbulent channel flow with conjugate heat transfer at prandtl number 0.01. *Nuclear Engineering and Design*, 253:153–160, 2012.

[34] H. Kawamura. Dns database. http://murasun.me.noda.tus.ac.jp/turbulence/poi/poi.html, 2017. Accessed January 2017.

[35] W. Guo and H. Prasser. Mixed convection study on the influence of low prandtl numbers and buoyancy in turbulent heat transfer using dns. *Annals of Nuclear Energy*, 158:108258, 2021.

[36] O. Errico and E. Stalio. Direct numerical simulation of turbulent forced convection in a wavy channel at low and order one prandtl number. *International Journal of Thermal Sciences*, 86:374–386, 2014.

[37] O. Errico and E. Stalio. Direct numerical simulation of low-prandtl number turbulent convection above a wavy wall. *Nuclear Engineering and Design*, 290:87–98, 2015.

[38] J. Oder, J. Urankar, and I. Tiselj. Spectral element direct numerical simulation of heat transfer in turbulent channel sodium flow. In *24th International Conference Nuclear Energy for New Europe*, Portoroz, Slovenia, 2015.

[39] J. Oder, A. Shams, L. Cizelj, and I. Tiselj. Direct numerical simulation of low-prandtl fluid flow over a confined backward facing step. *International Journal of Heat and Mass Transfer*, 142:118436, 2019.

[40] M. Niemann and J. Fröhlich. Turbulence budgets in buoyancy-affected vertical backward-facing step flow at low prandtl number. *Flow, Turbulence and Combustion*, 99:705–728, 2017.

[41] K. Rehme. *Handbook of single-phase convective heat-transfer*. A Wiley Inter science Publication, 1988.

[42] G. Grötzbach and M. Wörner. Direct numerical and large eddy simulations in nuclear applications. *International Journal of Heat and Fluid Flow*, 20:222–240, 1999.

[43] A. Kraus, E. Merzari, T. Norddine, O. Marin, and S. Benhamadouche. Direct numerical simulation of fluid flow in a 5x5 square rod bundle. *International Journal of Heat and Fluid Flow*, 90:108833, 2021.

[44] P. Fischer, J. Lottes, and H. Tufo. Nek5000, 2007. Computer software.

[45] S. Tavoularis. Rod bundle vortex networks, gap vortex streets, and gap instability: A nomenclature and some comments on available methodologies. *Nuclear Engineering and Design*, 241:2624–2626, 2011.

[46] E. Bubelis and M. Schikorr. Review and proposal for best fit of wire-wrapped fuel bundle friction factor and pressure drop predictions using various existing correlations. *Nuclear Engineering and Design*, 238:3299–3320, 2008.

[47] E. Novendstern. Turbulent flow pressure drop model for fuel rod assemblies utilizing a helical wire-wrap spacer system. *Nuclear Engineering and Design*, 22:19–27, 1972.

[48] K. Rehme. Pressure drop correlations for fuel element spacers. *Nuclear Technology*, 17:15–23, 1973.

[49] F. Engel, R. Markley, and A. Bishop. Laminar, transition and turbulent parallel flow pressure drop across wire-wrap-spaced rod bundles. *Nuclear Science and Engineering*, 69:290–296, 1979.

[50] S. Cheng and N. Todreas. Hydrodynamic models and correlations for bare wire-wrapped hexagonal rod bundles—bundle friction factors, sub-channel friction factors and mixing parameters. *Nuclear Engineering and Design*, 92:227–251, 1986.

[51] P. Press. *Heat Transfer and Fluid Flow in NuclearSystems*. Pergamon Press, 1981.

[52] V. Sobolev. Fuel rod and assembly proposal for xt-ads pre-design. *Coordination meeting of WP1 & WP2 of DM1 IP EUROTRANS*, 2006.

[53] D. Fan, T. Peng, Y. Tang, Q. Zhao, W. Tian, D. Liu, R. Li, D. Wang, and L. Gu. Periodicity and transversal pressure distribution in a wire-wrapped 19-pin fuel assembly. *International Journal of Energy Research*, 45:11837–11850, 2020.

[54] S. Cheng, Y. Cheng, and N. Todreas. The upgraded cheng and todreas correlation for pressure drop in hexagonal wire-wrapped rod bundles. *Nuclear Engineering and Design*, 335:356–373, 2014.

[55] P. Zhao, J. Liu, Z. Ge, X. Wang, and X. Cheng. Cfd analysis of transverse flow in a wire-wrapped hexagonal seven-pin bundle. *Nuclear Engineering and Design*, 317:146–157, 2017.

[56] OpenFOAM Foundation. Openfoam. https://www.openfoam.org. Open-source CFD software.

[57] J. Wantland. Orrible—a computer program for flow and temperature distribution in 19-rod lmfbr fuel subassemblies. *Nuclear Technology*, 24:168–175, 1974.

[58] M.N. Raj and K. Velusamy. Characterization of velocity and temperature fields in a 217 pin wire wrapped fuel bundle of sodium cooled fast reactor. *Annals of Nuclear Energy*, 87:331–349, 2016.

[59] S. Yoon and F. Heidet. Evaluation of pressure drop correlations for the wire-wrapped rod bundles. *Transactions of the American Nuclear Society, Virtual Conference*, 2020.

[60] A. Ahmad and K. Kim. Three-dimensional analysis of flow and heat transfer in a wire-wrapped fuel assembly. In *Proceeding of International Congress on Advances in Nuclear Power Plants (ICAPP)*, 2005.

[61] R. Gajapathy, K. Velusamy, P. Selvaraj, P. Chellapandi, and S. Chetal. Cfd investigation of helical wire-wrapped 7-pin fuel bundle and the challenges in modeling full scale 217 pin bundle. *Nuclear Engineering and Design*, 237:2332–2342, 2007.

[62] W.P. Jones and B.E. Launder. The prediction of laminarization with a two-equation model of turbulence. *International Journal of Heat and Mass Transfer*, 15(2):301–314, 1972.

[63] U. Bieder, H. Uitslag-Doolaard, and B. Mikuz. Investigation of pressure loss and velocity distribution in fuel assemblies with wire-wrapped rods by using rans and les with wall functions. *Annals of Nuclear Energy*, 152(108025), 2020.

[64] D. Dovizio, B. Mikuz, A. Shams, and F. Roelofs. Validating rans to predict the flow behavior in wire-wrapped fuel assemblies. *Nuclear Engineering and Design*, 356(110376), 2020.

[65] M. Song, J. Jeong, and E. Kim. Numerical investigation on vortex behavior in wire-wrapped fuel assembly for a sodium fast reactor. *Nuclear Engineering and Technology*, 51:665–675, 2019.

[66] F. Roelofs, H. Uitslag-Doolaard, B. Mikuž, D. Dovizio, D.D. Santis, A. Shams, F. Bertocchi, M. Rohde, K.V. Tichelen, S. Keijers, G. Kennedy, A. Batta, J. Pacio, P. Planquart, A. Obabko, L. Brockmeyer, E. Merzari, R. Vaghetto, Y. Hassan, D. Leonard, M. Martin, B. Jackson, M. Steer, M. Delchini, and W. Pointer. Cfd and experiments for wire-wrapped fuel assemblies. In *Proceedings of 18th International Topical Meeting on Nuclear Reactor Thermal Hydraulics (NURETH-18)*, 2019.

[67] M. Delchini, L. Swiler, E. Popov, and W. Pointer. An uncertainty quantification of the computational fluid dynamics solution to the modeling of the contact point in a wire-wrapped fuel assembly. *ANS Annual Meeting*, 2018.

[68] K. Katsuyama, T. Nagamine, S. Matsumoto, and M. Ito. Application of x-ray computer tomography for observing the deflection and displacement of fuel pins in an assembly irradiated in fbr. *Journal of Nuclear Science and Technology*, 40(4):220–226, 2003.

[69] V. Kriventsev. Thermal hydraulics of innovative nuclear energy systems. *Joint ICTP-IAEA Workshop on the Physics and Technology of Innovative Nuclear Energy Systems, Trieste, Italy*, 2018.

[70] B. Mays, R. Jackson, T. Reeves, and N. Salpeter. Experimental data sets for cfd calculations of flow and heat transfer in deformed fuel assemblies. volume 115, 2016.

[71] M. Nishimura, H. Sato, H. Kamide, H. Ohshima, K. Nagasawa, and Y. Imai. Investigation on velocity distribution around the wrapping wire in an inner subchannel of fuel pin bundle. 2012.

[72] E. Merzari, P. Fischer, H. Yuan, K.V. Tichelen, S. Keijers, J.D. Ridder, J. Degroote, J. Vierendeels, H. Doolaard, V. Gopala, and F. Roelofs. Benchmark exercise for fluid flow simulations in a liquid metal fastreactor fuel assembly. *Nuclear Engineering and Design*, 298:218–228, 2016.

[73] F. Bertocchi and M. Rohde. Preliminary design of mir facility. *SESAME Deliverable 2.1*, 2016.

[74] D. Dovizio, B. Mikuz, A. Shams, and F. Roelofs. Validating rans to predict the flow behaviour in wire-wrapped fuel assemblies. 2019.

[75] M. Chun and K. Seo. An experimental study and assessment of existing friction factor correlations for wire-wrapped fuel assemblies. *Annals of Nuclear Energy*, 28:1683–1695, 2001.

[76] J. Chen, D. Zhang, P. Song, X. Wang, S. Wang, Y. Liang, S.Q. S., Y. Zhang, M. Wang, and G. Su. Cfd investigation on thermal-hydraulic behaviors of a wire-wrapped fuel subassembly for sodium-cooled fast reactor. *Annals of Nuclear Energy*, 113:256–269, 2018.

[77] M. Berthoux and T. Cadiou. The thermal hydraulics in a rod bundle representative of the start-up core of the allegro gas cooled fast reactor—experimental and numerical approaches. *Nuclear Engineering and Design*, 240:3372–3386, 2010.

[78] I.D. Piazza, M. Angelucci, R. Marinari, M. Tarantino, and N. Forgione. Heat transfer on hlm cooled wire-spaced fuel pin bundle simulatorin the nacie-up facility. *Nuclear Engineering and Design*, 300:256–267, 2016.

[79] H. Doolaard, H. Bijleveld, V. Sanna, D. Rosa, and V. Gopala. Report on pre- and post-test analysis of the nacie and theades experimental loops and assessment of the 127 pin myrrha fa. search d2.8. 2015.

[80] J. Pacio, M. Daubner, F. Fellmoser, K. Litfin, and T. Wetzel. Experimental study of heavy-liquid metal (lbe) flow and heat transfer along a hexagonal 19-rod bundle with wire spacers. *Nuclear Engineering and Design*, 301:111–127, 2016.

[81] J. Pacio, T. Wetzel, and H.D.F. Roelofs. Thermal-hydraulic study of the lbe-cooled fuel assembly in the myrrha reactor: Experiments and simulations. *Nuclear Engineering and Design*, 312:327–337, 2017.

[82] T. Nguyen, N. Goth, P. Jones, R. Vaghetto, and Y. Hassan. Stereoscopic piv measurements of near-wall flow in a tightly packed rod bundle with wire spacers. *Experimental Thermal and Fluid Science*, 92:420–435, 2018.

[83] N. Goth, P. Jones, D. Nguyen, R. Vaghetto, Y. Hassan, A. Obabko, E. Merzari, and P. Fischer. Comparison of experimental and simulation results on interior subchannels of a 61-pin wire-wrapped hexagonal fuel bundle. *Nuclear Engineering and Design*, 338:130–136, 2018.

[84] B. Mays and R. Jackson. Thermal hydraulic computational fluid dynamics simulations and experimental investigation of deformed fuel assemblies. final report. 2017.

[85] H. Narita and H. Ohshima. Improvement of single-phase subchannel analysis code asfre-iii – verification analysis of fuel pin heat transfer model and pressure loss model. *PNC TN9410*, pages 97–104, 1994.

[86] J. Jeong, M. Song, and K. Lee. Cfd investigation of three-dimensional flow phenomena in a jaea 127-pin wire-wrapped fuel assembly. *Nuclear Engineering and Design*, 323:166–184, 2017.

[87] G. Kennedy, K.V. Tichelen, and H. Doolaard. Experimental investigation of the pressure loss characteristics of the full-scale myrrha fuel bundle in the complot lbe facility. 2015.

[88] A. Saxena. *Thermal-hydraulic numerical simulation of fuel sub-assembly for Sodium-cooled Fast Reactor*. PhD thesis, 2014.

[89] A. Shams. Towards the accurate numerical prediction of thermal hydraulic phenomena in corium pools. *Annals of Nuclear Energy*, 117:234–246, 2018.

[90] C. Pe'ñ'a Monferrer, J.L. Mu'ñ'oz Cobo, and S. Chiva. Cfd turbulence study of pwr spacer-grids in a rod bundle. *Science and Technology of Nuclear Installations*, 2014.

[91] A. Batta and A.G. Class. Cfd analysis of pressure drop across grid spacers in rod bundles compared to correlations and heavy liquid metal experimental data. *Nuclear Engineering and Design*, 312:121–127, 2017.

[92] A. Mathur, H. Uitslag-Doolaard, and F. Roelofs. Reduced-resolution rans approach to grid spacer fuel assemblies. *Nuclear Engineering and Design*, 356:110374, 2020.

[93] S. Neti, R. Eichhorn, and O.J. Hahn. Laser doppler measurements of flow in a rod bundle. *Nuclear Engineering and Design*, 74:105–116, 1982.

[94] K. Rehme. The structure of turbulent flow through rod bundles. *Nuclear Engineering and Design*, 74:105–154, 1987.

[95] R.F. Neumeister, S.V. Möller, and G. Ribatski. Thermal-hydraulic characteristics of rod bundles with spacer grids: an overview. *Nuclear Engineering and Design*, 446:114516, 2026.

[96] G. Grötzbach. Anisotropy and buoyancy in nuclear turbulent heat transfer – critical assessment and needs for modeling. *Forschungszentrum Karlsruhe, FZKA 7363*, 2007.

[97] S. Kenjeres and K. Hanjalic. Convective rolls and heat transfer in finite-length rayleigh–bénard convection: a two-dimensional numerical study. pages 7987–7998, 2000.

[98] C. Donaldson. Construction of a dynamic model of the production of atmospheric turbulence and the dispersal of atmospheric pollutants. *Haugen, D.A. (Ed.), Workshop on Micrometeorology. Amer. Met. Society*, pages 313–392, 1973.

[99] W. Rodi. Turbulence models and their application in hydraulics – a state of the art review. *3rd ed. IAHR Publication*, 1993.

[100] L. Carteciano and G. Grötzbach. Validation of turbulence models for a free hot sodium jet with different buoyancy flow regimes using the computer code flutan. *Forschungszentrum Karlsruhe, FZKA 6600*, 2003.

[101] L. Chandra and G. Grötzbach. Analysis and modelling of the turbulent diffusion of turbulent heat fluxes in natural convection. *International Journal of Heat and Fluid Flow*, 29:743–751, 2008.

[102] A. Shams, A.D. Santis, L. Koloszar, A.V. Ortiz, and C. Narayanan. Status and perspectives of turbulent heat transfer modelling in low-prandtl number fluids. *Nuclear Engineering and Design*, 353, 2019.

[103] I. Otic, G. Groetzbach, and M. Woerner. Analysis and modelling of the temperature variance equation in turbulent natural convection for low-prandtl number fluids. *Journal of Fluid Mechanics*, 525:237–261, 2005.

[104] W. Guo, A. Shams, and B. Niceno. Direct numerical simulation of a mixed convection flow in liquid metal with varying buoyancy. *SESAME International Workshop, The Netherlands*, page 19–21, 2019.

[105] M. Duponcheel and Y. Bartosiewicz. Dns and les of liquid metal impinging jets. *SESAME Project – Deliverable 1, 3*, 2018.

[106] S. Kenjeres, S.B. Gunarjo, and K. Hanjalić. Contribution to elliptic relaxation modelling of turbulent natural and mixed convection. *International Journal of Heat and Fluid Flow*, 26(4):569–586, 2005.

[107] J. Lai, G. Busco, E. Merzari, and Y. Hassan. Direct numerical simulation of the flow in a bare rod bundle at different prandtl numbers. *Journal of Heat Transfer*, 141, 2019.

[108] X. Zhou, D. Zhang, J. Liu, C. Lin, Y. Liang, W. Tian, S. Qiu, and G. Su. Numerical and experimental analysis of lbe flow and heat transfer characteristics in hexagonal rod bundles. *Annals of Nuclear Energy*, 189, 2023.

[109] J. Liu, P. Song, D. Zhang, S. Wang, C. Lin, Y. Liu, L. Zhou, C. Wang, W. Tian, and S. Qiu. Thermal-hydraulic research on rod bundle in the lbe fast reactor with grid spacer. *Nuclear Engineering and Technology*, 54:2728–2735, 2022a.

[110] J. Pacio, M. Daubner, F. Fellmoser, K. Litfin, and T. Wetzel. Heavy-liquid metal heat transfer experiment in a 19-rod bundle with grid spacers. *Nuclear Engineering and Design*, 273:33–46, 2014.

[111] D. Martelli, R. Marinari, G. Barone, I. Piazza, and M. Tarantino. Cfd thermo-hydraulic analysis of the circe fuel bundle. *Annals of Nuclear Energy*, 103:294–305, 2017.

[112] D. Angeli, A. Fregni, and E. Stalio. Direct numerical simulation of turbulent forced and mixed convection of lbe in a bundle of heated rods with p/d = 1.4. *Nuclear Engineering and Design*, 355:110320, 2019.

[113] C. Peskin. The immersed boundary method. *Acta Numerica*, 11:479–517, 2002.

[114] R.J. LeVeque and Z. Li. Immersed interface method for elliptic equations with discontinuous coefficients and singular sources. *SIAM Journal on Numerical Analysis*, 31(4):1019–1044, 1994.

[115] S.V. Patankar. A numerical method for conduction in composite materials, flow in irregular geometries and conjugate heat transfer. In *Proceedings of the 6th International Heat Transfer Conference*, volume 3, page 297, 1978.

[116] R. LeVeque. High resolution finite volume methods on arbitrary grids via wave propagation. *Journal of Computational Physics*, 78(1):36–63, 1988.

[117] R. Mittal and G. Iaccarino. Immersed boundary methods. *Annual Review of Fluid Mechanics*, 37:239–261, 2005.

[118] G.S. Barozzi, C. Bussi, and M.A. Corticelli. A fast cartesian scheme for unsteady heat diffusion on irregular domains. *Numerical Heat Transfer, Part B*, 46:56–77, 2004.

[119] M. Piller, S. Polidoro, and E. Stalio. Multiplicity of solutions for laminar, fully-developed natural convection in inclined, parallel-plate channels. *International Journal of Heat and Mass Transfer*, 79:1014–1026, 2014.

[120] E. Stalio and M. Piller. Direct numerical simulation of heat transfer in converging–diverging wavy channels. *Journal of Heat Transfer*, 129(7):769–777, 2007.

[121] M. Piller and E. Stalio. Numerical investigation of natural convection in inclined parallel-plate channels partly filled with metal foams. *International Journal of Heat and Mass Transfer*, 55(23-24):6506–6513, 2012.

[122] S.V. Patankar. *Numerical Heat Transfer and Fluid Flow*. McGraw-Hill, 1 edition, 1980.

[123] A.J. Chorin. Numerical solution of the navier–stokes equations. *Mathematics of Computation*, 22:754–762, 1968.

[124] P.M. Gresho and R. Sani. On pressure boundary conditions for the navier–stokes equations. *International Journal for Numerical Methods in Fluids*, 7:1111–1145, 1987.

[125] M. Piller and E. Stalio. Numerical investigation of natural convection in inclined parallel-plate channels partly filled with metal foams. *International Journal of Heat and Mass Transfer*, 55(23–24):6506–6513, 2012.

[126] S. Pirozzoli. Prandtl number effects on passive scalars in turbulent pipe flow. *Journal of Fluid Mechanics*, 965, 2023.

[127] G.K. Batchelor. Diffusion in a field of homogeneous turbulence. i. eulerian analysis. *Australian Journal of Scientific Research, Series A: Physical Sciences*, 2:437–450, 1949.

[128] M.M. Rogers, N.N. Mansour, and W.C. Reynolds. An algebraic model for the turbulent flux of a passive scalar. *Journal of Fluid Mechanics*, 203:77–101, 1989.

[129] B.A. Younis, C.G. Speziale, and T.T. Clark. A rational model for the turbulent scalar fluxes. *Proceedings of the Royal Society A: Mathematical, Physical and Engineering Sciences*, 461:575–594, 2005.

[130] B.J. Daly and F.H. Harlow. Transport equations in turbulence. *Physics of Fluids*, 13:2634–2649, 1970.

[131] G. Grasso, C. Petrovich, D. Mattioli, C. Artioli, P. Sciora, D. Gugiu, G. Bandini, E. Bubelis, and K. Mikityuk. The core design of alfred, a demonstrator for the

european lead-cooled reactors. *Nuclear Engineering and Design*, 278:287–301, 2014.

[132] J. Pacio, S.K. Chen, Y.M. Chen, and N.E. Todreas. Analysis of pressure losses and flow distribution in wire-wrapped hexagonal rod bundles for licensing. part i: The pacio-chen-todreas detailed model (pctd). *Nuclear Engineering and Design*, 388:111607, 2022.

[133] J. Pacio, S.K. Chen, Y.M. Chen, and N.E. Todreas. Analysis of pressure losses and flow distribution in wire-wrapped hexagonal rod bundles for licensing. part ii: The pacio-chen-todreas detailed model (pctd). *Nuclear Engineering and Design*, 388:111606, 2022.

[134] X. Zhu, S. Morooka, and Y. Oka. Numerical investigation of grid spacer effect on heat transfer of supercritical water flows in a tight rod bundle. *International Journal of Thermal Sciences*, 76:—, 2014.

[135] M.A. Hassan and K. Rehme. Heat transfer near spacer grids in gas-cooled rod bundles. *Nuclear Technology*, 52, 1981.

[136] K. Mikityuk. Heat transfer to liquid metal: Review of data and correlations for tube bundles. *Nuclear Engineering and Design*, 239, 2009.

[137] V.I. Subbotin, P.A. Ushakov, P.L. Kirillov, M.H. Ibragimov, M.N. Ivanovski, E.M. Nomofilov, D.M. Ovechkin, L.N. Sorokin, and V.P. Sorokin. Heat transfer in elements of reactors with a liquid metal coolant. In *Proceedings of the 3rd International Conference on Peaceful Use of Nuclear Energy*, 1965.

[138] V. Borishanski, M. Gotovski, and E. Firsova. Heat transfer to liquid metals in longitudinally wetted bundles of rods. *Atomnaya Energiya*, 27(6), 1969.

[139] V.H. Gräber and M. Rieger. Experimentelle untersuchung des wärmeübergangs an flüssigmetalle (nak) in parallel durchströmten rohrbündeln bei konstanter und exponentieller wärmeflussdichteverteilung. —, 19, 1972.

[140] S.B. Pope. *Turbulent Flows*. Cambridge University Press, Cambridge, UK, 2000.

[141] E. Buckingham. On physically similar systems: Illustrations of the use of dimensional equations. *Physical Review*, 4(4):345–376, 1914.

[142] Data-driven scale-adaptive turbulence closure modelling. Presented at the 1st European Fluid Dynamics Conference (EFDC1), Aachen, Germany, 2024.